Transverse Momentum of Gluons in *ep*-Scattering

Axel Cholewa

Deutsches Elektronensynchrotron Hamburg

29. September 2005

Transverse Momentum of Gluons in *ep*-Scattering at HERA

Diplomarbeit

von

Axel Cholewa

29. September 2005

angefertigt am

Deutschen Elektronensynchrotron Hamburg

unter Begutachtung von

Prof. Dr. Olaf Lechtenfeld

Institut für Theoretische Physik

Universität Hannover

Abstract

A Monte Carlo analysis of the phase space of hard interacting gluons in ep-scattering is presented. The event generator CASCADE is used in combination with the program HzTool to identify the accessible regions of phase space of present HERA measurements. A map of the k_t-x_g-plane is presented to show that in the region $-3 \lesssim \log x_g \lesssim -1$ transverse gluon momenta of up to $k_t \gtrsim 20$ GeV are accessible to HERA measurements. Furthermore the observables x_γ and the transverse jet energy E_T are found to be highly sensitive to the transverse momentum and the longitudinal momentum fraction of gluons.

Contents

,,Auch für den Physiker ist die Möglickeit einer
Beschreibung in der gewöhnlichen Sprache ein
Kriterium für den Grad des Verständnisses, das
in dem betreffenden Gebiet erreicht worden ist."

Werner Heisenberg

Introduction

The standard model of particle physics describes three of the four basic interactions of nature, excluding gravity. Its basic theoretical formalism consists of quantum field theories (QFT). Interactions manifesting for example in electrical and magnetic phenomena are described by quantum electrodynamics (QED). Radioactive decay and certain phenomena related thereto are described by the theory of weak interactions. In the standard model QED and the theory of weak interactions are successfully unified in the *electroweak* theory. Finally, the structure of protons and neutrons as well as the binding of these in atomic nuclei is due to the so-called strong interaction, which is described in quantum chromodynamics (QCD).

In QFTs particles are interpreted as excitations of quantum fields. All particles that form matter are fermions, i.e. particles of spin $\hbar/2$. All interactions are described by an exchange of so called gauge bosons, which are interpreted as excitations of the gauge fields describing the associated interaction. These gauge or exchange bosons have a spin of an integer multiple of $\hbar$. The exchange bosons of the electromagnetic, weak and strong interactions are the photon, the $W^{\pm}$- and Z^0-boson, and the gluon, respectively.

There are twelve fermions in the standard model, six leptons and six quarks, and twelve antifermions, each of which is the charge conjugate of a particle. Of these particles only leptons are found as free particles in nature. Up to now quarks have only been observed in bound states of two (e.g. the π-meson) or three (e. g. protons, neutrons) quarks or antiquarks.

The concept of antiparticles is a natural part of quantum field theories arising from creation and annihilation mechanisms. It allows a particle-

antiparticle pair to be created by gauge boson splitting and to annihilate by forming a gauge boson in the interaction.

To study the structure of the proton beams of electrons and protons are collided head-on in the storage ring HERA, located at the DESY laboratory in Hamburg. The interaction of electron and proton is dominated by photon exchange where a photon is emitted by an electron and interacts with a constituent of the proton, called parton. Gluons also may interact with the photon via the creation of a quark and an antiquark, one of which then may absorb the photon. In these processes, called *boson gluon fusion*, the momentum distribution of the gluons in the proton is of particular importance.

The so-called k_t-factorisation approach, which uses so-called *unintegrated* gluon distributions depending explicitly on the transverse momentum k_t of the gluons, is a central part of this thesis. It is analysed in which regions of the gluon phase space present HERA measurements can constrain these gluon densities in order to obtain a better understanding of the parton distributions in the proton.

The first chapter presents the HERA collider ring and the particle detector of the H1 collaboration. Chapter 2 gives an overview of the theory needed for an understanding of electron-proton scattering. Perturbative methods for the calculation of the scattering cross section are presented, k_t-factorisation is introduced, and further theoretical aspects concerning hadronic final states are shortly summarised.

Since this study was based entirely on Monte Carlo simulations of high energy physics events (event generators), chapter 3 outlines the basic methods and features used therein. In chapter 4 the program HzTool is presented which enables easy comparison of Monte Carlo simulations with measured data. By using this program along with the Monte Carlo simulation Cascade a total of 16 HERA measurements have been analysed to find out in which regions of the gluon phase space they can be used to make assertions about unintegrated gluon densities.

Chapter 5 finally discusses the results of this analysis and gives a short outlook to a possible future measurement based on this thesis.

Chapter 1

HERA and the H1 Detector

The electron-proton collider ring HERA (HADRON ELEKTRON RING ANLAGE) at DESY in Hamburg accelerates electrons up to an energy of 27.5 GeV and protons up to an energy of 920 GeV[1]. There are four interaction points in the northern, eastern, southern, and western halls, where the experiments H1, HERMES, ZEUS and HERA-B, respectively, are positioned (fig. 1.1).

HERMES investigates the spin structure of the nucleon by colliding polarised electrons from HERA with polarised gas targets, and HERA-B investigates CP-violation effects in B-meson decays by colliding protons from the HERA storage ring with stationary nuclei. These experiments are not considered in this thesis and will not be described any further.

The topic of this thesis is the investigation of the gluon structure of the proton with the experiments ZEUS and especially H1. Therefor the H1 detector is described in more detail in this chapter.[2]

Since 1994 positrons have been used instead of electrons, since the beam lifetime was increased significantly in this way. In 1998 and the first part of 1999 electrons had been in use again. When not stated otherwise the term electron refers to both electrons and positrons in the following.

---

[1]Before 1998 the proton energy was 820 GeV.

[2]A description of the ZEUS detector can be found at *http://www-zeus.desy.de/bluebook/bluebook.html.*
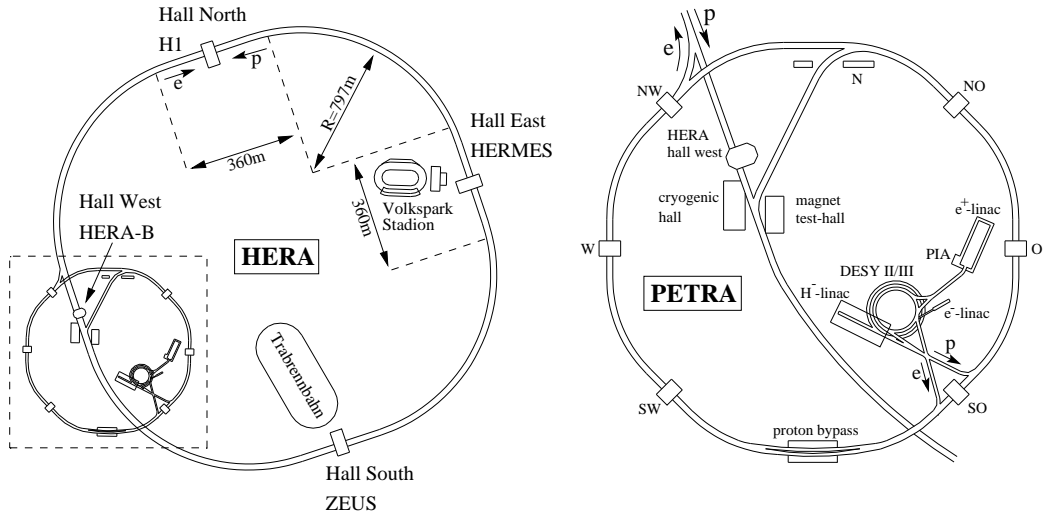
Figure 1.1: *The collider ring HERA is seen on the left with the four experiments. The pre-accelerators PETRA, DESY II and III and the linear pre-accelerators are depicted on the right.*

1.1   The Electron-Proton Accelerator HERA

The electrons and protons are pre-accelerated in linear colliders and the small storage rings DESY II and III, respectively, and PETRA II (fig. 1.1). They are injected into the HERA ring at an energy of 12 GeV for the electrons and 40 GeV for the protons. Electric fields then accelerate the particles up to their final energy in HERA. Superconducting magnets of 4.68 T are used to keep the protons on their orbit, while the electrons are kept on their path by normal conducting magnets with a field strength of 0.164 T.

The beams consist of bunches of $0.4 \cdot 10^{11}$ electrons and $0.7 \cdot 10^{12}$ protons each. A maximum of 210 bunches can be stored in HERA with a spacing of 28.8 m. This leads to a bunch crossing frequency of $\sim$10 MHz at the interaction points of ZEUS and H1.
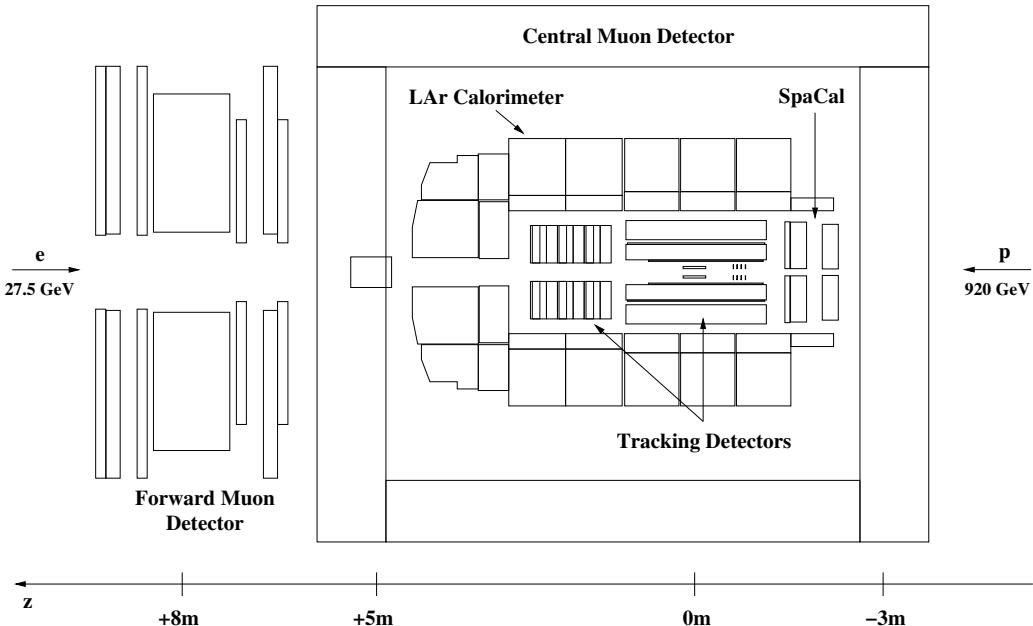
Figure 1.2: *Side view of the H1 Detector. The main components of the detector are indicated and a scale of the detector's size is given.*

1.2 The H1 Experiment at HERA

The main components of the H1 detector can be seen in figure 1.2. Also indicated is the positive z-direction, often referred to as the 'forward' region, which coincides with the direction of the proton beam.

The tracking system surrounding the interaction point measures the tracks of charged particles for momentum determination. The energy of the particles is measured in the liquid Argon calorimeter (LAr) surrounding the tracking system. The SpaCal (spaghetti calorimeter) determines the energy of electrons in the backward region. A superconducting coil surrounding the calorimeters produces a magnetic field of 1.15 T parallel to the beam axis. For the identification of muon tracks the central muon detectors (CMD) are located in an iron yoke which also returns the magnetic field. The forward muon detector is located in a toroidal magnet system at the front end of the detector. Tracking system and calorimetry are now explained in more detail.
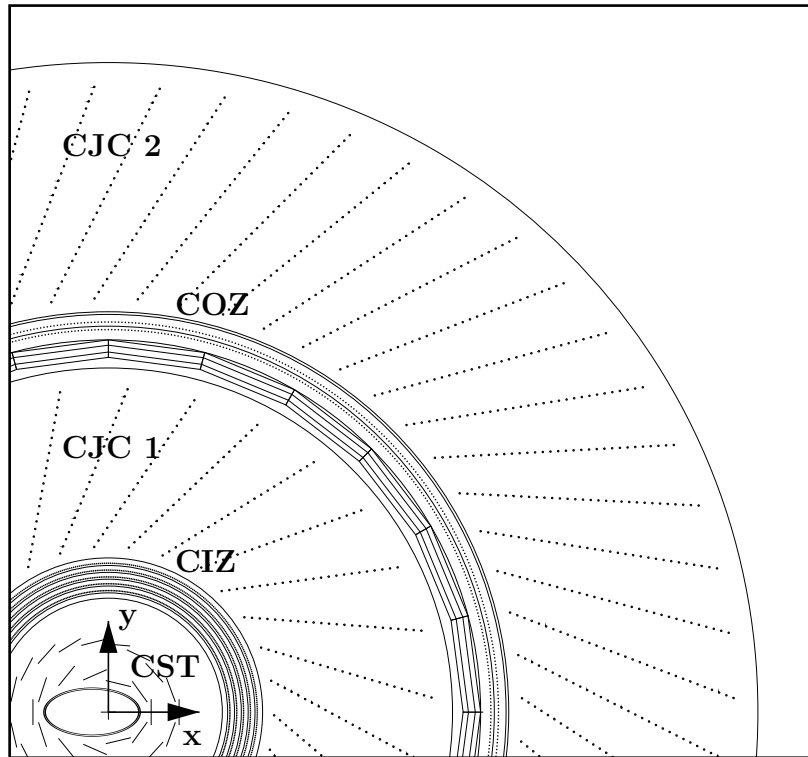
Figure 1.3: *Cross section of the tracking system in the x-y plane. The axes originate from the interaction point. The central jet chamber CJC 1 and 2 are indicated as well as the central inner (CIZ) and outer (COZ) z-chambers and the central silicon tracker (CST).*

1.2.1   Tracking

The inner part of the detector contains the tracking system, which consists of the two central jet chambers (CJC 1 and 2), the central inner (CIZ) and central outer (COZ) z-chambers and the central silicon tracker (CST). The layout is shown in figure 1.3.

The Central Silicon Detector

The innermost part of the detector, the CST, consists of two concentric layers of silicon sensors that measure tracks of charged particles close to the interaction vertex with high accuracy. This provides a possibility to measure

the decay lengths of charmed or beauty hadrons, which are in the order of a few hundred micrometers.

The Central z-Chambers

The CIZ, a drift chamber located between CST and CJC 1, and the COZ, located between the two jet chambers, measure the z-coordinate of a track with a typical z-resolution of 300 μm. Here the sense wires are strung perpendicular to the beam axis, so that the drift direction is parallel to that axis.

The Jet Chambers

The jet chambers are drift chambers with sense wires parallel to the beam axis. The drift cells are inclined against the radius so that electrons from ionisations drift approximately perpendicular to high momentum tracks in the magnetic field. The spacial resolution of the jet chambers is 170 μm in the r-ϕ plane.

1.2.2 The Liquid Argon Calorimeter

The calorimetry system is divided into an electromagnetic and a hadronic calorimeter (fig. 1.4). The calorimeters are build up of alternating layers of showering and read out cells. For both electromagnetic and hadronic calorimetry liquid Argon is used as active material in th cells.

Electromagnetic Calorimetry

The electromagnetic calorimeter uses lead as showering material and is located around the tracking system. Electrons as well as photons interact with the showering material electromagnetically, either radiating a photon in the process or, if the particle is a photon, splitting into an e^+e^- pair. Electrons, for example, mostly lose their energy by emitting bremsstrahlung, which than splits further into an e^+e^- pair, which then may radiate bremsstrahlung as
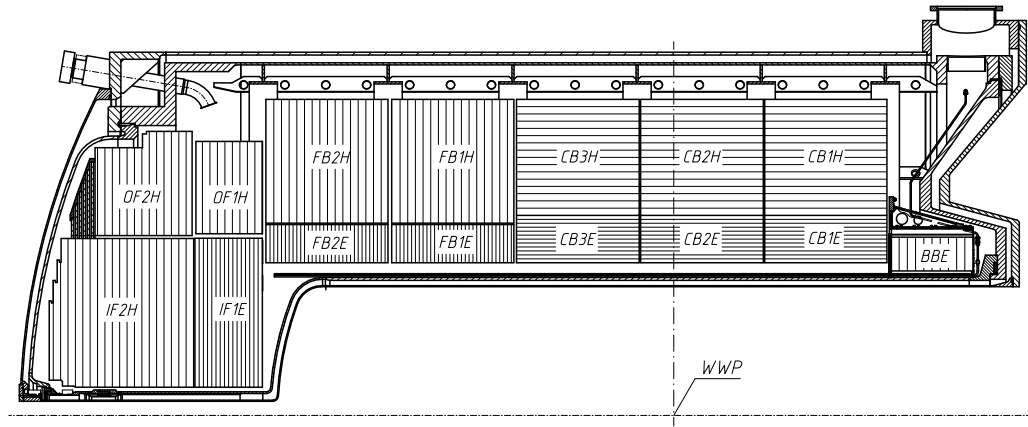
Figure 1.4: *Longitudinal cross section of the liquid Argon calorimeter showing the sections of the inner electromagnetic and the outer hadronic part.* WWP *indicates the interaction point.*

well. This showering continues until the shower particles are absorbed in the read out material.

Hadronic Calorimetry

Hadrons passing the electromagnetic calorimeter deposit their energy in hadronic showers in the outer part of the LAr calorimeter. Hadronic showers originate from strong interactions of hadrons passing the calorimeter with the nuclei of the showering material, here stainless steel. The showers created in such interactions are broader than electromagnetic showers, but the hadrons also interact by nucleon excitation or fission. That is why the energy deposited in the detector by the hadrons is always below the actual hadron energy.

1.2.3   Muon Detection

Since muons do not lose much of their energy in the calorimeters they easily reach the iron yoke surrounding the detector. For this reason, and for 'tail catching' of hadronic showers, the iron yoke is instrumented with drift chambers sandwiched between the iron layers of the yoke. There muons are

detected. The tracks can then be associated with tracks in the inner detector parts which also determine the muon momentum.

The forward muon detector located at the forward end of the detector is build around a toroidal magnet and works in a similar way to the central muon detector.

Chapter 2

Theoretical Overview

This chapter serves as an overview of the theory of electron-proton (ep) and positron-proton scattering. In the following the term ep-scattering always includes positron-proton scattering, since all the theoretical aspects presented below apply to both.

The first section gives a short introduction into the kinematics relevant for collisions at HERA. Special features of lepton-hadron scattering are presented and its importance for the understanding of the structure of hadrons in general and the proton in particular is emphasised.

After that mechanisms are presented to describe the contribution of partons[1] to the hadron momentum. These mechanisms include parton evolution equations, which provide calculational methods for perturbative processes.

At the end of the chapter methods for describing the transition from quarks to hadrons, called hadronisation, are introduced. Special features of the photoproduction regime at low photon virtualities, heavy quark and jet production are discussed.

2.1   Lepton-Hadron Scattering

In lepton-hadron scattering leptons are used to probe the structure of hadrons by an exchange of either charged weak gauge bosons, i.e. $W^{\pm}$ (*charged cur-*

---

[1]The term parton always refers to quarks *and* gluons.

rent), or neutral gauge bosons, i.e. Z^0 or γ (*neutral current*). Only neutral current interactions are considered in this thesis, and because of the small cross section of weak interactions photon exchange dominates most processes. Therefore, when not stated otherwise, the term photon refers to both Z^0 and γ^*.

The following Lorentz invariants can be defined via the four momenta of the incoming and outgoing particles:

$$
\begin{align}
s &= (p + P)^2 \tag{2.1} \\
Q^2 &= -q^2 = -(p - p')^2 \tag{2.2} \\
W_{\gamma p} &= (q + P)^2 \tag{2.3} \\
x_{\mathrm{Bj}} &= \frac{Q^2}{2P \cdot q} \tag{2.4} \\
y_{\mathrm{Bj}} &= \frac{P \cdot q}{P \cdot p}. \tag{2.5}
\end{align}
$$

As illustrated in figure 2.1, p, p', P, and q denote the four momenta of the incoming electron, the outgoing electron, the proton and the exchanged boson, respectively. The squared energy of the electron-proton centre-of-mass system (cms) is given by s, Q^2 defines the negative squared four momentum transfer, and $W_{\gamma p}$ is the squared cms energy of the photon-proton system. $W_{\gamma p}$ is also often referred to as the hadronic cms energy, because hadrons are produced in the interaction of the virtual photon and the proton. x_{Bj} and y_{Bj} are the Björken variables which denote the longitudinal momentum fraction with respect to the hadron and the inelasticity, respectively. In the proton rest frame the latter can be interpreted as the fraction of the electron energy carried by the virtual photon, $y_{\mathrm{Bj}} = E_{\gamma^*}^{rest}/E_e^{rest}$.

The kinematics of *ep*-scattering are fully described by only three of these five variables, because they are not independent and can be related by

$$
\begin{align}
Q^2 &= s \cdot x \cdot y \tag{2.6} \\
W_{\gamma p} &= y \cdot s - Q^2. \tag{2.7}
\end{align}
$$
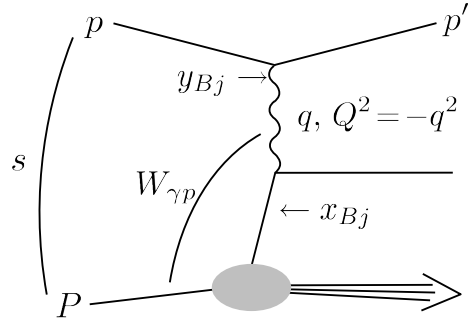
Figure 2.1: *Illustration of Lorentz invariants and four momenta relevant in ep-scattering*

2.1.1 The Parton Model

The following considerations are based on textbook [1], which is a good introduction into the subject, and textbooks [2, 3], which both present the subject in more detail.

In the so-called naive parton model (PM) hadrons consist of non-interacting quarks, or more generally partons. The cross section for a charged lepton scattering electromagnetically off one of those quarks is

$$\frac{d^2\sigma^{lq}}{dxdQ^2} = \frac{2\pi\alpha^2}{xQ^4}\left[1 + (1-y)^2\right]e_i^2\,x\ , \tag{2.8}$$

which by summing over all quarks i in the proton becomes

$$\frac{d^2\sigma^{lp}}{dxdQ^2} = \frac{2\pi\alpha^2}{xQ^4}\left[1 + (1-y)^2\right]\sum_i e_i^2\,x\,f_i(x)\ . \tag{2.9}$$

Here, $f_i(x)$ is called parton distribution (or density) function (PDF) and denotes the probability density of finding a quark of flavour i and charge e_i and a fraction x of the proton momentum.

The general form for the differential cross section of electromagnetic lepton-proton (lp-) scattering is given by

$$\frac{d^2\sigma^{ep}}{dxdQ^2} = \frac{2\pi\alpha^2}{xQ^4}\left[\left(1 + (1-y)^2\right)F_2^{ep}(x,Q^2) - y^2 F_L^{ep}(x,Q^2)\right] \tag{2.10}$$

with F_2^{ep} being the proton structure function and F_L^{ep} its longitudinal component[2]. Compared to this equation (2.9) predicts

$$F_2^{em}(x, Q^2) = F_2^{em}(x) = \sum_i e_i^2 \, x \, f_i(x) \qquad \text{and} \qquad F_L^{lh} = 0 \ . \qquad (2.11)$$

Equation (2.11) states that the naive parton model leads to a structure function independent of Q^2. That the longitudinal contribution of the virtual photon to the cross section vanishes here is a consequence of scattering from spin-$\frac{1}{2}$ particles which cannot absorb longitudinally polarised vector bosons.

The independence from the scale Q^2 is called Björken-scaling. Measurements at HERA confirmed earlier experiments at other accelerators that proved deviations from this scaling behaviour. These scaling violations seen in HERA and other data were only seen because higher energies made available a wider range in $x = Q^2/sy$ (eq. (2.6)). They cannot be explained by the naive parton model but need an improvement which takes into account not only the static quark content of the proton, but also contributions of gluon radiation where quarks interacting with the photon radiate gluons before the interaction. To show how this non scaling behaviour is predicted by perturbative quantum chromodynamics (pQCD) is the aim of the next section.

2.2 The Improved Parton Model and the Collinear Approach

In order to describe the scaling violations observed in many experiments one has to take into account perturbative corrections to the process shown in figure 2.2a. First order corrections include gluon radiation in the initial and in the final state (fig. 2.2b and 2.2c respectively). To illustrate how these are treated perturbatively the structure function F_2 of (2.11) is first related to the scattering amplitude for the photon-quark scattering before the corrections

---

[2]In contrast to real photons, which only occur in transverse polarisation due to their vanishing mass, virtual photons with an invariant mass $\neq 0$ can aquire a longitudinal polarisation.
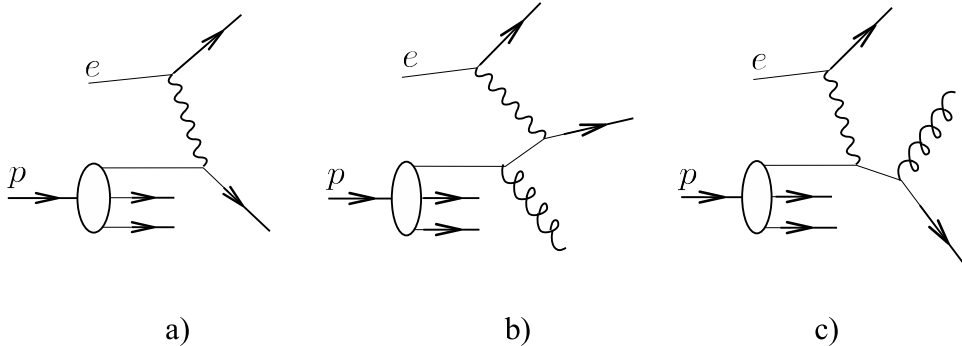
Figure 2.2: *Scattering of an electron off a parton in a) the naive parton model and the parton model improved by b) initial state gluon radiation and c) final state gluon radiation.*

are added. At the end of this section gluons are included in the evolution equations.

2.2.1 First Order Corrections to the Structure Function

The structure function F_2 of equation (2.11) describes the subprocess $\gamma^* q \to q$, and can be written as

$$\frac{F_2(x, Q^2)}{x} = \sum_i e_i^2 \int_x^1 \frac{dx'}{x'} f_i(x') \delta\left(1 - \frac{x}{x'}\right) = \frac{\sigma(\gamma^* q \to q)}{\sigma_0} . \qquad (2.12)$$

where $\sigma_0 = 4\pi^2 \alpha / \hat{s}$ depends on the fine structure constant α and the cms-energy $\hat{s}$ of the $\gamma^* q$-system.

In the $\gamma^* q$-centre-of-mass frame the quark would leave the interaction collinear to the photon as illustrated in figure 2.3a. By radiating a gluon either before or after interacting with the virtual photon the quark can acquire a transverse momentum component relative to the virtual photon momentum (fig. 2.3b), so that the resulting cross section would depend on this transverse momentum.

The real first order corrections shown in figure 2.4b and c picture the process $\gamma^* q \to q \, g$. Evaluating the matrix elements of these processes gives
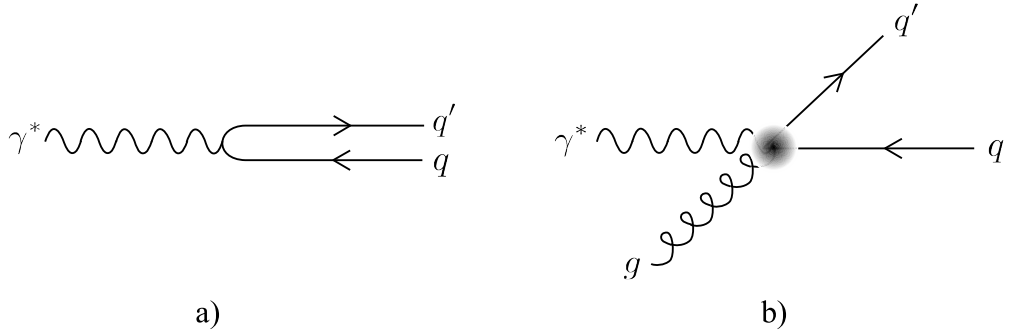
**Figure 2.3:** *Photon-quark collision in the γ^*q-cms. The scattered quark is a) collinear with the virtual photon if gluon radiation is neglected and b) acquires transverse momentum relative to the γ^* if gluon radiation is taken into account.*

a differential cross section as a function of the transverse momentum of the outgoing quark, p_t:

$$\frac{1}{\sigma_0}\frac{d\sigma}{dp_t^2}(\gamma^*q \to q\,g) \simeq e_i^2 \frac{1}{p_t^2}\frac{\alpha_s}{2\pi}P_{qq}(z) \ , \tag{2.13}$$

with α_s representing the strong coupling constant. $P_{qq}(z)$ is called 'splitting function' and describes the probability of a quark radiating a gluon and thereby becoming a quark with a fraction z of its original momentum.[3] It is given by

$$P_{qq}(z) = \frac{4}{3}\left(\frac{1+z^2}{1-z}\right) \ . \tag{2.14}$$

It is important to note the infrared divergencies arising from the $1/p_t^2$ term in (2.13) and from the $(1-z)$ term in (2.14). The latter gets cancelled out by virtual corrections pictured in figure 2.4a. The treatment of the divergence at $p_t^2 \to 0$, which represents the long range or soft part of the strong interaction[4], is outlined below.

The cross section for $\gamma^*q \to q\,g$ would then be (to first order in α_s):

$$\frac{\sigma(\gamma^*q \to q\,g)}{\sigma_0} \ \simeq \ e_i^2 \int_{\kappa^2}^{p_{t,max}^2} dp_t^2 \frac{d\sigma}{dp_t^2}(\gamma^*q \to q\,g) \tag{2.15}$$

---

[3]A splitting function $P_{fi}(z)$ describes the probability of a final state parton f originating from an initial state parton i and carrying a fraction z of of the initial state's momentum.

[4]see for example [2], p. 104
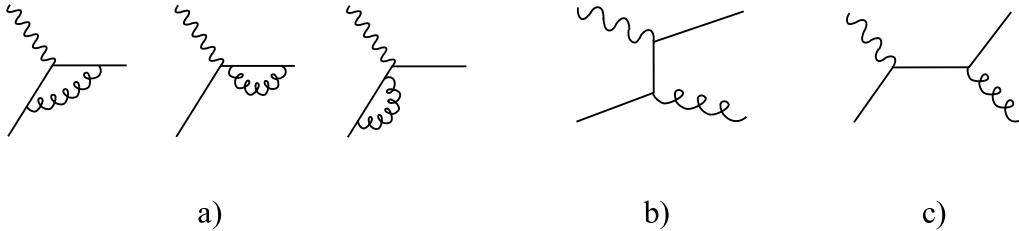
Figure 2.4: *Diagrams for virtual (a) and real (b, c) first order corrections*

$$\simeq \; e_i^2 \int_{\kappa^2}^{p_{t,max}^2} \frac{dp_t^2}{p_t^2} \frac{\alpha_s}{2\pi} P_{qq}(z) \; . \tag{2.16}$$

The transverse momentum of the outgoing quark is kinematically limited because of four momentum conservation by $p_{t,max}^2 = \hat{s}/4 = Q^2(1-z)/4z$ in the γ^*q-centre-of-mass frame. Furthermore the lower cut-off scale κ^2 ensures that the cross section is finite. The cross section may now be written as

$$\begin{aligned}
\frac{\sigma(\gamma^*q \to q\,g)}{\sigma_0} &\simeq \; e_i^2 \frac{\alpha_s}{2\pi} P_{qq}(z) \left[\ln\left(\frac{Q^2}{\kappa^2}\right) + \ln\frac{1-z}{4z}\right] \\
&\simeq \; e_i^2 \frac{\alpha_s}{2\pi} \left[P_{qq}(z)\ln\left(\frac{Q^2}{\kappa^2}\right) + C(z)\right] \;, \tag{2.17}
\end{aligned}$$

where the non-singular (in p_t) term is absorbed in the constant $C(z)$. This result can now be added to the structure function of (2.12) as a correction of first order in α_s (neglecting the non-singular term $C(z)$, which does not give a leading contribution):

$$\begin{aligned}
\frac{F_2(x,Q^2)}{x} &= \; \sum_i e_i^2 \int_x^1 \frac{dx'}{x'} f_i^0(x') \cdot \\
&\quad \cdot \left[\delta\left(1-\frac{x}{x'}\right) + \frac{\alpha_s}{2\pi} P_{qq}\left(\frac{x}{x'}\right)\ln\left(\frac{Q^2}{\kappa^2}\right)\right] \tag{2.18}
\end{aligned}$$
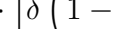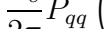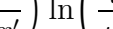
Here $z = x/x'$ is the fraction of the initial quark momentum of the quark after gluon emission, while x' and x represent the proton momentum fractions of the quark before and after gluon emission, respectively. The integral over x' sums the contributions from all possible initial momentum fractions. The

delta function now represents a parton carrying the same fraction as the initial parton, so that it corresponds to $\gamma^* q \to q$ without gluon radiation. In analogy to renormalisation the initial parton density $f_i^0(x)$ can be see as an unmeasurable parton distribution, similar to the 'bare' charge e that appears in the coupling constant.

2.2.2   Long and Short Range Contributions and Parton Evolution

The resulting structure function (2.18) now contains contributions of the long range part $p_t \to 0$ of the strong interaction represented by the cut-off scale κ, and the short range part taking place at a scale Q^2 induced by the interaction with the virtual photon. Since the long range part cannot be calculated by perturbative methods it is desirable to factorise the cross section into a short range and a long range part. This is done with a formalism similar to renormalisation: by introducing a so-called *collinear factorisation scale* μ the dependence on $\ln Q^2$ and $\ln \kappa^2$ can be separated by $\ln(Q^2/\kappa) = \ln(Q^2/\mu) + \ln(\mu/\kappa)$, so that the parton densities depend on the cut-off scale representing the long range part,

$$f_i(x', \mu^2) = f_i^0(x') + \frac{\alpha_s}{2\pi} \int_{x'}^1 \frac{dx''}{x''} f_i^0(x'') P_{qq}\left(\frac{x'}{x''}\right) \ln\left(\frac{\mu^2}{\kappa^2}\right), \qquad (2.19)$$

so that the structure function becomes:

$$\begin{aligned}
\frac{F_2(x, Q^2)}{x} &= \sum_i e_i^2 \int_x^1 \frac{dx'}{x'} f_i(x', \mu^2) \left[\delta\left(1 - \frac{x}{x'}\right) + \right. \\
&\qquad\qquad \left. \frac{\alpha_s}{2\pi} P_{qq}\left(\frac{x}{x'}\right) \ln\left(\frac{Q^2}{\mu^2}\right) \right] \qquad (2.20)
\end{aligned}$$

In this way the structure function and with it the cross section is factorised into a perturbatively calculable term and a parton density including terms that cannot calculated by perturbative methods. However, it can be examined perturbatively how the parton densities *evolve* with a change in the scale μ by taking the derivative of (2.19):

$$\frac{\partial f_i(x, \mu^2)}{\partial \ln \mu^2} = \frac{\alpha_s}{2\pi} \int_x^1 \frac{dx'}{x'} f_i(x', \mu^2) P_{qq}\left(\frac{x}{x'}\right) \qquad (2.21)$$
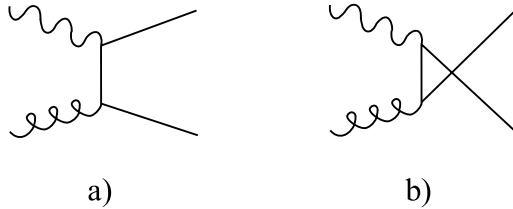
Figure 2.5: *Diagram of boson-gluon-fusion*

This type of *parton evolution equation* is mostly referred to as a DGLAP-
(Dokshitzer, Gribov, Lipatov, Altarelli, Parisi) or Altarelli-Parisi-
equation. By now it only accounts for the quark content of the proton while
the gluon content is left out.

Note that the parton densities $f_i(x, Q^2)$ are not physical observables like
the structure function F_2. They can be determined, of course, from the
observable structure function at any particular scale, because $F_2(x, Q^2) =
x \sum_i e_i^2 f_i(x, Q^2)$.

2.2.3 Including Gluons in Parton Evolutions

Since the virtual photon probes the quark content of the proton the process
$\gamma^* g \to q\bar{q}$ known as *boson gluon fusion* (BGF) also contributes to the struc-
ture function. It is this process that is studied in this thesis. The associated
diagrams diagrams are shown in figure 2.5. The quark that interacts with
the virtual photon now originates from a gluon inside the proton. In analogy
to the case of quarks these diagrams contribute to the structure function by
adding an extra term:

$$
\begin{aligned}
\frac{F_2(x, Q^2)}{x} &= \left.\frac{F_2(x, Q^2)}{x}\right|_{\gamma^* q \to qg} + \left.\frac{F_2(x, Q^2)}{x}\right|_{\gamma^* g \to q\bar{q}} \\
&= \left.\frac{F_2(x, Q^2)}{x}\right|_{\gamma^* q \to qg} + \\
&\quad + \sum_i e_i^2 \int_x^1 \frac{dx'}{x'} f_g(x') \frac{\alpha_s}{2\pi} P_{qg}\left(\frac{x}{x'}\right) \ln\left(\frac{Q^2}{\mu^2}\right) \quad (2.22)
\end{aligned}
$$

The splitting function $P_{qg}(z)$ for gluons splitting into a quark-antiquark
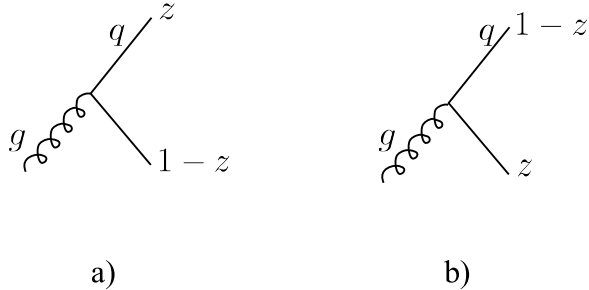
Figure 2.6: *Crossed diagrams of gluon splitting where the momentum fraction z and $1 - z$ are interchanged.*

pair is given by

$$P_{qg}(z) = \frac{1}{2}\left[z^2 + (1-z)^2\right].\tag{2.23}$$

The second term describes the crossed diagram (fig. 2.6b) of the first (fig. 2.6a) where the momentum fractions are interchanged and the quark interacting with the virtual photon carries the fraction $1 - z$ instead of z. This also effects the evolution of the quark densities, now given by

$$\frac{\partial f_i(x,\mu^2)}{\partial \ln \mu^2} = \frac{\alpha_s}{2\pi}\int_x^1 \frac{dx'}{x'}\left[f_i(x',\mu^2)P_{qq}\left(\frac{x}{x'}\right) + f_g(x',\mu^2)P_{gq}\left(\frac{x}{x'}\right)\right].\tag{2.24}$$

To express an evolution equation for the gluon density one has to take into account the processes and that correspond to the splitting functions P_{gq} and P_{gg}, respectively. This then gives the evolution equation for gluon densities:

$$\frac{\partial f_g(x,\mu^2)}{\partial \ln \mu^2} = \frac{\alpha_s}{2\pi}\int_x^1 \frac{dx'}{x'}\left[f_g(x',\mu^2)P_{gq}\left(\frac{x}{x'}\right) + f_g(x',\mu^2)P_{gg}\left(\frac{x}{x'}\right)\right],\tag{2.25}$$

with the splitting functions

$$P_{gq}(z) = \frac{4}{3}\left[\frac{1+(1-z)^2}{z}\right]\quad \text{and}\tag{2.26}$$

$$P_{gg}(z) = 6\left[\frac{1-z}{z} + \frac{z}{1-z} + z(1-z)\right].\tag{2.27}$$

With these evolution equations a tool exists for calculating the contribution of parton emission to the structure function. To do this the DGALP-formalism re-sums leading $\ln\mu^2$ contributions in successive gluon emissions
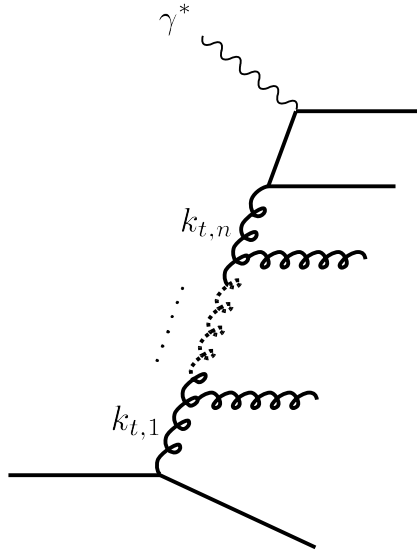
Figure 2.7: *Successive emission of gluons in BGF.*

(fig. 2.7). This approximation is equivalent to a region of phase space where the virtualities k_i of the propagating gluons are strongly ordered:

$$\mu^2 \ll k_1^2 \ll k_2^2 \ll \cdots \ll k_n^2 \ll Q^2. \tag{2.28}$$

It is this strong ordering that gives the *collinear* ansatz its name, because it states that the gluon entering the hard interaction with the virtual photon has a negligible transverse momentum compared to the scale of the hard interaction and can therefore be taken as collinear with the incoming proton.

2.2.4 DGLAP at small x

In the collinear factorisation scheme the transverse momentum of the partons entering the hard interaction is neglected. The evolution of parton densities is examined in dependence of leading logarithms of Q^2 (a common choice for μ^2).

At small momentum fractions, $x \ll x' \Rightarrow \frac{x}{x'} = z \ll 1$, the splitting functions can be approximated by[5]

$$P_{qq} \to \frac{4}{3}, \quad P_{qg} \to \frac{1}{2}, \quad P_{gq} \to \frac{8}{3z}, \quad P_{gg} \to \frac{6}{z}, \tag{2.29}$$

_____

[5]cf. eqs.(2.14), (2.23), (2.26) and (2.27)

which shows that here the gluon splitting functions give the biggest contribution and that P_{gg} dominates the gluon evolution. The DGLAP equation for the gluon density now reads

$$\frac{\partial f_g(x, Q^2)}{\partial \ln Q^2} = \int_x^1 \frac{dx'}{x'} f_g(x', \mu^2) P\left(\frac{x}{x'}\right) , \qquad (2.30)$$

where the factor $\alpha_s/2\pi$ has been absorbed into the splitting function $P(z) = (\alpha_s/2\pi) \cdot P_{gg}(z)$. $P(z)$ can now be expanded into a power series which at low x is dominated by powers of $\ln^1/_x$. In DGLAP these are neglected, so that at low x the DGALP equations obviously need some modification.

2.3 k_t-Factorization

In the DGLAP ansatz a process dependent coefficient function, $C^i(x/z)$, and a collinear parton density $f_i(z, \mu_f^2)$, are convoluted to form the cross section:

$$\sigma \sim \int \frac{dx'}{x'} C^i\left(\frac{x}{x'}\right) f_i(x', \mu_f^2), \qquad (2.31)$$

where the parton density does not depend on the transverse momentum of the partons.

To account for the larger phase space available at low x the k_t-factorisation scheme [4] factorises the cross section into a scattering cross section $\hat{\sigma}$ and a k_t-dependent, so-called *unintegrated* parton density (uPDF) $\mathcal{G}(z, k_t)$, where the parton's transverse momentum k_t now plays a role similar to the factorisation scale μ_f in the DGLAP approach. The cross section then becomes

$$\sigma \sim \int \frac{dx'}{x'} \int dk_t^2 \hat{\sigma}\left(\frac{x}{x'}, k_t\right) \mathcal{G}(x', k_t), \qquad (2.32)$$

where the transverse momentum is allowed to take on any kinematically allowed value. Here the matrix element of the hard scattering is taken *off-shell*, which means that the virtuality of the gluon entering the hard scattering is not neglected as it is the case in the collinear factorisation.

In the following two approaches for unintegrated parton densities are presented: the BFKL (BALITSKY, FADIN, KUAREV, LIPATOV) approach

valid at small x, and the CCFM-approach (CATANI, CIAFALONI, FIORANI, MARCHESINI), which is an attempt for an interpolation between DGLAP and BFKL valid both at small and large x.

Unintegrated gluon densities $\mathcal{G}(x, k_t)$ of the k_t-factorisation approach can be compared to the gluon densities $f_g(x, \mu_f)$ of the collinear approach by:

$$x f_g(x, \mu_f) \simeq \int^{\mu_f} \frac{dk_t^2}{k_t^2} \mathcal{G}(x, k_t) . \qquad (2.33)$$

This is, however, not an exact equation since the integration over the transverse momentum for the calculation of the cross section also includes the k_t-dependent matrix element.

In the following x always denotes a parton's momentum fraction with respect to the proton. z_i stands for the momentum fraction of a propagating parton after the ith splitting relative to the mother parton. Hence, $1 - z_i$ always denotes the momentum fraction of the parton *emitted* from the ith splitting.

Furthermore, it is convention to use $\mathcal{G}(x, k_t)$ for DGLAP-like uPDFs, $\mathcal{F}(x, k_t)$ for uPDFs in the BFKL approach, and $\mathcal{A}(x, k_t, \bar{q})$ for uPDFs in the CCFM approach.

2.3.1 BFKL

Due to the dominating contributions of gluon splitting at small x the BFKL-approach only includes gluon density evolution. In this ansatz the emitted gluon takes a large fraction $(1 - z)_{z \to 0}$ of the momentum of the incoming gluon, and the momentum fraction of the propagating gluon is small. Therefore the BFKL approach offers a calculational scheme for soft propagating gluons ($z \to 0$) for which perturbative techniques may not be applicable anymore.

If the momentum fraction $z_i = x_i/x_{i-1}$ after gluon emission is small, $z \ll 1$, the momentum fractions x of the propagating gluons in a gluon ladder become strongly ordered (fig. 2.8):

$$x_0 \gg x_1 \gg \cdots \gg x_n. \qquad (2.34)$$
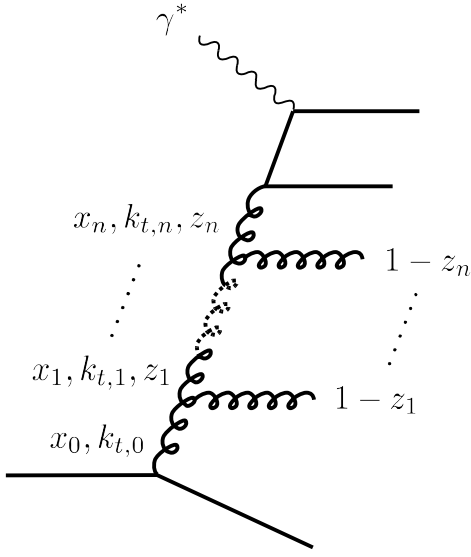
Figure 2.8: *Gluon ladder in BFKL. The momentum fractions $z_i = x_i/x_{i-1}$ of each emission are assumed to be small, $z \ll 1$, and the longitudinal momentum fractions relative to the proton momentum become ordered, $x_1 \gg \cdots \gg x_n$. The transverse momenta of the propagating gluons, $k_{t,i}$, are not ordered.*

The transverse momenta of the gluons, however, are left arbitrary and may perform a 'random walk'. The resulting large $\ln^1/_x$-terms are re-summed to all orders in BFKL, in contrast to the collinear approach where the splitting functions are truncated at a fixed perturbative order. The splitting functions here naturally become more complicated.

The BFKL evolution equation [5–7]

$$\frac{\partial \mathcal{F}(x, k_t)}{\partial \ln^1/_x} = \int dk_t'^2 \, K(k_t, k_t') \, \mathcal{F}(x, k_t) \tag{2.35}$$

includes the 'BFKL-kernel' $K(k_t, k_t')$, which can be found in [8] and [9], and the unintegrated gluon density $\mathcal{F}(x, k_t)$, which can be related to the DGLAP parton density by

$$x f_g(x, \mu_f) \simeq \int^{\mu_f} \frac{dk_t^2}{k_t^2} \mathcal{F}(x, k_t) \,. \tag{2.36}$$
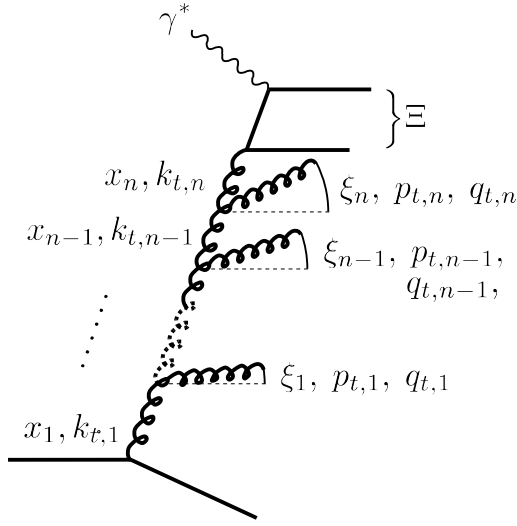
Figure 2.9: *CCFM gluon ladder with angular ordering $\xi_i > \xi_{i-1}$, where the variable ξ is related to the emission angle θ relative to the proton axis by $\xi = \tan^2(\theta_i/2)$. Ξ is related to the angle of the $q\bar{q}$ pair in the electron-proton cms with respect to proton direction and defines the upper scale for gluon emission.*

2.3.2 CCFM

The CCFM approach is an attempt to unify the DGLAP ansatz, valid at large and medium x, and the BFKL approach, valid at small x. Similar to BFKL it contains k_t-unintegrated parton densities, which are the main subject of this analysis. Therefore CCFM is presented here in more detail.

CCFM provides parton evolutions ordered in the emission angles of the partons arising from colour coherence effects in the emissions. This is illustrated in figure 2.9. In the electron-proton cms the variable ξ is connected to the emission angle θ by $\xi = \tan^2(\theta/2)$, and therefore $\theta_i > \theta_{i-1}$ leads to $\xi_i > \xi_{i-1}$.

The maximum angle allowed for emission in the gluon evolution[6] is now taken to be the angle of the quark-antiquark ($q\bar{q}$) pair in the electron-proton

---

[6]Since the Monte Carlo event generator CASCADE only includes gluon ladders, other parton evolutions are not treated here. In general CCFM provides evolution equations of gluon and quark densities.

cms with respect to the proton axis, Θ, which defines the upper boundary for gluon emission, $\Xi = \tan^2(\Theta_i/2)$.

The four-momentum of the quark pair can be written as

$$p_q + p_{\bar{q}} = \Upsilon(P + \Xi p) + Q_t = x_g(P + \Xi p) + Q_t, \qquad (2.37)$$

where P and p represent again the four-momenta of proton and electron, respectively, Q_t is the transverse momentum of the $q\bar{q}$ pair in the electron-proton cms, and the variable Υ is the longitudinal momentum fraction with respect to the proton entering the hard interaction. In case of boson gluon fusion, which is studied here, $\Upsilon \equiv x_g$, where x_g is the longitudinal momentum fraction of the gluon entering the hard scattering. In the same manner the four-momenta of the emitted gluons can be written as

$$p_i = v_i(P + \xi_i p) + p_{t,i}, \qquad (2.38)$$

$$\text{with} \quad \xi_i = \frac{p_{t,i}^2}{s v_i} \quad \text{and} \quad v_i = (1 - z_i)x_{i-1}, \qquad (2.39)$$

where $p_{t,i}$ is the transverse momentum of the ith emitted gluon.

The definition of the angular ordered region of phase space is then

$$\xi_1 < \cdots < \xi_n < \Xi. \qquad (2.40)$$

With a rescaled transverse momentum defined by

$$q_i = x_{i-1}\sqrt{s \cdot \xi} = \frac{1}{1 - z_i} p_{t,i}$$

this becomes

$$z_{i-1} q_{i-1} < q_i . \qquad (2.41)$$

The variable Ξ related to the maximum emission angle then gives an upper scale for the evolution:

$$\bar{q}^2 = x_g^2 s \cdot \Xi = \hat{s} + Q_t^2, \qquad (2.42)$$

so that the angular ordering in CCFM can be written as:

$$q_0 < q_1, \cdots, z_{i-1} q_{i-1} < q_i, \cdots, z_n q_n < \bar{q} . \qquad (2.43)$$

It can easily be shown that this angular ordering leads to strong ordering of x for small x and to ordering in k_t at large x, so that CCFM indeed covers the regions of phase space in which DGLAP and BFKL are valid.

Equation (2.42) also shows the relation of $\bar{q}$ to the factorisation scale μ_f in the collinear approach.

Evolution Equation of CCFM

The CCFM evolution equation for the gluon density can be written in integral form:

$$\mathcal{A}(x, k_t, \bar{q}) = \mathcal{A}_0(x, k_t, \bar{q}) + \int \frac{dz}{z} \int_{q_0^2}^{\bar{q}} \frac{d^2 q}{\pi q^2} \Theta(\bar{q} - zq) \Delta_s(\bar{q}, zq) \tilde{P}_{gg}(z, q, k_t) \mathcal{A}\left(\frac{x}{z}, k_t', q\right).$$
(2.44)

Here $\vec{k}_t' = |\vec{k}_t + (1 - z)\vec{q}|$, and the angular ordering is given by

$$q_0 < q_1, \quad z_{i-1} q_{i-1} < q_i, \quad z_n q_n < \bar{q}$$
(2.45)

The Sudakov form factor $\Delta_s(\bar{q}, q_0)$ gives the probability for no emission between a starting scale q_0 and $\bar{q}$. Thus, in the evolution equation (2.44) it represents the probability of no gluon emission between zq and $\bar{q}$ and therefore ensures the ordering (2.45) of the emission scales. It is defined as

$$\Delta_s(\bar{q}, q_0) = \exp\left[-\int_{q_0^2}^{\bar{q}} \frac{dq^2}{q^2} \int_0^{1-\frac{q_0}{q}} dz \frac{\bar{\alpha}_s\left(q \cdot (1 - z)\right)}{1 - z}\right],$$
(2.46)

where $\bar{\alpha}_s = 3\alpha_s/\pi$. The Sudakov form factor is a re-summation of large z contributions and thereby cancels the collinear singularity $1/(1 - z)$ of the splitting functions.

The splitting functions of CCFM are given by[3]

$$P_{gg}(z_i, q_i, k_{t,i}) = \frac{\bar{\alpha}_s(k_{t,i})}{z_i} \Delta_{ns}(z_i, q_i, k_{t,i}) + \frac{\bar{\alpha}_s(p_{t,i})}{1 - z_i}$$
(2.47)

---

[3]The choice that $\bar{\alpha}_s$ depends on the transverse momentum $p_t = q(1 - z)$, or k_t, respectively, is made because the strong ordering in k_t is not applied, so that small values of k_t leading to large $\bar{\alpha}_s$ may occur. These would not be included if the scale in $\bar{\alpha}_s$ would be fixed e. g. at Q^2.

with the non-Sudakov form factor Δ_{ns} defined by

$$\ln\Delta_{ns}(z_i, q_i, k_{t,i}) = -\alpha_s \int_{z_i}^1 \frac{dz'}{z'} \int \frac{dq^2}{q^2}\Theta(k_{t,i} - q)\Theta(q - z'q_i) \ . \qquad (2.48)$$

Equivalent to the Sudakov form factor it resums contributions of small z and thereby cancels the $1/z$-singularity. Equation (2.48) can now be written as

$$\ln\Delta_{ns}(z_i, q_i, k_{t,i}) = -\alpha_s k_{t,i}\ln\left(\frac{z_0}{z_i}\right)\ln\left(\frac{k_{t,i}^2}{z_0 z_i q_i^2}\right) \ , \qquad (2.49)$$

because the Θ-functions limit the integral over z' by $z_i \leq z' \leq \min\left(1, k_{t,i}/q_i\right)$. Here z_0 is an upper cut-off for z_i depending on the ratio of emitted and propagating transverse momentum. With this the non-Sudakov form factor can be written as an exponential series corresponding to a series of Feynman amplitudes

$$1 \ + \ \alpha_s(k_{t,i}\ln\left(\frac{z_0}{z_i}\right)\ln\left(\frac{k_{t,i}^2}{z_0 z_i q_i^2}\right) \ + \ \left(\frac{1}{2!}\alpha_s(k_{t,i}\ln\left(\frac{z_0}{z_i}\right)\ln\left(\frac{k_{t,i}^2}{z_0 z_i q_i^2}\right)\right)^2 + \ \cdots$$

The CCFM gluon densities can be compared to the DGLAP like gluon densities by

$$x f_g(x, \mu_f) \simeq \int^{\mu_f} \frac{dk_t^2}{k_t^2}\mathcal{A}(x, k_t, \bar{q}) \ . \qquad (2.50)$$

The Soft Region of Phase Space

In the DGALP approach the non-perturbative terms of the soft region were included in the initial parton distribution as outlined in section 2.2.2. Due to the strong ordering the transverse momentum of partons in the evolution cannot fall below the cut-off scale κ. In the CCFM approach a lower cut-off k_t^{cut} is used for calculation of the initial parton density $\mathcal{A}_0(x, k_t, \bar{q})$, but the transverse momentum of partons in the evolution can still achieve values in the non-perturbative soft region below k_t^{cut} where the coupling constant $\bar{\alpha}_s(\mu)$ becomes large. A practical solution is to simply restrict the evolution in k_t to values $k_t > k_t^{\text{cut}}$, while $\bar{\alpha}_s(\mu)$ is fixed for $\mu < q_0$.

A Closer Look at the Splitting Functions

The splitting function (2.47) contains only collinear and soft singular terms $1/z_i$ and $1/(1-z_i)$, respectively. Although at asymptotically high energies effects from non-leading contributions can be neglected, they might play a role at energies currently available at colliders. This can be taken care of by including non-singular terms in the splitting functions, but Δ_s and Δ_{ns} then have to be changed accordingly. How this is done is presented in [10] and [11].

Another possible modification of the splitting function effects $\bar{\alpha}_s$: instead of using different scales for the soft and the collinear term in (2.47) one can also use $p_{t,i}$ in both scales:

$$P_{gg}(z_i, q_i, k_{t,i}) = \frac{\bar{\alpha}_s(p_{t,i})}{z_i}\Delta_{ns}(z_i, q_i, k_{t,i}) + \frac{\bar{\alpha}_s(p_{t,i})}{1-z_i} \, , \qquad (2.51)$$

which also has to be considered in the non Sudakov form factor [10, 11].

How the inclusion of non-singular terms as well as changes to the splitting functions effect the unintegrated gluon densities of CCFM is examined in the next section.
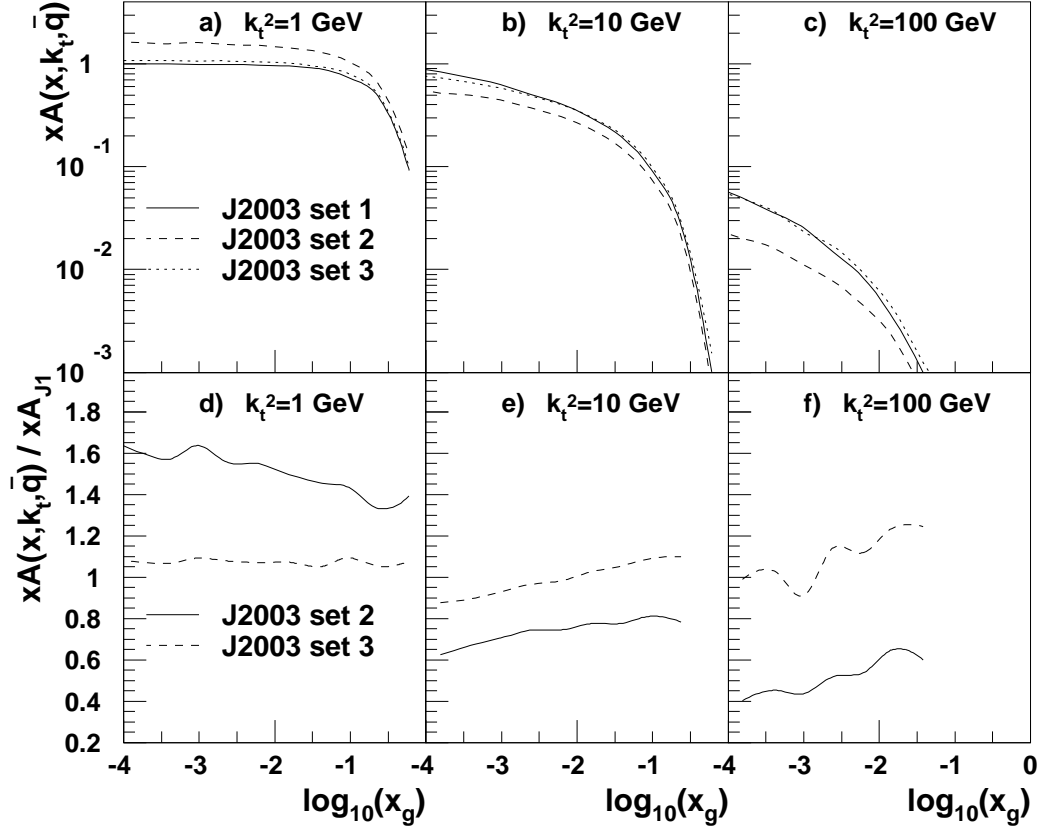
Figure 2.10: *Comparison of three sets of CCFM gluon densities $x\mathcal{A}(x, k_t, \bar{q})$ as functions of $\log x$ at three different k_t^2 (a-c), and the ratios of set 2 and set 3 with respect to the first set (d-f).*

2.4 Unintegrated Gluon Densities

Three different sets of unintegrated gluon densities are used in this thesis (taken from [12]):

- *J2003 set 1*
  This set of unintegrated gluon densities contains the splitting function (2.47) and a collinear cut-off $k_t^{\mathrm{cut}} = q_0 = 1.33$ GeV.
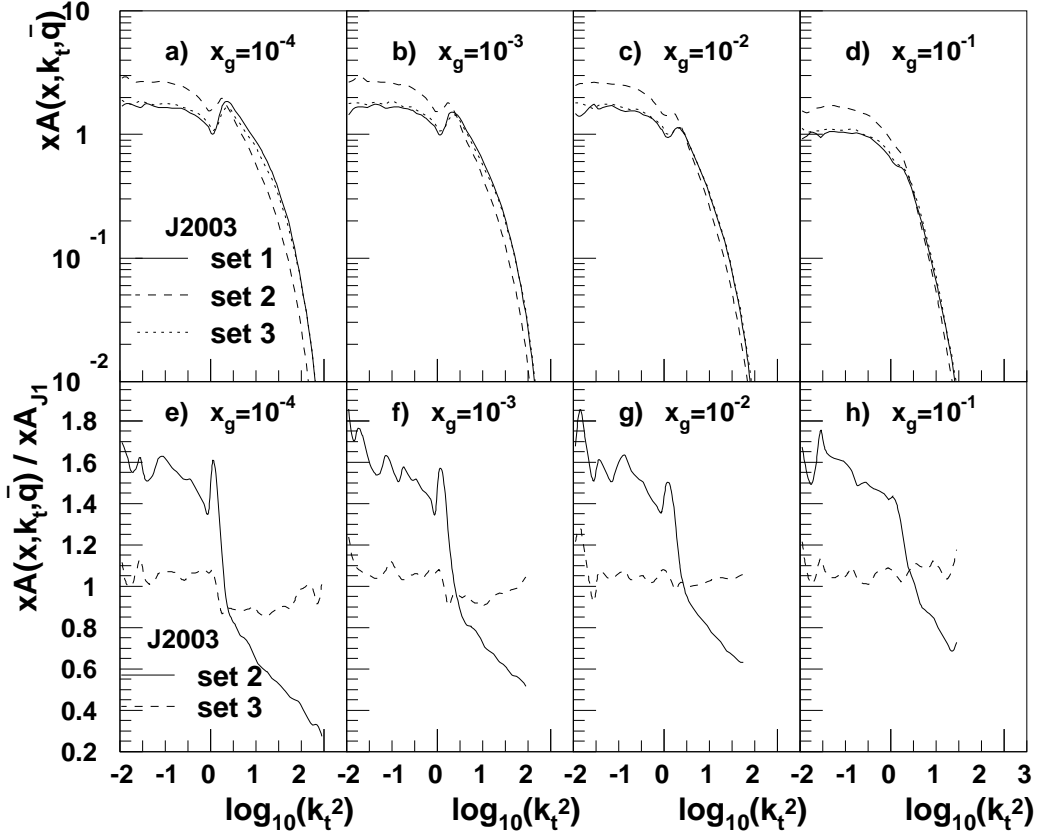
Figure 2.11: *Comparison of three sets of CCFM gluon densities $x\mathcal{A}(x, k_t, \bar{q})$ as functions of $\log k_t^2$ in bins of x_g (a-d), and the ratios of set 2 and set 3 with respect to the first set (e-h).*

- *J2003 set 2*

  Here the improved splitting function containing non-singular terms was used and the collinear cut-off was $k_t^{\mathrm{cut}} = q_0 = 1.18$ GeV.

- *J2003 set 3*

  The change to the scale in $\bar{\alpha}_s$ was included here in a splitting function excluding non-singular terms (eq. 2.51). $k_t^{\mathrm{cut}} = q_0 = 1.35$ GeV was taken as a collinear cut-off and $\bar{\alpha}_s(\mu)$ was fixed for $\mu < 0.9$ GeV.
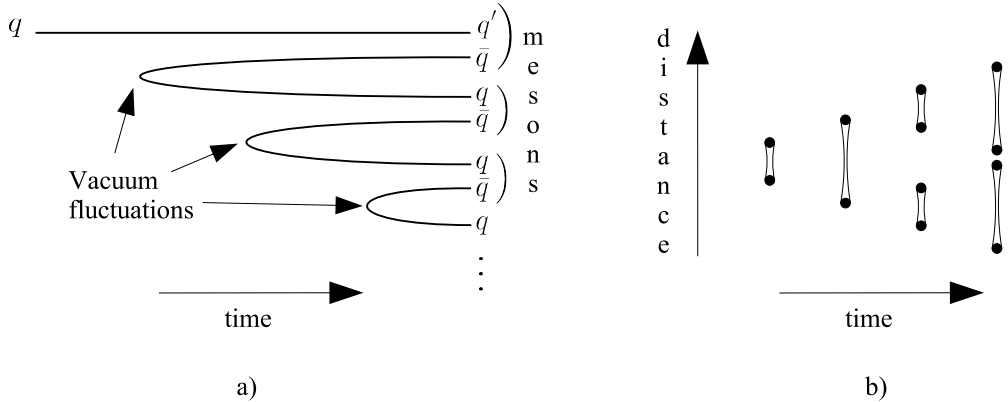
Figure 2.12: *The formation of hadrons by quarks is illustrated using a) the independent fragmentation model and b) the Lund string model.*

These uPDFs are compared in figures 2.10 and 2.11. Figures 2.10a to c show the gluon distributions $x\mathcal{A}(x, k_t, \bar{q})$ as functions of $\log x$ for three different values of k_t, while figures 2.10d to f show the ratio of set 2 and 3 with respect to the first set. Figures 2.11a to d and figures 2.10e to h, respectively, show the same as functions of $\log k_t^2$ for four different values of x_g.

At low x_g the gluon densities show a certain saturation behaviour, which is most distinct for $k_t^2 = 1$ GeV^2.

From figures 2.10d to f and 2.11e to h it is obvious that the non-singular contributions included in set 2 lead to significant deviations from the gluon density using the original splitting function (set 1). Furthermore the contribution of the non-singular parts in the splitting functions effect the soft region most, in which set 2 exceeds the other gluon densities. In comparison the effect of changing the scale in $\bar{\alpha}_s$ is not as large.

2.5   Fragmentation and Hadronisation

The process of forming hadrons out of partons is called *hadronisation*, but sometimes also referred to as *fragmentation*. In a more differentiated terminology fragmentation describes the QCD processes occurring after the hard scattering but before the hadronic final state is formed. It is then said that

the partons *fragment* by gluon radiation, gluon splitting and similar QCD processes before hadrons are actually formed. But since it is not clear 'when' a group of partons may be considered a hadron, these terms are mostly used in a similar manner. In addition hadrons may also radiate gluon and thereby fragment further, so that a clear distinction is not possible. The only distinction that can be made is that between parts that can and parts that cannot be treated perturbatively.

2.5.1 Parton Showers

In Monte Carlo generators the perturbative part of fragmentation is usually described by *final state parton showers*. The methods are similar to the methods used in the initial state parton evolution, except that parton emissions are now time like, whereas they are space like in initial state parton evolution. This part usually treats the transition from partons *off mass-shell*, meaning that their masses may differ from their actual mass, to partons on mass-shell.

2.5.2 Independent Fragmentation

The independent fragmentation model describes fragmentation and hadronisation by assuming that a quark combines with quarks created from vacuum fluctuations to hadrons as sketched in figure 2.12a. The picture also illustrates that the last quark is left over concerning colour and flavour conservation, so that a treatment of colour and flavour neutralisation has to be introduced. In the hadronisation model described in the next section colour neutralisation is always ensured.

2.5.3 The Lund String Model

The Lund string model is sketched in figure 2.12b. In QCD the colour force between two coloured objects increases with distance. This is modelled by strings connecting two coloured objects that break up when the distance between the objects becomes too large. The colour strings are treated as colour
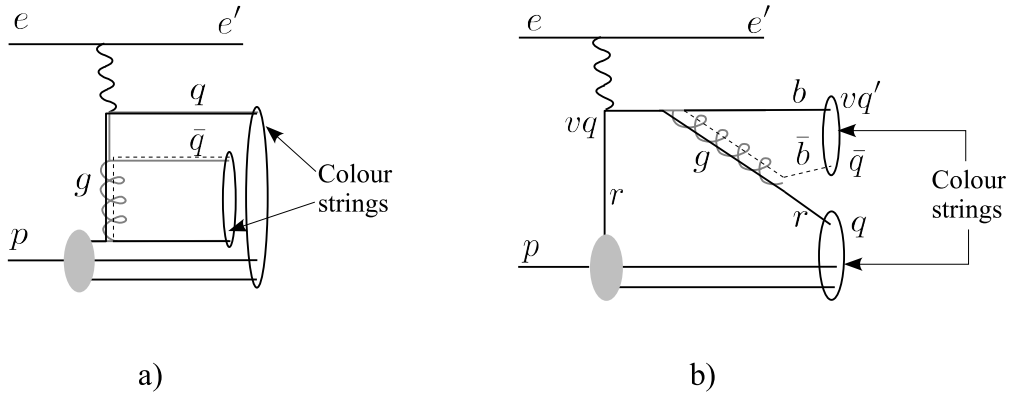
Figure 2.13: *Lund strings illustrated in two processes: in BGF (a) both quarks of the diquark system are still connected to the proton remnant via a colour string, while in a QCD Compton process with a valence quark (b) the scattered quark is not connected to the proton remnant anymore. The solid and the dashed lines illustrate the colour and anticolour flow, respectively, and r, b and $\bar{b}$ indicate the colours red, blue and antiblue.*

singlet states that connect either a quark-antiquark pair or three quarks that are combined to a colourless state. Thus no net colour charge can be created in the process, so that the colour neutrality is already assured.

Figure 2.13 illustrates the situation in *ep*-scattering: after the hard interaction the quarks are connected to the proton remnant by a colour string. The difference between BGF (fig. 2.13a) and QCD Compton (QCDC) involving a valence quark (fig. 2.13b) is the following: in BGF the gluon carries colour from the proton, and the quarks q and $\bar{q}$ both obtain this colour. In this way, both quarks are connected to the proton remnant by a colour string. In QCDC including a valence quark vq this carries colour, but no anticolour that is connected to the proton remnant. The anticolour is not created until the gluon is emitted, and then it is associated with the colour of the former valence quark. In this way, the antiquark $\bar{q}$ originating from the gluon is connected to the former valence quark vq', and the quark q originating from the gluon is connected to the proton remnant.
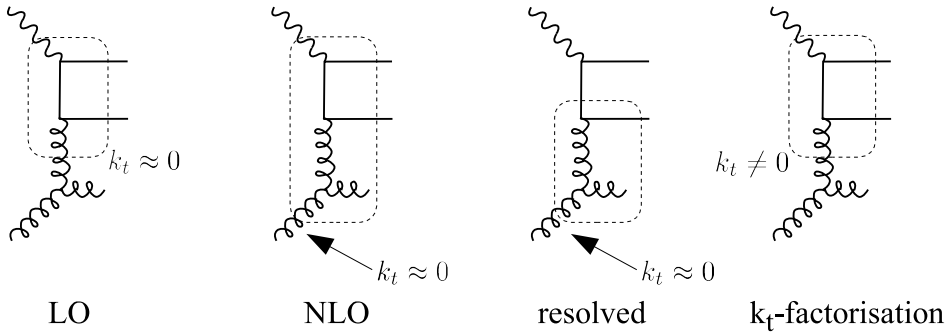
Figure 2.14: *Illustration of matrix elements of a) collinear LO, b) collinear NLO, c) collinear resolved processes and d) k_t-factorisation. The dashed boxes indicated the matrix elements.*

2.6 Photoproduction

The kinematic region of low virtualities, usually defined by $Q^2 < 1$ GeV^2, is called *photoproduction* because then the photon can be considered as quasi-real. In this region of low photon virtualities the virtuality of the gluon entering the hard scattering might play a role. Since in the collinear approach the gluon virtuality is always neglected so-called *resolved photon* processes have to be introduced. In this model the photon fluctuates into either a quark-antiquark pair (*anomalous resolved* case) or a vector meson with a hadronic substructure (*normal resolved* case).

In the first case the hard scattering is described by the interaction of, e. g., a gluon from the proton with neglected virtuality and a quark or antiquark from the photon by the exchange of a gluon. This is indicated in figure 2.14. Collinear LO (fig. 2.14a) neglects the gluon virtuality. Collinear NLO (fig. 2.14b) includes processes where the incoming gluon virtuality is still neglected, but the emission of another gluon is included in the hard scattering matrix element. The resolved model (fig. 2.14c) now treats the hard scattering as an interaction between a quark from the photon and a gluon from the proton, as indicated by the dashed box. Thereby the gluon which in collinear LO is treated massless and collinear to the proton, $k_t \approx 0$, can now attain finite virtuality and k_t. The gluon *entering the hard scattering*, however, is still considered massless and collinear to the proton.

a)   b)
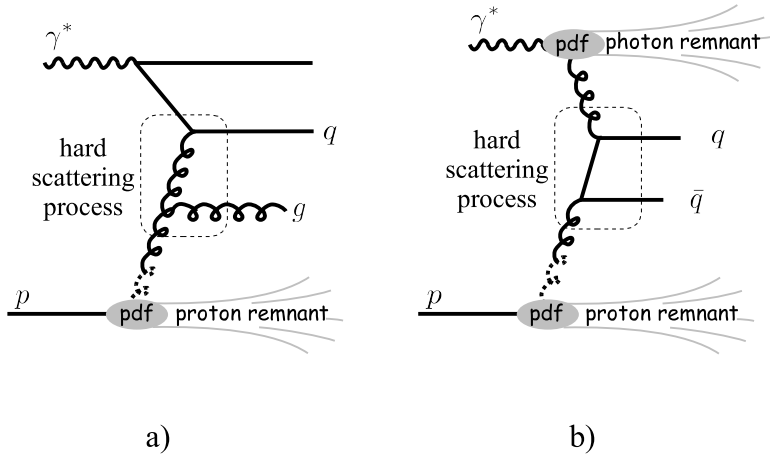
Figure 2.15: *Resolved photon processes: In a) an example of the anomalous resolved case is shown, where a gluon from the proton interacts with a quark from the photon. In b) the normal resolved case is shown in an example of gluon gluon fusion, where two gluons from both proton and photon interact.*

The normal and anomalous cases are illustrated in figure 2.15a and b, respectively. To describe the hard scattering in the resolved photon model a parton distribution function $f_{i/\gamma}(x_\gamma, \mu_f)$ is introduced. Here x_γ is the fraction of the photon momentum entering the hard interaction and μ_f is the factorisation scale. In the hard scattering a parton from the proton then interacts with a parton from the quasi-real photon, be it a quark or antiquark in the anomalous case or a quark, antiquark or gluon in the normal resolved case.

The cross section for resolved processes can be written as a convolution of parton densities from the proton and a hard scattering cross section, but now the quasi-real photon structure also has to be considered by including its parton density:

$$\sigma \sim \int \frac{dx_p}{x_p} \int \frac{dx_\gamma}{x_\gamma} \sum_{i,j} f_{i/p}(x_p, \mu_f) f_{j/\gamma}(x_\gamma, \nu_f) \hat{\sigma}_{ij} , \qquad (2.52)$$

where $\hat{\sigma}_{ij}$ describes the hard interaction of a parton i from the proton and a

parton j from the photon. The momentum fraction x_γ can be written as[4]

$$x_\gamma = \frac{\sum_i E_{T,i} e^{\eta_i}}{2yE_e} \ , \tag{2.53}$$

where the sum is taken over the particles leaving the *hard interaction*. In figure 2.15a these are the antiquark q from the photon and the emitted gluon g, while in figure 2.15b they are indicated by q and $\bar{q}$. E_e is the energy of the electron beam and y the inelasticity. The *transverse energy* of a particle is defined by

$$E_{T,i} := \sqrt{E_i^2 - p_{z,i}^2} \ , \tag{2.54}$$

and the pseudo-rapidity $\eta = -\tfrac{1}{2}\ln(\tan(\theta/2))$ is a measure for the angle θ between particle and proton.

The momentum fraction x_γ can also be interpreted as the momentum fraction of the photon entering the quark-antiquark ($q\bar{q}$) pair in BGF. In direct collinear processes four-momentum conservation dictates that the quarks of the $q\bar{q}$ pair cancel in transverse momentum. This forbids further gluon emissions in the hard scattering, because transverse momentum would not be conserved by such an emission. Therefore direct processes are characterised by $x_\gamma = 1$, because the full photon momentum enters the diquark system.

Resolved processes, on the other hand, are characterised by $x_\gamma < 1$, since this is only possible when the gluon is allowed finite virtuality and transverse momentum.

Note that the resolved model is only considered in collinear LO. In k_t-factorisation as well as collinear NLO the introduction of such a model is not necessary because the gluon is treated off mass-shell and may therefore have finite virtuality. Processes with $x_\gamma < 1$ are therefore naturally included in the matrix elements. The hadronic component of the photon, however, is not considered. w

2.7 Heavy Flavour Production

Since the centre-of-mass energy at HERA is not large enough two produce a top quark pair, only charm and beauty production are considered here.

---

[4]In [13] a derivation of x_γ is can be found.
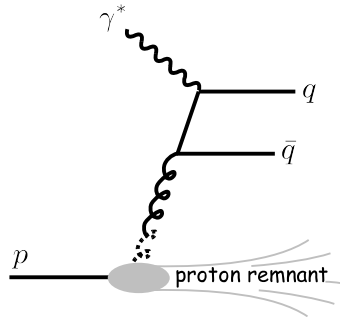
Figure 2.16: *Direct boson gluon fusion process where the photon is considered to be point like*

The production of heavy quarks differs from light quark production in that the mass of the heavy quarks provides a hard scale for the scattering while the masses of the light quarks u, d and s are always neglected. Because of this heavy quark production ensures that perturbative methods can be applied, but the treatment of the heavy flavour now depends on the energy scale. At HERA most heavy quarks are produced at scales near production threshold, $\mu \approx m_Q$ (the capital Q indicates heavy flavour), where BGF processes make the dominant contribution. At moderate x heavy quarks are not treated as partons of the proton but as particles created in the hard process. In the collinear approach at scales $\mu \gg m_Q$ heavy quarks are treated similar to light quarks and are therefore considered partons of the proton.

In the study of heavy flavours the properties of the quarks are reconstructed by investigation of hadrons formed by the quarks or of decay particles of the quarks. Charm quarks, for example, are often reconstructed via the study of $D^{*\pm}$-mesons, but also tagging one one quark by a D^* and the other by muon (fig. 2.17). Beauty quarks are mainly reconstructed by studying muons from their decay. If jets are used in heavy flavour they are associated with a D^* and muons.

In most heavy flavour studies the transverse momentum and the pseudo rapidity η of D^*-mesons or muons are measured. To find out if these observables are sensitive to the phase space of the gluon entering the hard interaction is one of the main goals of this thesis.
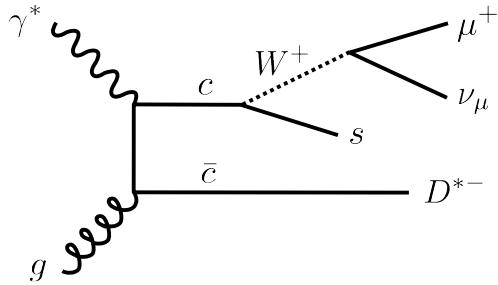
**Figure 2.17:** *Example of charm production via BGF: a charm quark decays semileptonically while the anticharm hadronises into a D^{*-}-meson.*

2.8 Jet Production

As described above particles in the final state are subject to fragmentation, parton showers and hadronisation. A final state parton may radiate gluons that further split into quarks, and out of all these particles the hadronic final state is build. Thus many hadrons may originate from one quark of the final state of the hard scattering and to reconstruct the properties of the final state quarks one now combines hadrons moving approximately in the same direction into a *jet*.

2.8.1 Jet Algorithms

The definition of a jet is not unique because one has to decide whether two particles are 'close enough' to be considered part of the same jet or whether two *sub jets* have to be considered as two different jets. For a clear identification of jets certain *jet algorithms* are used. In the k_t-jet algorithm [14], for example, user defined objects are treated as so-called *proto jets*, which are compared in transverse momentum p_t, pseudo-rapidity η and azimuthal angle ϕ. These objects may be partons in Monte Carlo simulations, hadrons reconstructed from tracks and calorimeters or tracks and clusters in the calorimeters[5]. The masses of the proto jets are neglected. If the distance of two proto jets i and j defined by

$$d_{ij} := \min\left(p_{t,i}^2, p_{t,j}^2\right)\left((\eta_i - \eta_j)^2 + (\phi_i - \phi_j)^2\right) , \qquad (2.55)$$

---

[5]Experimental methods to detect particles are discussed in section 1.2

is greater than the transverse momentum of at least one of the proto jets, the proto jet is considered a jet and removed from the list of proto jets to be compared. If d_{ij} is smaller than both transverse momenta of the proto jets, they are merged into one proto jet by determining combined transverse momenta, pseudo-rapidity and azimuthal angle depending on the proto jet variables. The comparison then continues until no proto jets are left.

2.8.2 Jet Variables

In this thesis jets are studied in heavy quark production or in dijet events which contain at least two jets. Instead of the transverse momentum jet analyses study the transverse jet energy defined by

$$E_{T,jet} := \sqrt{E_{jet}^2 - p_{z,jet}^2} \qquad (2.56)$$

The energy E_{jet} of the jet is measured in the calorimeter, and the projection on the z axis defines $p_{z,jet}$. Since the mass of a jet is not properly defined, transverse momentum and transverse energy are taken to be equal.

Comparing this with equation (2.53) one can now use the transverse energy and the pseudo-rapidity of the jets to approximate x_γ by

$$x_\gamma^{obs} = \frac{\sum_{jets} E_T^{jet} e^{-\eta^{jet}}}{2 E_e y} \, , \qquad (2.57)$$

where the sum runs over the jets in the final state.

Figure 2.18 illustrates why x_γ is expected to be a variable sensitive to the transverse momentum of the hard interacting gluon. It is assumed that in a dijet event the jets with the highest transverse energy are studied. If $x_\gamma \approx 1$ (direct process, fig. 2.18a), the transverse momenta of the two jets balance, as already stated in section 2.6. The gluon, therefore is collinear with the proton and on-shell, i. e. massless. Here the measured jets originate from the diquark system.

If, on the other hand, $x_\gamma < 1$ (resolved process in collinear factorisation, fig. 2.18b), four momentum conservation forbids that the diquark system can be the source of two jets with high transverse energy. Thus one of the jets
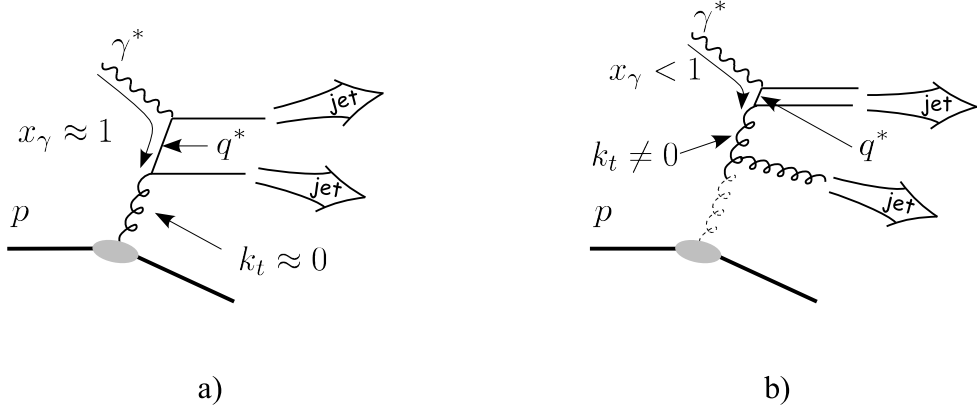
Figure 2.18: *Sensitivity of x_γ to the transverse momentum k_t of the hard interaction gluon: In a) the transverse energy of the jets balance and no virtuality and transverse momentum are required from the incoming gluon, $k_t \approx 0$. In b) 4-momentum conservation forbids the production of high E_T jets from the diquark system.*

with large E_T has to originate from the emitted gluon. But if the transverse momentum of the emitted gluon is large, four momentum conservation requires a propagating gluon with large transverse momentum. This is why low x_γ are sensitive to large k_t and high x_γ are sensitive to small k_t. Therefore x_γ presents the opportunity to study the transverse momentum of gluons in different regions of phase space.

Chapter 3

Monte Carlo Event Generators

Simulating processes of high energy physics with Monte Carlo techniques is a common way to compare theoretical predictions to measurements and to fit theoretical parameters to data that cannot be predicted by theory itself. These simulations are often referred to as event generators or simply Monte Carlos (MCs).

In this chapter the basic mechanisms of event generators and the generators used in this thesis are presented and important parameters are introduced.

3.1   Mechanisms of Monte Carlo Event Generators

Monte Carlo event generators calculate hard scattering matrix elements and branching probabilities with Monte Carlo methods to generate partons and then final states on hadron level. The generation process can roughly be divided into a few elementary steps shown in figure 3.1: First the matrix element of the hard scattering is calculated, then initial parton showers are applied via the corresponding evolution equations. After that parton showering is applied to the final state out of which, finally, hadrons are build.

For the initial state radiation a forward evolution approach is possible, where parton showers are calculated with evolution equations from starting
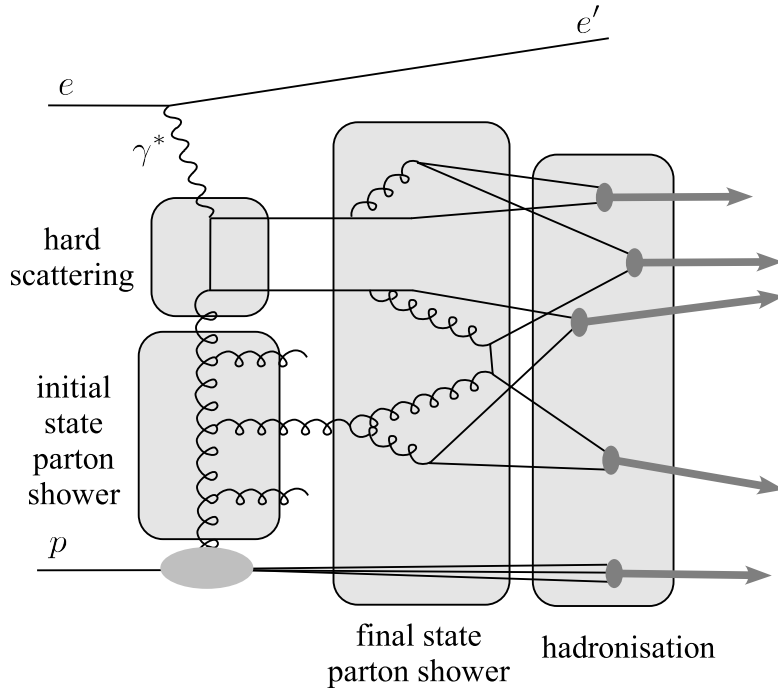
Figure 3.1: *Schematic division of event generation into calculation of hard scattering matrix, initial state parton showers, final state parton showers and hadronisation.*

values until some stopping conditions are met. In this case the matrix element would be calculated after the momentum of the parton entering the hard interaction is calculated. However, this turns out to be inefficient because it is possible that the available phase space does not allow for a hard scattering, and because it is too likely to create branchings that contribute insignificantly to the cross section. Therefore the *backward evolution* method is chosen.

3.1.1   Backward Evolution

In this approach the hard scattering matrix element (dashed boxes in fig. 3.2) is evaluated first, giving for example the upper scale for the parton evolutions.
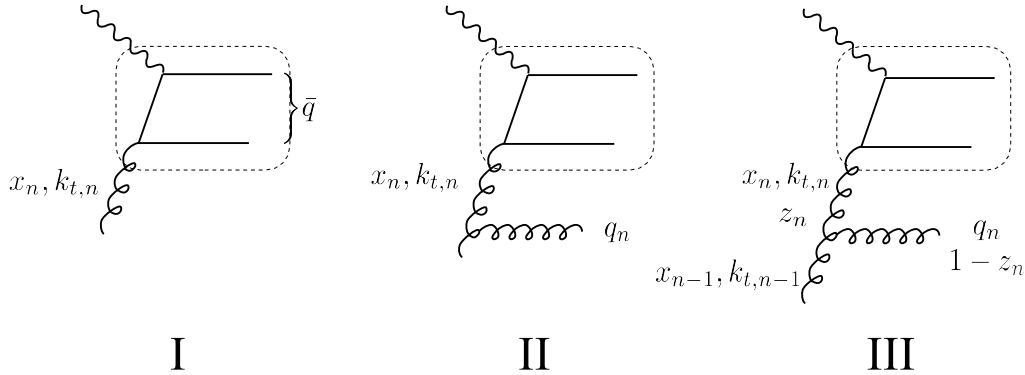
Figure 3.2: *Backward evolution of initial state parton emission in event generators. The matrix element is indicated by the dashed box.*

Backward Evolution for DGLAP

In the collinear approach the evolution equations give no restrictions for the emitted gluons. Thus, after the matrix element is generated and the factorisation scale calculated, the evolution starts by generating the final parton f of the evolution according to $x_f > x$, where x is the longitudinal momentum fraction of the quark struck by the photon, and $k_{t,n}^2 \ll \mu_f$ by using random numbers to calculate the momenta. After that, the backward evolution repeats this step according to the strong ordering of virtualities k^2 in DGLAP (eq. (2.28)), and considering $x_{i-1} > x_i$ until a lower cut-off for k^2 or an upper cut-off for x_i is reached. The emitted gluons are generated in the process according to momentum conservation.

Backward Evolution for CCFM

In CCFM $\bar{q}$ is given by the opening angle Θ of the diquark system. From here on the evolution is done backwards by calculating the scale q_n of the last emission in the ladder (fig. 3.2.II) with the probability of emission given by the Sudakov form factor $\Delta_s(\bar{q}, q_n)$ (eq. (2.46)). As already mentioned above this gives the probability of *no emission* between $\bar{q}$ and q_n, so that q_n is chosen according to the Sudakov form factor. With $k_{t,n}$ and q_n already known z_n can now be determined via the splitting function, and after that x_{n-1} and $k_{t,n-1}$ are calculated (fig. 3.2.III).

This procedure is then repeated until a lower cut-off scale is reached. Initial momentum fraction x_0 and transverse momentum $k_{t,0}$ are determined, the proton remnant is build and $k_{t,0}$ is added to the quark-diquark system of the proton remnant.[1]

This procedure is very well suited for initial state parton showering, because here it is more efficient than the forward approach. However, complication arise because the transverse momentum is actually a vector, so that the azimuthal angle ϕ also has to be considered. In addition the transverse momentum of an incoming gluon enters the non-Sudakov form factor, the splitting function and the parton density, which also causes difficulties in this approach.

3.1.2　Final State Parton Showers - the Forward Method

For parton showers in the final state a forward method is used. Here this is easier to do since there are no parton densities that have to be considered in the evolution.

The showering is also described using the Sudakov form factor to give the probabilities of the splittings, and the splitting is repeated until all partons are on mass shell, where the upper scale for emission is, for example, given by the proton-photon cms energy $W_{\gamma p}$. After that hadronisation models are applied to the partonic final state.

3.2　The Event Generator RAPGAP

The Monte Carlo event generator RAPGAP [15] implements the DGLAP evolution equations and the Lund string model for hadronisation. It is applicable in *ep*-scattering in various kinematic regimes. Processes in direct photoproduction as well as in deep inelastic scattering can be simulated. Resolved processes, also for DIS, can be chosen separately. In addition diffractive QCD

---

[1]If a valence quark is interacting with the photon, e.g. in $\gamma^* q \to q\,g$, the proton remnant is treated as a di-quark system, while in BGF it is treated as a system of a single quark and a di-quark.

Parameter	Value	Function
IPRO	13/14	selecting BGF-processes for light/heavy quarks
INPR	1004046	proton structure function CTEQ 5L
PARU 112	0.192	Λ_{QCD}
PARJ 54	0.05	ϵ_c for Peterson fragmentation function
PMAS 4	1.5	mass of the charm quark in GeV
PMAS 5	4.8	mass of the beauty quark in GeV

Table 3.1: *Main steering parameters for the* RAPGAP *Monte Carlo event generator.*

processes are implemented where a colour singlet state is exchanged in the interaction processes and hence a gap in rapidity is observed in the data.[2].

In this thesis the RAPGAP Monte Carlo was used to compare description of the data by the CCFM approach to standard DGLAP. This was done with the steering parameters displayed in table 3.1.

The parameter Λ_{QCD} is the scale at which the coupling gets large and enters the matrix element as well as as the parton and gluon densities. The choice depends on the structure function used and was chosen to account for the structure function CTEQ 5L from the CTEQ collaboration.

In RAPGAP only boson gluon fusion processes are selected. Since BGF is the dominant production mechanism of heavy quarks, and since the CASCADE event generator includes only boson gluon fusion processes, this still provides the possibility to compare the results from the two event generators to heavy quark data.

The energy of the electron and the proton beam were tuned to $E_e = 27.5$ GeV and $E_p = 820$ GeV, respectively. The latter choice was made for considering that most of the measurements that are studied here took place with that proton energy.

[2]For a detailed description see [15]
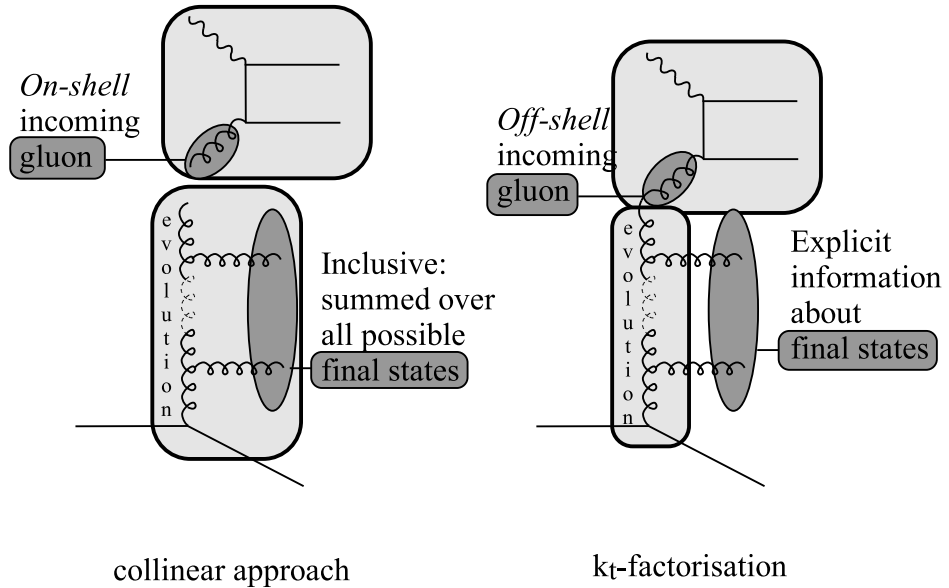
Figure 3.3: *On the left hand it is illustrated how the collinear approach sums over all final states of the gluon cascade, while angular ordering gives explicit information about this (right hand figure). In addition the former approach takes the incoming gluon in the hard scattering to be on-shell, while in the latter it is taken to be off-shell.*

3.3   CASCADE - an Implementation of CCFM

The Event Generator CASCADE also uses the Lund string fragmentation model but implements CCFM unintegrated gluon densities to simulate the proton structure. Up to now this excludes processes like $\gamma^* q \to q\,g$ and only boson gluon fusion processes, $\gamma^* g \to q\,\bar{q}$, are taken into account.

The gluon evolution is done via the backward method as described in section 3.1.1. The CCFM evolution is suited especially well for Monte Carlo Simulation, because evolution equations using angular ordering give explicit informations about the final state in the gluon evolution, meaning the emitted gluons (fig. 3.3). In contrast to that the collinear approach sums over all possible final state configurations and therefore cannot give explicit information about the final states of partons emitted in the evolution.

Also the collinear approach uses on-shell matrix elements, meaning that

Parameter	Value	Function
IPRO	11/12	selecting light/heavy flavours
IGLU	1001 - 1003	gluon densities J2003 set 1 - 3
PARU 112	0.2	Λ_{QCD}
PARJ 54	-0.05	ϵ_c for Peterson fragmentation function
PARJ 55	-0.005	ϵ_b for Peterson fragmentation function
PMAS 4	1.5	mass of the charm quark in GeV
PMAS 5	4.8	mass of the beauty quark in GeV

Table 3.2: *Main steering parameters for the* CASCADE *Monte Carlo event generator.*

the mass of the gluon entering the hard interaction vanishes. Since the gluon at the upper end of the evolution must have a finite virtuality for kinematical reasons, this leads to problems when implementing the DGLAP approach into Monte Carlos, because the evolution then has to be fit to the matrix element. In k_t-factorisation the matrix elements are calculated off-shell with a gluon with finite virtuality, so that these problems do not arise.[3]

The most important steering parameters are given in table 3.2. The parameters mostly agree with the ones used in RAPGAP, with exception of the structure function, which here are replaced by the gluon densities presented in section 2.4, and the scale Λ_{QCD}. As in RAPGAP Λ_{QCD} is chosen to match the scale used in the uPDFs. The parameters ϵ_c and ϵ_b are needed for the Peterson fragmentation function used in the Lund fragmentation model and are chosen according to [17].

Up to now the event generator CASCADE only implements gluon evolution following the CCFM equations. Before quark densities can also be included, a detailed knowledge of the gluon behaviour is desired. In this the-

---

[3]However, in [16] the authors argue that k_t-factorisation still does not consider the full 4-momentum of the gluon, because the parton densities depend only on the longitudinal momentum fraction and the transverse momentum. The gluon virtuality still does not enter the kinematics. For a correct treatment of the hard scattering fully unintegrated parton densities are necessary that include the full four momentum of the hard interacting parton.

sis it will be shown which region of the phase space of the hard interacting gluon is available to present HERA measurements. This will indicate which measurements can be used to further constrain unintegrated gluon densities, and in which region further measurements are needed for such a constraint.

Chapter 4

Hadronic final state measurements

In chapter 5 differential cross sections as functions of k_t and x_g are investigated to identify regions of the gluon phase space which is accessible to present HERA measurements.

To accomplish this for several measurements the Monte Carlo interface HzTool is used.[1] HzTool implements a set of Fortran routines to compare Monte Carlo predictions with measured data. Each HzTool routine contains data of the associated publication and allows the user to compare it with the Monte Carlo predictions. This is done by applying kinematical cuts or other selection criteria of the measurement (e.g. demanding at least two jets for dijet events) to the hadronic final states from a Monte Carlo event generator.

To investigate the sensitivity of HERA measurements to the gluon phase space the HzTool -routines have been modified to calculate distributions of k_t and x_g in kinematic regions of the measurements. In addition k_t and x_g are investigated in bins of certain observables which are used in the measurements, like p_{T,D^*} and η_{D^*}, to study their sensitivity to the gluon variables.

---

[1]A manual containing a short description of all available routines can be found at *http://hepforge.cedar.ac.uk/hztool/docs/hztool.pdf.*

The data studied here were published and also printed in DESY red reports. For easy reference the DESY numbers of the publications are given.

4.1   Analysed Measurements and Comparison of Monte Carlo Predictions to Data

This section gives an overview of the measurements of both H1 and ZEUS which are investigated in this analysis. Objectives and certain specialities of the measurements are described for each publication. Furthermore selected control plots are presented to show how accurately the individual measurements are described by the Monte Carlo calculations. The CASCADE calculations are shown without error bars, because only statistical errors occur which are very small for most of the analyses. Whenever statistical errors are of noticeable size they are shown in the plots.

Heavy flavour and dijet processes are covered in the separate sections 4.1.1 and 4.1.2. The HZTOOL routine for the investigation of charm events with D^*-muon tagging developed during the course of this analysis is presented in more detail in section 4.2. This also serves as an example of the structure of an HZTOOL analysis routine.

4.1.1   Investigation of Heavy Quark Production

Heavy flavours are analysed in photoproduction regime as well as in deep inelastic scattering. Also heavy flavour measurements including dijets are introduced at the end of the section.

DESY 98-085: Inclusive $D^{*\pm}$ and associated Dijet Measurement in photoproduction (ZEUS)

In an inclusive D^*-meson analysis two jets were used in [18] to tag the $q\bar{q}$ system of the boson gluon fusion process. One of the jets was associated with the D^*-meson. The centre-of-mass energy of the photon-proton-system was

restricted to 130 GeV $< W_{\gamma p} <$ 280GeV. The selection criteria for the jets are $|\eta_{jet}| < 2.4$ for both jets and $E_{T,jet\,1} > 7$ GeV for the jet with the highest and $E_{T,jet\,2} > 6$ GeV for the jet with the second highest transverse energy. At least one D^* was requested to fulfil $p_{T,D^*} > 3$ GeV and $|\eta_{D^*}| < 1.5$. A comparison of the measured data to three unintegrated gluon densities in CASCADE is given in section 4.3.

DESY 03-015: Dijet Angular Distributions in Photoproduction of Charm at HERA (ZEUS)

Angular distributions of dijets associated with D^* production has been measured in photoproduction ($Q^2 < 1$ GeV^2) with the ZEUS detector. The hadronic cms energy was restricted to $130 < W_{\gamma p} < 280$ GeV^2. The jets were restricted to $E_T^{jet} > 5$ GeV and $|\eta^{jet}| < 2.4$, and the D^*-meson had to fulfil $p_{t,D^*} > 3$ GeV and $|\eta^{D^*}| < 1.5$.

DESY 99-101: $D^{*\pm}$ Production and the Charm Contribution to F_2 in DIS (ZEUS)

A measurement by ZEUS of the charm contribution to F_2 in DIS (1 GeV$^2 < Q^2 < 600$ GeV^2) was investigated in [19]. The events were required to fulfil

$$0.02 < \quad y \quad < 0.7$$
$$1.5 \text{ GeV} < \quad p_{T,D^*} \quad < 15 \text{ GeV}$$
$$|\eta_{D^*}| \quad < \quad 1.5 \,.$$

The data are compared to CASCADE computations in figure 4.1. Figure 4.1a shows the charm contribution to the structure function of the proton, F_2^c, as a function x_{Bj}, for low virtualities of $Q^2 = 7$ GeV^2 and for higher virtualities of $Q^2 = 60$ GeV^2. All the calculations are in good agreement with the data
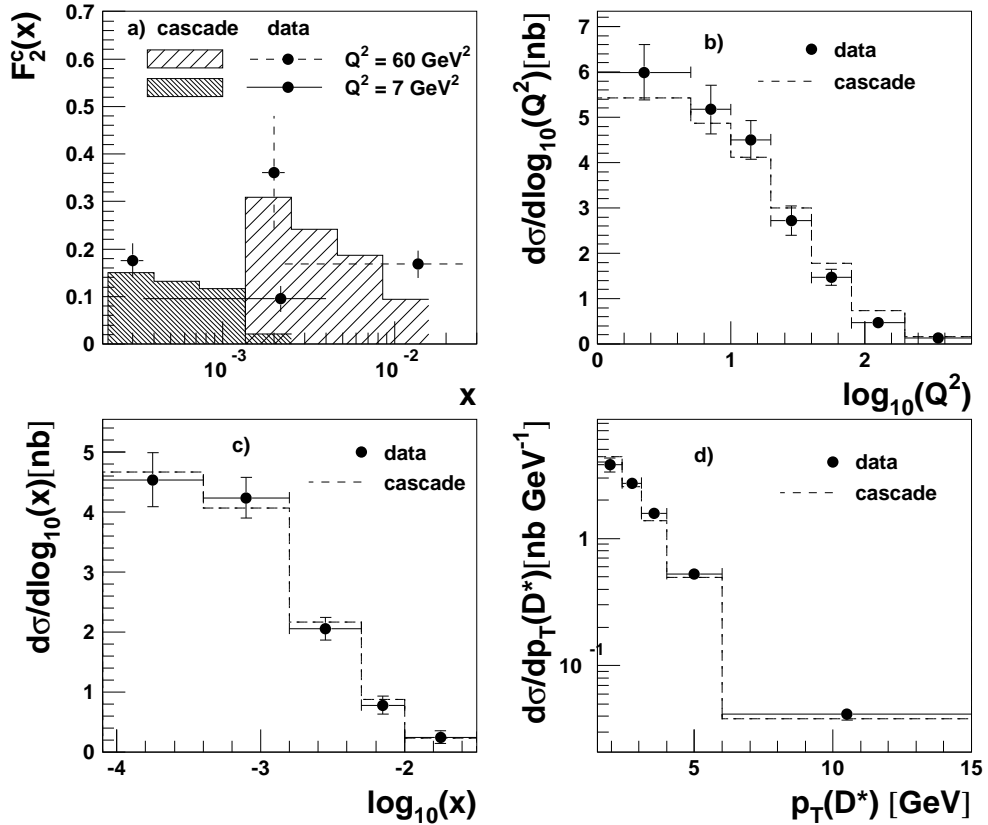
**Figure 4.1:** *DESY 99-101: a) shows the charm contribution to $F_2(x)$ for $Q^2 = 7$ GeV^2 (solid line, dense hatching) and $Q^2 = 60$ GeV^2 (dashed line, light hatching). The dots represent the data points and the hatched areas represent bins of* CASCADE *calculations. In b), c) and d) differential cross sections as functions of $\log Q^2$, $\log x$ and p_{T,D^*}, respectively, are shown, where the dots represent the data with systematic and statistical errors added in quadrature.*

DESY 01-100: Inclusive $D^{*\pm}$ Meson Production and F_2^c Measurement in Deep Inelastic Scattering (H1)

The charm contribution to the structure function F_2 was analysed with the H1 detector in deep inelastic scattering [20] at virtualities of $1~\text{GeV}^2 < Q^2 < 100~\text{GeV}^2$ and at $0.05 < y < 0.7$. The D^* meson is restricted to the visible region of $p_{T,D^*} > 1.5$ GeV and $|\eta_{D^*}| < 1.5$.

DESY 99-126: Open Beauty Production tagged with Muons (H1)

The semileptonic decay of b-hadrons in muons was used at H1 to reconstruct the $Q\bar{Q}$ system in open beauty production [21]. At least two jets were required, one of which had to contain a muon. The events were selected in photoproduction ($Q^2 < 1~\text{GeV}^2$) with an inelasticity range of $0.1 < y < 0.8$. The muons were required in the central region ($35\,^\circ < \theta^\mu < 130\,^\circ$) with a transverse momentum p_T^μ of at least 2 GeV. The transverse energy of both jets, E_T, had to be above 6 GeV, and the jet cone radius^2 was restricted to $R < 1$. The beauty contribution was determined with the spectrum of the transverse momentum of the muons relative to the jet thrust axis, $p_{T,rel}^\mu$, which is harder for muons originating from b-quarks than from lighter quarks.

DESY 00-166: Open Beauty and Dijet Production Tagged with Electrons (ZEUS)

At ZEUS the semileptonic decay of b-hadrons inside a jet into electrons was used to study open beauty production [22]. As above two jets were required, but in contrast to that measurement no jet was required to contain the electron from the semileptonic decay. The kinematics were restricted to $Q^2 < 1~\text{GeV}^2$, $134 < W_{\gamma p} < 269$ GeV (corresponding to $0.2 < y < 0.8$) and $E_T^{jet\,1(2)} > 7(6)$ GeV. The b-quark was reconstructed from the electron tag by fitting the measured distribution of the electron's transverse momentum relative to the jet axis, $p_{t,rel}$, to summed charm and beauty contributions. The reconstructed quark then had to fulfil $p_{T,b} > 5$ GeV and $|\eta^b| < 2$.

---

^{2}The radius R of the jet cone is defined as $R := \sqrt{(\Delta\eta)^2 + (\Delta\phi)^2}$

4.1.2   Investigation of Dijet Processes

In addition to heavy quark analyses Dijet measurements both in photopro-
duction and deep inelastic scattering are presented.

DESY 97-164: Inclusive Dijet Cross Section in Photoproduction (H1)

An inclusive dijet measurement in photoproduction ($Q^2 < 4$ GeV^2) was made
with the H1 detector [23]. Selection criteria were a jet with transverse energy
of at least $E_T > 6$ GeV and a single cluster[3] in the hadronic calorimeter of
at least 2 GeV. The inelasticity was restricted to $0.2 < y < 0.8$, and the
pseudo-rapidity of the jets was found in the region $-0.5 < \eta_{jet} < 2.5$.

Figure 4.2 show the CASCADE predictions compared to the data.   In
figure 4.2a, which shows the differential cross section as a function of the
logarithmic transverse energy of the jets for $0.4 < x_\gamma < 0.5$, the calculation
is in good agreement with the data.   But figure 4.2b, presenting $d\sigma/dx_\gamma$
for $17.8 < E_T < 22.4$ GeV, again shows that CASCADE overestimates the
contribution of high x_γ.

DESY 97-179: Low Q^2 Jet Production at HERA (H1)

To study parton distributions of the virtual photon at the H1 experiment the
transition between the photoproduction regime and deep inelastic scattering
was investigated [24] at low photon virtualities ($0 < Q^2 < 49$ GeV^2) and
inelasticities of $0.3 < y < 0.6$.   Since three different data samples were
analysed, each of which taken in a different region in Q^2.   The cuts on the
jets in the γp-frame were $E_T^* >$ GeV and $-2.5 < \eta^* < -0.5$.

DESY 97-196: Dijet Cross Section in Photoproduction (ZEUS)

Dijet cross sections were measured at ZEUS [25] in photoproduction for jets
with $E^{T,jet} > 6$GeV, $-1.375 < \eta^{jet} < 1.875$ and a difference in η of maximal
$|\Delta\eta| < 0.5$.

---

[3]see section 1.2.2
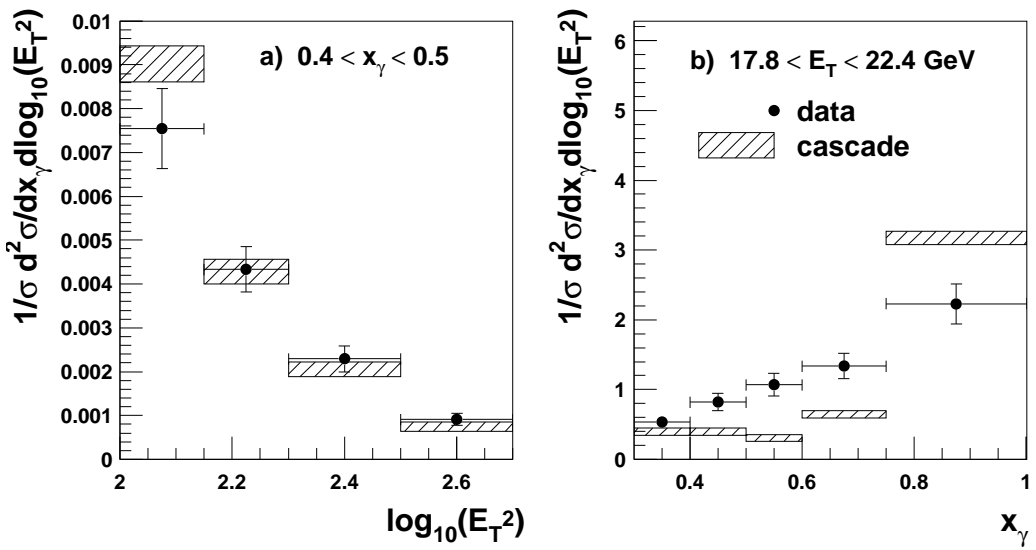
Figure 4.2: *DESY 97-164: The graph in* a *compares* CASCADE *calculations of double differential cross sections as functions of* $\log E_T$ *in a representative bin of* x_γ *to measured data, while* b *shows similar comparisons for differential cross sections of* x_γ *in a representative bin of* $\log E_T$. *Dots represent measured data with total errors, while the boxes show statistical errors of the* CASCADE *calculations. For better comparison the differential distributions are normalised by the total cross section.*
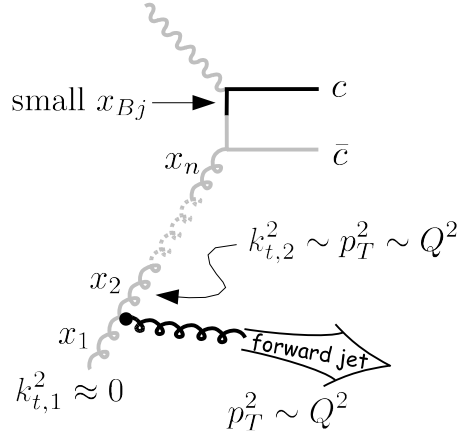
Figure 4.3: *Parton level picture of forward jet production at small x_{Bj}.*

DESY 98-018: High E_T Inclusive Jet Cross Sections in Photoproduction (ZEUS)

The process $e^+p \rightarrow e^+ + \mathrm{jet} + \mathrm{X}$ was studied with the ZEUS detector for pseudo-rapidities in the range $-1 < \eta_{jet} < 2$ and for 134 GeV $< W_{\gamma p} < 277$ GeV. [26] The comparison of the data to Monte Carlo simulations was done for cone radii of $R = 1$ and $R = 0.7$ and four minimal transverse jet energies, $E_T > 14$ GeV, $E_T > 17$ GeV, $E_T > 21$ GeV and $E_T > 25$ GeV. In the original publication the Monte Carlo simulations below 21 GeV and at $R = 1$ did not describe the data properly, whereas cone radii of 0.7 do.

DESY 98-143: Forward Jet and Forward Single Particle Production at small x_{Bj} (H1)

At small x_{Bj} the main contribution to the cross section is BGF, and the parton interacting with the virtual photon faces a hard restriction in longitudinal momentum. Thus the longitudinal momentum of the quarks is too small to form forward jets, so that contributions from forward quark jets are negligible compared to contributions from forward gluon jets (cf. fig. 4.3).

The transverse momentum of these gluon jets is now required to be of the same order of magnitude as the photon virtuality ($p_T^2 \sim Q^2$). Since in the collinear approach (DGLAP) the incoming gluon only carries a negligible

transverse momentum ($k_{t,1}^2 \approx 0$), the emission of a gluon with $p_T^2 \sim Q^2$ causes the propagating gluon to obtain a transverse momentum of the same order of magnitude as the emitted one, $k_{t,2}^2 \sim p_T^2 \sim Q^2$. This leads to a vanishing contribution of DGLAP parton evolution, because a transverse momentum close to the upper scale of the evolution strongly limits the available phase space of the collinear approach, where parton emissions are strongly ordered in transverse momenta.

Since partons in BFKL evolution are not restricted in transverse momentum but strongly ordered in longitudinal momentum fraction ($x_0 \gg x_1 \gg ... \gg x_n$) gluons with high longitudinal momenta occur at the lower end of the evolution ladder with arbitrary transverse momenta and in this way contribute to forward jet production at small x_{Bj}. Effects from CCFM are also expected in this region, because CCFM provides an interpolation between BFKL and DGLAP and at small x_{Bj} should give an approximation to BFKL.

This is why differences in parton evolution models are expected to arise at HERA in forward jet and forward single particle measurements. In the H1 collaboration this was studied in two ways, via measuring forward jet production and forward single particle production, both in deep inelastic scattering [27].

The scattered electron was demanded to have an energy of at least $E_{e'} > 11$ GeV for jet production and $E_{e'} > 12$ GeV for single particle production. The scattering angle with respect to the proton axis had to fulfil $\theta_{min} < \theta_{e'} < 173°$, where $\theta_{min} = 160°$ and $156°$ for jet production and single particle production, respectively. When the mass of the electron is neglected Q^2 can be approximated by $Q^2 = 4E_e E_{e'} cos^2(\theta_{e'}/2)$. The kinematics were thus restricted to the DIS regime. In addition it was demanded that $y > 0.1$.

The jets had to fulfil

$$E_{T,jet} > 3.5 \text{ GeV}$$

$$x_{jet} > 0.035$$

$$7° < \theta_{jet} < 20°$$

$$0.5 < p_{T,jet}^2/Q^2 < 2,$$
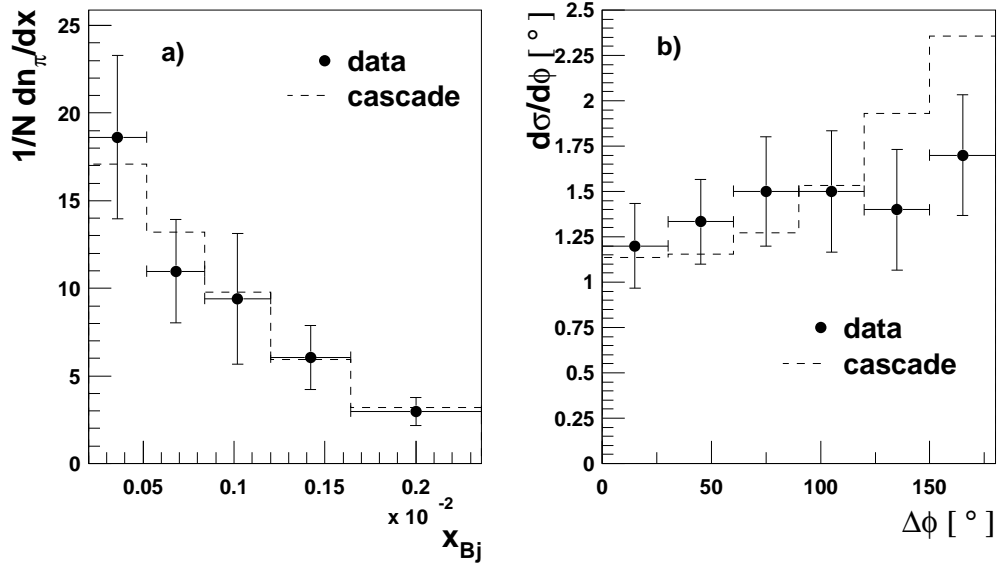
Figure 4.4: *DESY 98143: Differential cross section as a function of the Björken variable x_{Bj} is shown in b). The distribution of the angle $\Delta\phi$ between jet and scattered electron is shown in a).*

where $x_{jet} := E_{jet}/E_p$ is the energy fraction of the jet with respect to the proton energy E_p. The transverse momentum of the jets was taken to be equal to the transverse energy, $p_{T,jet} \equiv E_{T,jet}$.

The single particles (sp), either neutral pions or charged particles all have to fulfil

$$p_{T,sp} > 1 \text{ GeV}$$

$$x_{sp} > 0.01$$

$$5° < \theta_{sp} < 25°.$$

In analogy to the jet case x_{sp} is defined as $x_{sp} := E_{sp}/E_p$, and for neutral pions the transverse momentum is also taken to be equal to the transverse energy.

Figure 4.4 now shows that CASCADE is able to describe the $x_{\text{Björken}}$-distribution well, but the distribution of the opening angle $\Delta\phi$ between jet and scattered electron deviates from the data for large angles.

DESY 98-050: Forward Jet Production at small x_{Bj} (ZEUS)

The validity of the BFKL evolution dynamics at HERA was also studied with the ZEUS detector via forward jet production [28]. The forward jets are selected by

$$
\begin{aligned}
\eta_{jet} &< 2.6 \\
E_{T,jet} &> 5 \text{ GeV} \\
x_{jet} &> 0.036 \\
p_{z,jet}^{Breit} &> 0 \text{ GeV,}
\end{aligned}
$$

where $x_{jet} := p_{z,jet}/E_p$ is the scaled longitudinal momentum fraction of the jets, and $p_{z,jet}^{Breit}$ is the z-component of the jet momentum in the Breit frame. As above the region where BFKL effects are to be expected is restricted by $0.5 < p_{T,jet}^2/Q^2 < 2$ and the cut on x_{jet}, and also the transverse jet momentum is taken to be equal to the transverse jet energy.

These cuts constrain the virtuality of the measurements to about $Q^2 \approx 12$ GeV. In addition the inelasticity is restricted to $y > 0.1$ and the scattered electron is demanded to have at least an energy of $E_{e'} > 10$ GeV.

DESY 00-017: The Q^2 Dependence of Dijet Cross Sections in Photoproduction (ZEUS)

The virtual photon structure was studied with the ZEUS detector via dijets in the virtuality ranges $Q^2 \approx 0$ GeV^2, $0.1 < Q^2 < 0.55$ GeV^2 and $1.5 < Q^2 < 4.5$ GeV^2 [29]. The ratio of the resolved virtual photon contribution to the direct contribution was studied via $d\sigma/dx_\gamma$ in the three different Q^2 regions. Two jets with at least $E_{T,jets} > 5.5$ GeV and a pseudo-rapidity in the range $-1.125 < \eta_{jet} < 2.2$ were demanded, and inelasticity cuts of $0.15 < y < 0.45$ were applied.

DESY 00-035: Dijet Cross Sections and Virtual Photon Structure (H1)

At H1 the resolved structure of the virtual photon was investigated with dijet events at low virtualities ($Q^2 < 0.01$ GeV^2) [30]. Two jets with transverse energy of at least 4 GeV were demanded in the pseudo-rapidity range of $-0.5 < \eta_{jet} < 2.5$ with an invariant jet mass of at least 12 GeV. To enhance the resolution of the jet energy measurement a rather small jet cone radius (R=0.7) reduced the influence of the underlying event energy. The virtual photon was required to carry a fraction y_e of the electron energy in the range $0.5 < y_e < 0.7$. As a result of these cuts x_γ was restricted to $x_\gamma > 0.03$.

In addition gluon densities of the virtual photon have been derived from effective parton densities $f_{\gamma,\text{eff}} = [q(x_\gamma) + \bar{q}(x_\gamma) + 9/4g(x_\gamma)]$ in LO QCD. These have been measured down to $x_\gamma = 0.05$ in a data sample restricted to $E_{T,jet} > 6$ GeV.

DESY 01-120: Measurement of Virtual Photon Structure with Dijets (ZEUS)

Dijet cross sections that are sensitive to the virtual photon structure were measured with the ZEUS detector in photoproduction ($Q^2 < 1$ GeV^2) to constrain the parton distribution functions of the virtual photon [31]. In an inelasticity range $0.2 < y < 0.85$ two jets were required to have $E_{T,jet1} > 14$ GeV and $E_{T,jet2} > 12$ GeV and to be found in the angular region defined by $-1 < \eta_{jet1,2} < 2.4$.

DESY 01-125: Measurement of Dijet Cross Sections (H1)

Dijet event cross sections were measured with the H1 detector in photoproduction in an inelasticity range of $0.1 < y < 0.9$ [32]. The jets with the highest and second highest transverse energy were demanded to have $E_{T,jet1} > 25$ GeV and $E_{T,jet1} > 15$ GeV, respectively. The jets' pseudo-rapidity was restricted to $-0.5 < \eta_{jet1,2} < 2.5$. For its high invariant jet mass of up to 180 GeV and transverse jet energies of up to 80 GeV this measurement took

place in a kinematic region where non-perturbative effects including multiple interactions and hadronisation effects are small and direct comparisons to NLO QCD calculations were possible.

4.2 An Example of the Analysis: Quark Double Tagging with $D^*\mu$-Processes

In [33] and [34] an analysis of events containing a D^* and a muon to tag both charm quarks of the diquark system is presented. In the scope of this thesis the HzTool routine HZ05040[4] has been developed that enables the user to directly compare the results of that measurement to Monte Carlo predictions.

4.2.1 Analysing Charm Production with D^* and Muon

The double tagging analysis uses a D^* particle and a muon to tag both charm quarks produced in boson gluon fusion, either charm or beauty. Tagging, for example, both charm quarks with two D^* particles is not very efficient because, even though the branching ratio $c \to D^*$ is $23.5 \pm 0.7 \pm 0.7\%$, the branching ratio for the 'golden channel' which is used for the reconstruction of D^*s, $D^* \to D^0\pi_s \to K\pi\pi_s$, is only $(2.56 \pm 0.06)\%$. The decay of charm quarks into muons occurs with a significantly higher probability (branching ratio $(9.8\pm0.5)\%$), so that the analysis of events containing a D^* and a muon is more effective than the study of events containing two D^*s.

A non-negligible fraction of $D^*\mu$-events will also originate from beauty quarks decaying into charm quarks which then fragment into a D^*. In this case the muon may originate either from beauty or from charm decay, as illustrated in 4.5. In case I the D^* and the muon originate from the same beauty quark. Here the charges of the D^* and the muon differ, $\Delta Q \neq 0$. Muon and D^* may also originate from different beauty quarks, where the muon may either come directly from the decay of beauty quark (case II),

---

[4]In appendix A a short description of the routine can be found.
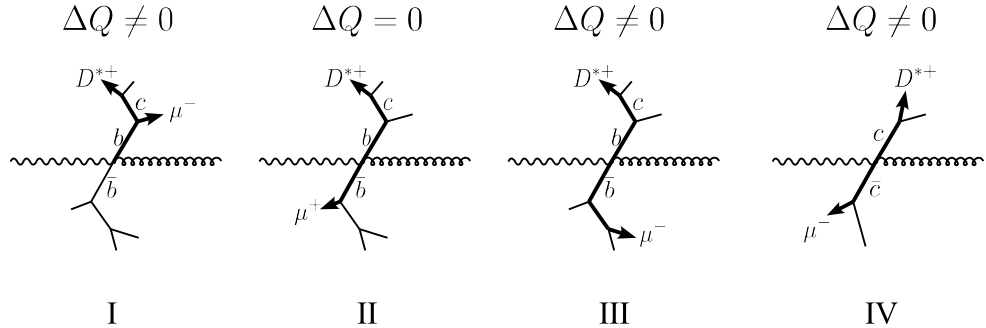
Figure 4.5: *Charge and angle correlations in $D^*\mu$ production*

where the charges are the same, or from the decay of a charm quark (case III), where the charges differ. In case IV the case of charm production is illustrated where the charge of the two particles differ.

In addition to the charge correlations the opening angle also provides an opportunity to distinguish the four cases: when the particles originate from the same quark the opening angle $\Delta\phi$ of the two particles is $\Delta\phi < 90°$, whereas $\Delta\phi > 90°$ when D^* and muon are daughter particles of different quarks of the BGF process.

These angle and charge correlations were used in the thesis to separate charm and beauty contributions and to get a beauty corrected 'quark anti-quark tag' sample where the detected particle are tags for the charm quark and antiquark in BGF.

4.2.2   The HzTool Routine HZ05040

In general HzTool subroutines are divided into three steps:

1. **Initialisation:** histograms are declared with bin sizes matching the bins of the corresponding measurements. Also histograms containing the measured data are declared.

2. **Event Generation:** events are selected by applying cuts matching the cuts of the measurements. After that histograms declared under **1.** are filled.

3. Termination: in the final step histograms are normalised and data histograms are filled with data and errors.

The following cuts defining the visible range of the $D^*\mu$ measurement were applied in the second step during the event generation:

$$p_{T,D^*} > 1.5 \text{ GeV}$$

$$|\eta_{D^*}| < 1,5$$

$$p_\mu > 2 \text{ GeV}$$

$$|\eta_\mu| < 1.735$$

$$0.05 < y < 0.75$$

$$Q^2 < 1\text{GeV}^2$$

All generated events have to fulfil these cuts in order to be selected and to calculate the variables of interest like $p_{t,D^*\mu}$, and to fill the histograms with these values.

$D^*\mu$ **Variables**

The transverse momentum of the diquark system is approximated by the transverse momentum of the $D^*\mu$ system:

$$p_{t,D^*\mu} = \sqrt{(p_{x,D^*} + p_{x,\mu})^2 + (p_{y,D^*} + p_{y,\mu})^2} \ . \tag{4.1}$$

The invariant mass of the diquark system is approximated by $M(D^*\mu)$, the rapidity[5] of the diquark system by

$$\hat{y} = \frac{1}{2}\ln\left(\frac{E(D^*\mu) + p_z(D^*\mu)}{E(D^*\mu) - p_z(D^*\mu)}\right), \tag{4.2}$$

and the opening angle of the quark antiquark pair is approximated by the opening angle $\Delta\phi$ of the $D^*\mu$ pair.

The longitudinal momentum fraction of the gluon, x_g^{obs}, was approximated by [33]:

$$x_g^{obs} = \frac{M(D^*\mu)^2}{sy} \ . \tag{4.3}$$

---

[5]A derivation of the rapidity can be found in [35]

Comparison with Data

In the original thesis CASCADE calculations were done with fragmentation parameters $\epsilon_c = 0.078$ and $\epsilon_b = 0.008$. The results of these calculations were used as a cross check for the HzTool routine, and in figures 4.6 to 4.8 the comparison of the HzTool routine to the original calculation is shown.[6]

It can be seen that the calculations taken from the original thesis are in general in good agreement with the simulation presented here. Good agreement is found in the p_t- and η-distributions of the D^* (fig. 4.6b and d) as well as the beauty corrected $p_{t,D^*\mu}$ (fig. 4.8b). The largest deviations are found in the x_g distribution (fig. 4.8a).

The contribution of beauty quarks is still to be analysed. Up to now there was no indication that this could be responsible for the deviations. Despite this the routine has already been included in the analysis of the gluon phase space of this thesis.

[6]Thanks to Jeannine Wagner for help with the calculations.
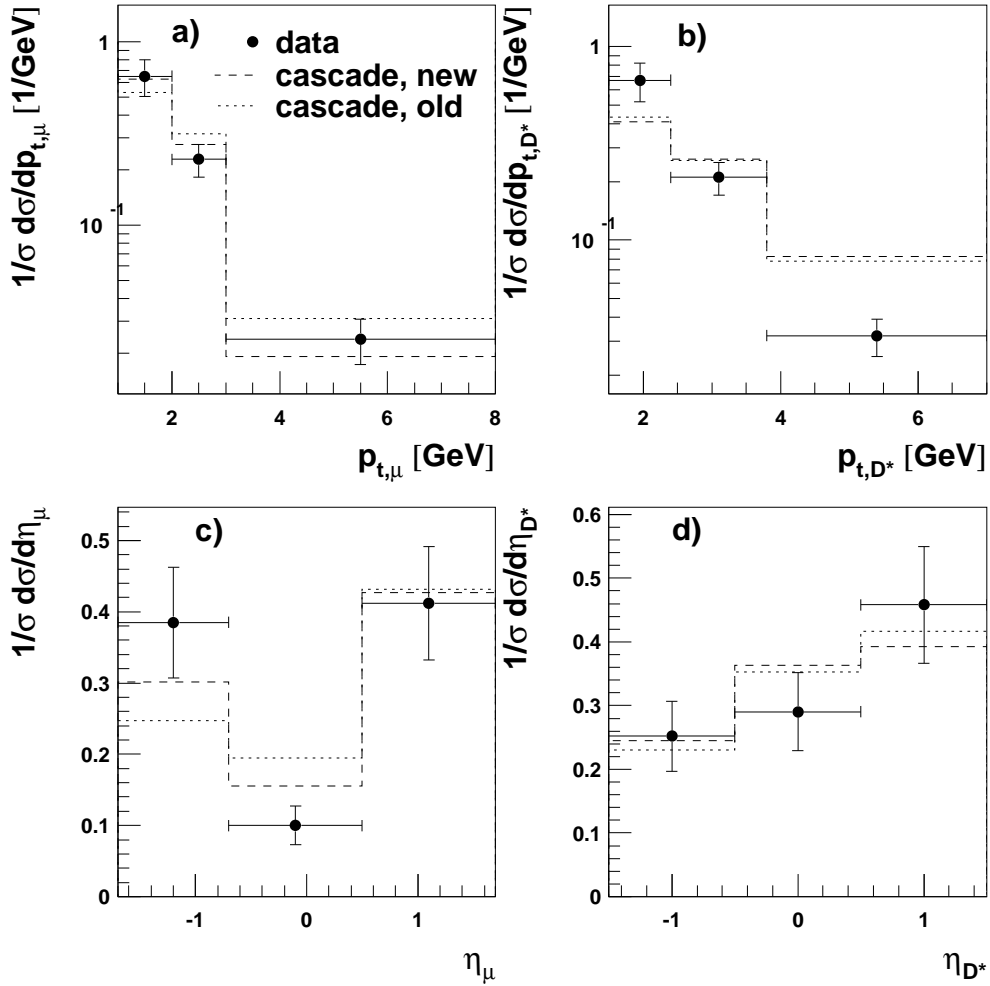
Figure 4.6: *Normalised differential cross sections as functions of a) $p_{t,\mu}$, b) p_{t,D^*}, c) η_μ and d) η_{D^*} are shown for a comparison of* CASCADE *calculations with the* HZTOOL *routine (dashed line, denoted 'new') to data (dots). In addition the* CASCADE *calculations as presented in the original publication are also plotted (dotted line, denoted 'old').*
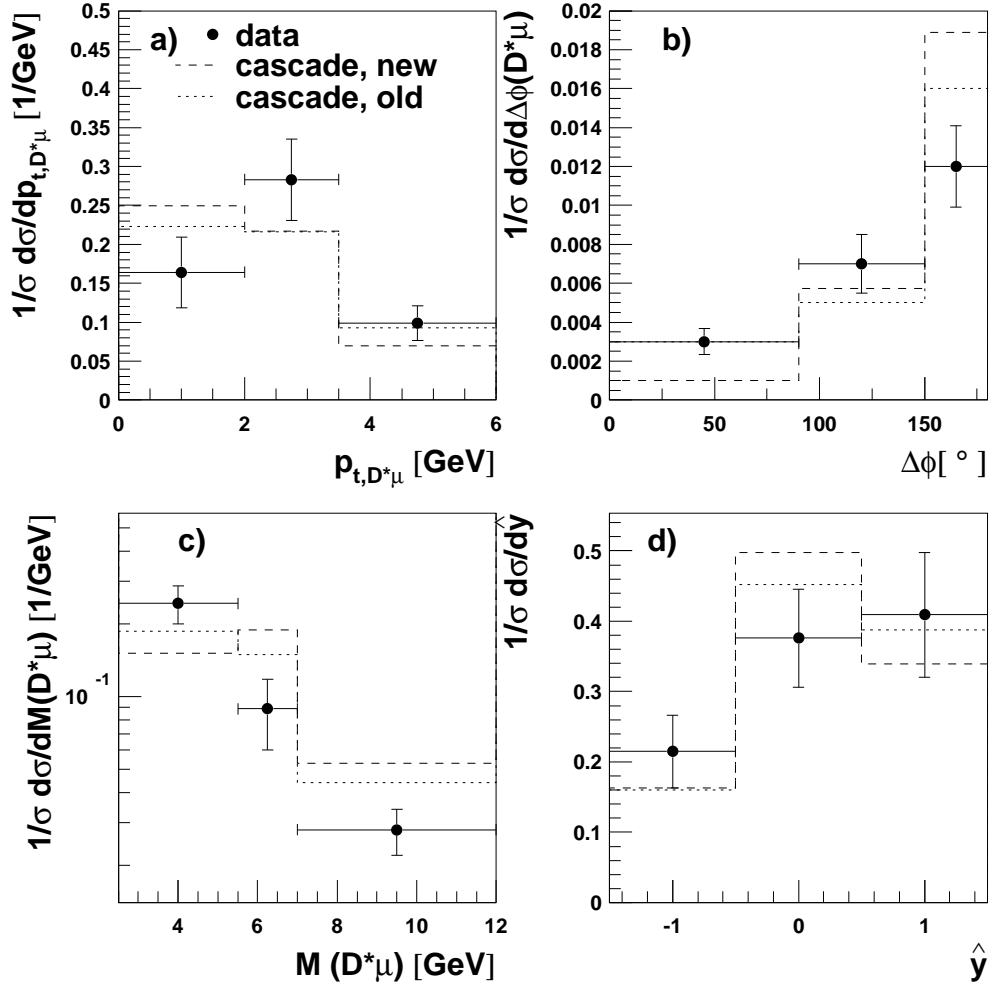
Figure 4.7: *Normalised differential cross sections as functions of a) $p_{t,D^*\mu}$, b) the opening angle of D^* and muon, $\Delta\phi(D^*\mu)$, c) the invariant mass $M(D^*\mu)$ and d) the rapidity $\hat{y}(D^*\mu)$ of the $D^*\mu$ system are shown. A comparison is made between CASCADE calculations with the new HzTool routine (dashed line), measured data (dots) and CASCADE calculations as presented in the original publication are also plotted (dotted line).*
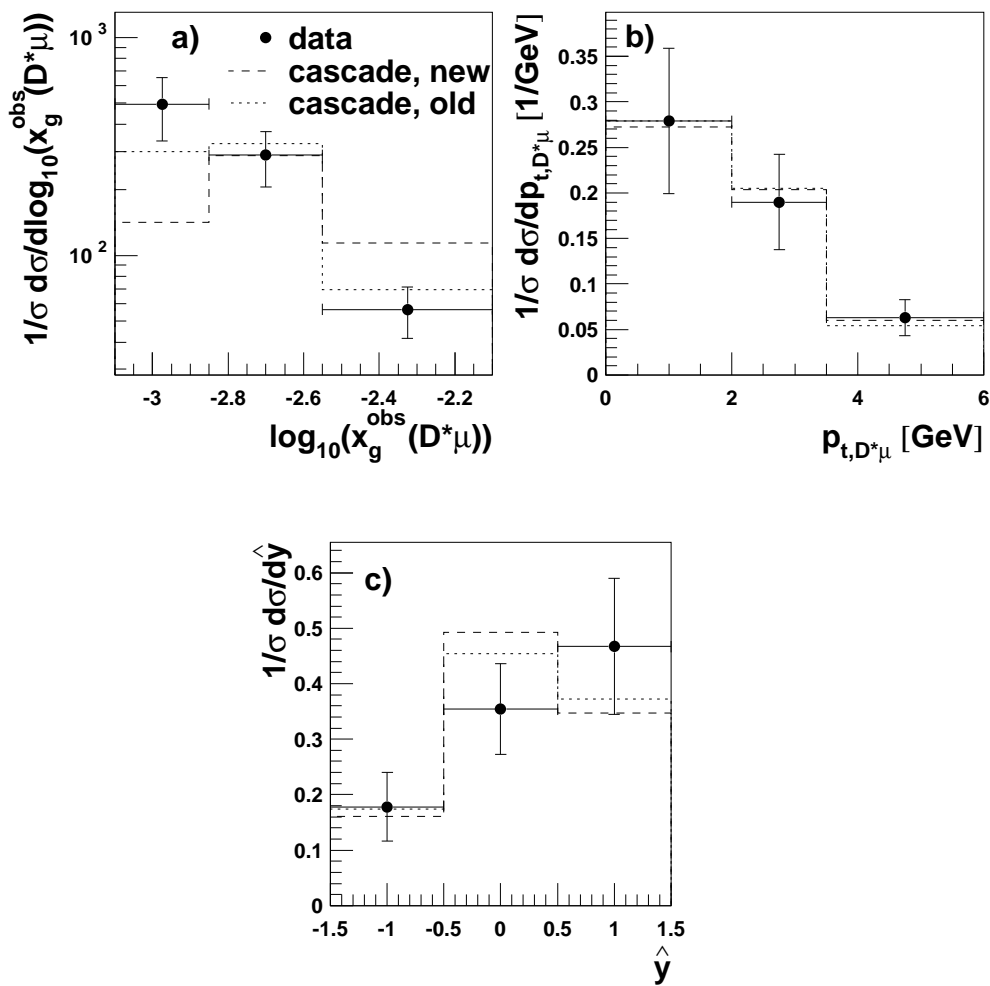
Figure 4.8: *Normalised differential cross sections as a function of a) the longitudinal momentum fraction x_g^{obs}, b) $p_{t,D^*\mu}$ and c) $\hat{y}(D^*\mu)$ are shown for a 'quark antiquark tag' sample.*

4.3   Comparison of Cascade to Rapgap

A short comparison of the calculations of Rapgap to the ones from Cascade is now given. The later analysis of the gluon phase space will be based upon Cascade calculations with same parameters.

In figure 4.9 the predictions of Rapgap and Cascade are compared in calculations for D^* production in DIS of DESY 01-100. The data are shown as dots, Cascade is represented by dashed and Rapgap by dotted lines.

Differential cross sections are shown as functions of a) the hadronic centre of mass energy $W_{\gamma p}$, b) the transverse momentum of the D^*-meson, p_{t,D^*}, c) its pseudo-rapidity η_{D^*} and d) the inelasticity z_{D^*}[7].

The distributions of the hadronic cms energy and the transverse momentum of the D^* are described equally well by Cascade and Rapgap , although Cascade lies closer to the data at low $W_{\gamma p}$. The pseudo-rapidity of the D^*, on the other hand, is described very well by Cascade , whereas Rapgap fails to describe the data properly. The distributions in the Rapgap calculations is shifted to the backward region.

The description of the inelasticity of the D^* is problematic in both generators. Rapgap as well as Cascade show a harder spectrum than the measurement, and only between $z_{D^*} = 0.2$ and 0.4 the calculations match the data roughly.

Using k_t-unintegrated gluon densities therefore enables to describe the measured data as well as and in some cases even better than using integrated gluon densities of the collinear approach. In the next section it will be shown that there are still large differences between the different approaches for uPDFs.

---

[7]The inelasticity is defined by $z_{D^*} := P \cdot p_{D^*} / P \cdot q$, where P, q and p_{D^*} represent the four momenta of the incoming proton, the exchanged photon and the D^*, respectively.
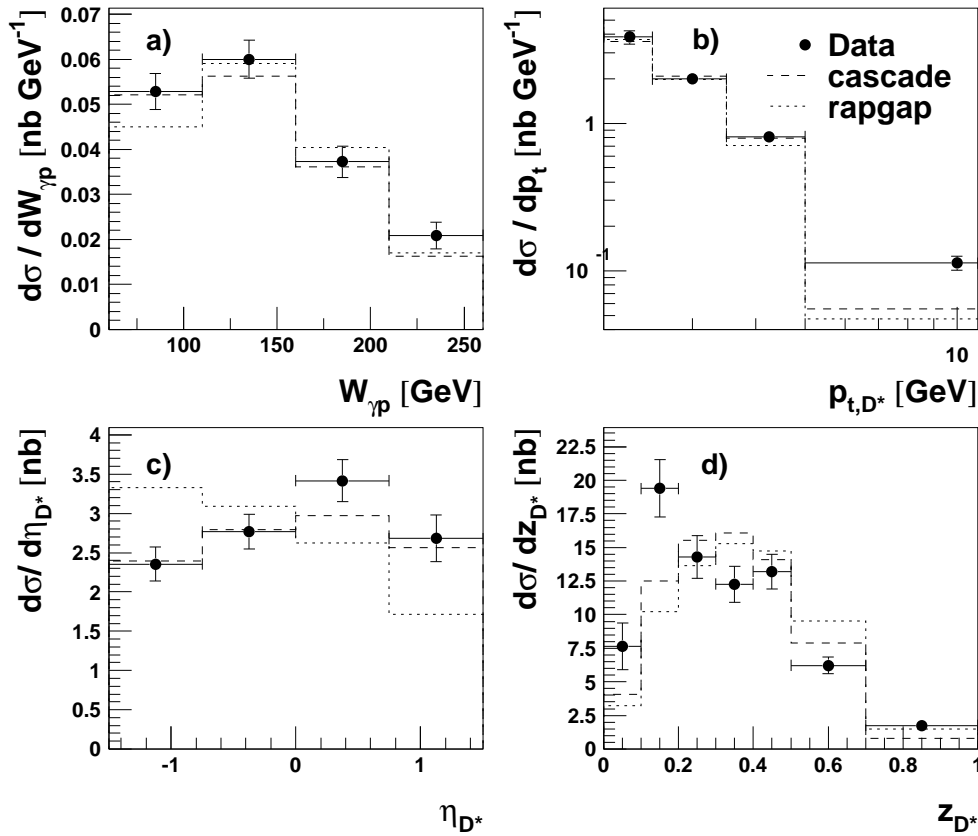
Figure 4.9: *DESY 01-100: Differential cross sections as functions of a) the invariant hadronic centre of mass energy $W_{\gamma p}$, b) the transverse momentum of the D^*-meson, p_{T,D^*}, c) the pseudo-rapidity of the D^*, η_{D^*}, and d) the inelasticity of the D^*, z_{D^*}. Dots represent data points with total errors, while the dashed line shows the CASCADE calculation and the dotted line shows the RAPGAP calculation.*

4.4 Comparison of Different Gluon Densities

Differential cross sections are shown as functions of x_γ (4.10a), p_{t,D^*} (4.10b) and η_{D^*} (4.10c-f). η_{D^*} is plotted in three bin of p_{t,D^*}. The three sets of gluon densities described in section 2.4 are compared: the solid line shows J2003 set 3, which is used in the analysis of the gluon phase space in this thesis. The dashed and the dotted line are set 2 and 1, respectively.

In figure 4.10 the differences between the three gluon densities are clearly visible. All three overestimate the contributions of high x_γ (fig. 4.10a), but set 1 and 3 are in good agreement with the data for p_{t,D^*} (fig. 4.10b). At low p_{t,D^*} set 2 falls below the data. The differential cross sections as a function of η_{D^*} confirm that set 2, which includes non-singular terms in the calculations, fails at describing the data, while set 3 and 1, come close to the data with deviations mainly in the region $\eta_{D^*} \gtrsim 1$.

This comparison shows that different approaches for unintegrated gluon densities can lead to very different results, so that further constraints on the gluon densities from experiment are necessary. One of the goals of this thesis is to show in which regions of phase space existing measurements can be used for these constraints, and where new measurements are needed.
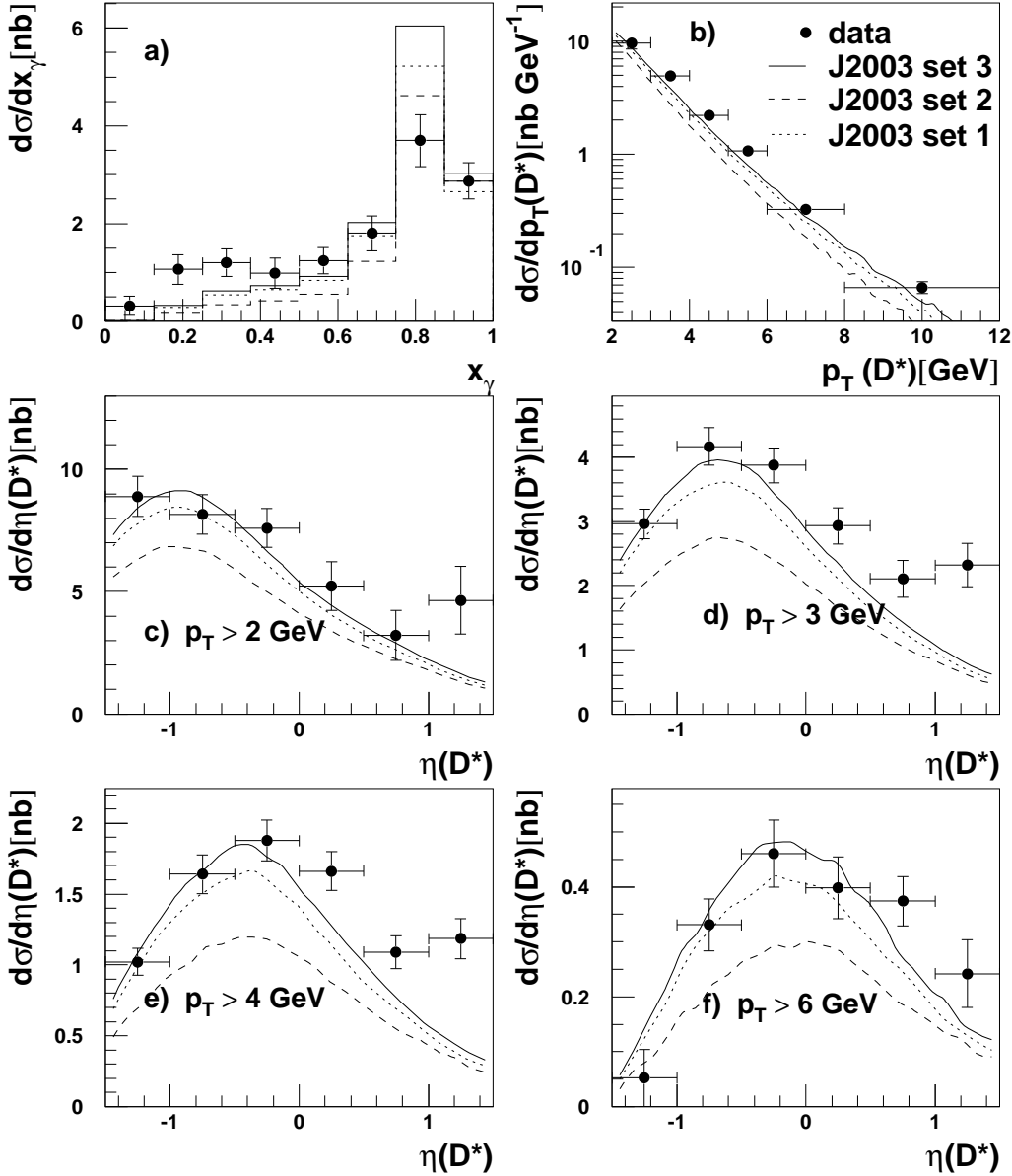
Figure 4.10: *DESY 98-085: differential cross sections as functions of a) x_γ and b) p_{T,D^*}. In c) to f) the cross section is plotted as a function of η_{D^*} for different minimal values of p_{T,D^*}. The solid line represents the gluon density J2003 set 3, the dashed and the dotted line represent set 2 and set 1, respectively.*

Chapter 5

Investigation of the $k_t - x_g-$plane

The transverse momentum and the longitudinal momentum fraction of the hard interacting gluon are now investigated with HzTool and Cascade in the measurements presented in the previous chapter. The aim is to identify the accessible gluon phase space of the measurements, so that they can be used to further constrain unintegrated gluon densities in their specific region of phase space.

Differential cross sections as functions of the transverse momentum and the longitudinal momentum fraction of the gluon are derived on parton level as calculated by the event generators.

5.1   Sensitivity of Observable Quantities

In order to study the gluon phase space it is useful to find observables that are sensitive to the transverse gluon momentum and the longitudinal gluon momentum fraction.

Therefore differential cross sections as functions of k_t and x_g are investigated in bins of observables commonly used in heavy flavour or dijet event measurements. Examples of such observables are the transverse momentum
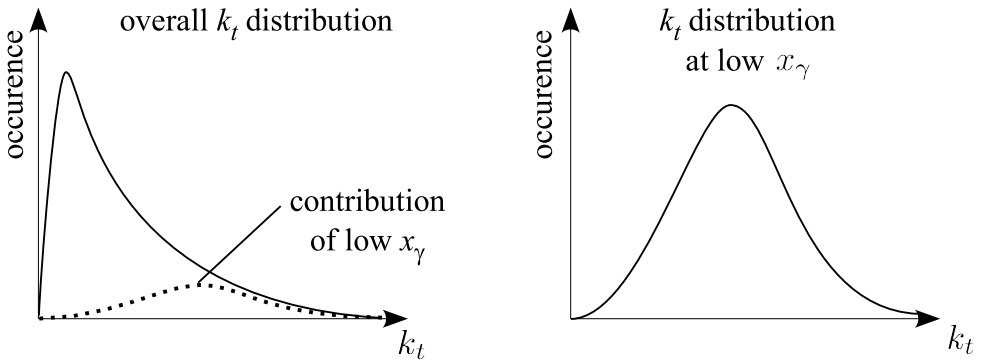
Figure 5.1: *Example of an observable sensitive to k_t. The distribution without a constraint on x_γ peaks at low k_t (sketch on the left). A cut on x_γ brings out the contribution of low x_γ to the cross section (sketch on the right), which shows a harder k_t-spectrum.*

of a D^*-meson, p_{t,D^*}, and the transverse energy of jets, E_T. The idea is to apply cuts on observables and by that restrain the k_t- and x_g-distributions. Figure 5.1 gives an example where a cut of x_γ, as explained already in section 2.8.2, selects events in which the gluon on average carries a higher transverse momentum.

5.1.1   Heavy Quark Production

To reconstruct the properties of heavy quarks produced in boson gluon fusion D^* mesons, muons and are jets are used. Thus the sensitivity of transverse momentum and pseudo rapidity of D^*s and muons are studied first. Afterwards jets are included in the investigations and the sensitivity of x_γ calculated from jet quantities ((2.57)) as well as the transverse jet energy E_T (eq. (2.56)) are studied.

The Transverse Momentum of $D^{*\pm}$ in DIS

Figure 5.2 shows the sensitivity of the transverse momentum p_{t,D^*} as measured in *DESY 01-100*. In three bins of p_{t,D^*} differential cross sections as
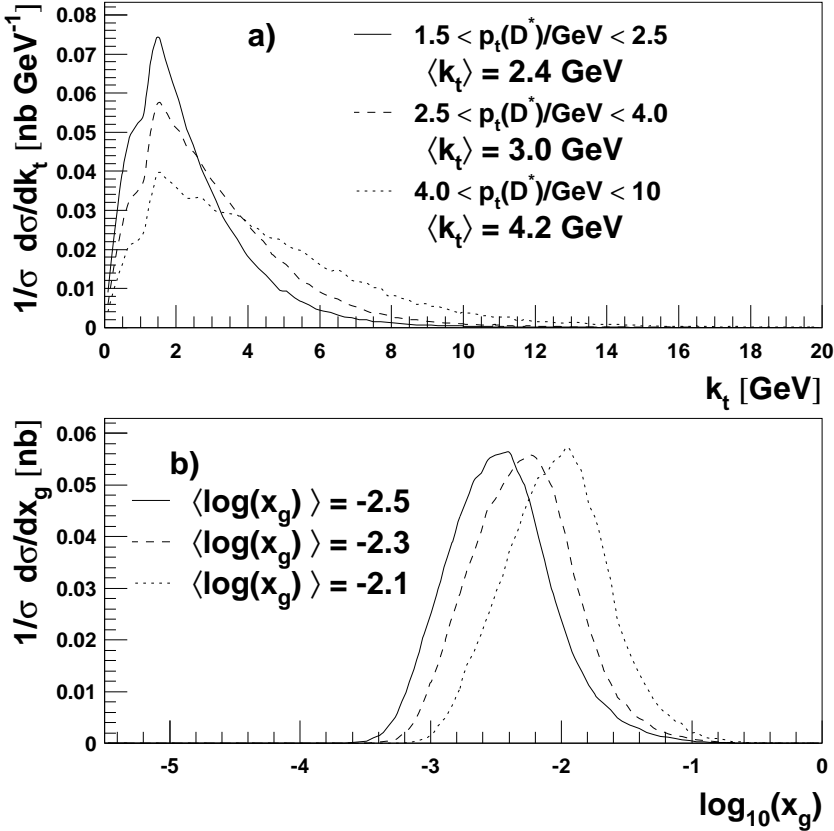
Figure 5.2: *DESY 01-100: In a) differential cross sections as functions of k_t are shown in three different bins of $p_{t,D*}$. Differential cross sections as functions of x_g are shown in b) in the same $p_{t,D*}$-bins as in a). The distributions are obtained by* CASCADE *and normalised to unity for better comparison.*

functions of transverse momentum (a) and the longitudinal momentum fraction of the gluon (b) have been investigated. Figure 5.2 reveals a slight sensitivity of $p_{t,D*}$ to both variables. The mean values of k_t and x_g both rise towards higher $p_{t,D*}$. In figure 5.2a this is due to a harder distribution at higher $p_{t,D*}$, while in figure 5.2d the peak of the distribution shifts.

The sensitivity of $p_{t,D*}$ arises from the relation between $p_{t,D*}$ and the

upper scale for gluon emission in CCFM:

$$\bar{q} = \hat{s} + Q_t^2 \tag{5.1}$$

$$\text{with} \quad Q_t^2 = (p_{t,c} + p_{t,\bar{c}})^2 \,, \tag{5.2}$$

and since p_{t,D^*} serves as an approximation of one of the charm quark's transverse momentum, it indirectly enters the upper scale. Thus larger transverse D^* momenta enhance the phase space available for gluon emission.

A similar statement is true for x_g, since $\bar{q}$ can also be written as (eq. (2.42)):

$$\bar{q} \simeq x_g \sqrt{s \cdot \Xi} \tag{5.3}$$

$$\Rightarrow \quad x_g \sim \bar{q} \sim p_{t,D^*} \,, \tag{5.4}$$

so that larger p_{t,D^*} also lead to larger x_g, which is seen in figure 5.2b.
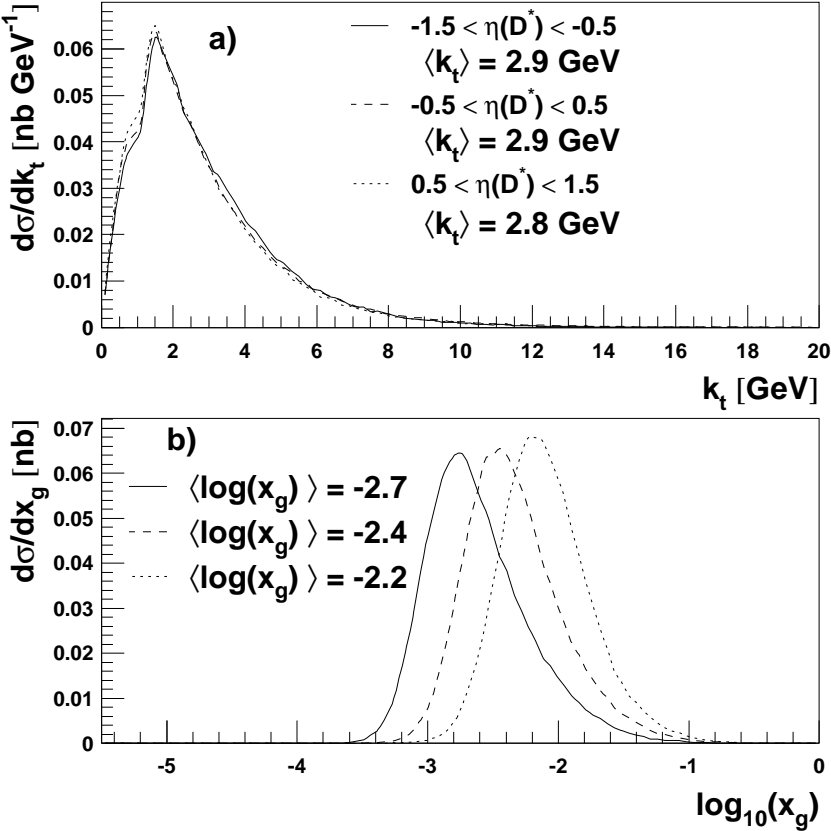
Figure 5.3: *DESY 01-100: In a) differential cross sections as functions of k_t are shown in three different bins of η_{D^*}. Differential cross sections as functions of x_g are shown in b) in the same η_{D^*}-bins as in a). The distributions are normalised to unity for better comparison.*

The Pseudo-Rapidity of $D^{*\pm}$ in DIS

Figure 5.3 shows differential cross sections as functions of k_t (a) and x_g (b) in different bins of η_{D^*}. In fig. 5.3a it can clearly be seen that the pseudo-rapidity η_{D^*} is not sensitive to the transverse momentum of the hard interacting gluon, but (b) shows that a sensitivity of η_{D^*} to x_g is found. The mean value of $\ln x_g$ shifts by half an order of magnitude from -2.7 to -2.2. This is understood by realising that particles of large longitudinal momentum fractions are expected to be found in the forward region.
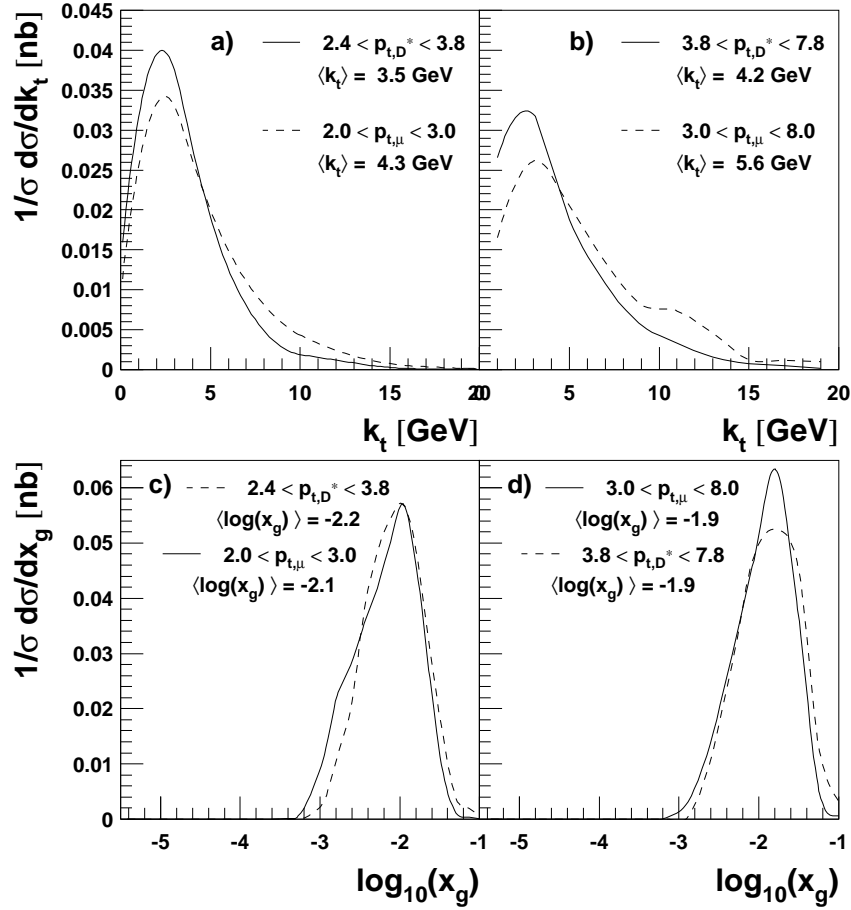
Figure 5.4: *DESY 05-040: Differential cross section as a function of k_t and x_g in bins of $p_{t,\mu}$ and p_{t,D^*}: in a) the k_t-distributions are plotted for the lowest bins of $p_{t,\mu}$ and p_{t,D^*}, while in b) they are plotted in the highest bins each. The graphs in c (d) show the x_g-distribution in bins of $p_{t,\mu}$ (p_{t,D^*}).*

The Transverse Momentum of D^* and Muons in Double Charm Tagging in Photoproduction

In section 4.2 a method was presented to tag both charm quarks of a diquark system by a D^* on one hand and a muon on the other. Ideally the properties of the quarks should be reconstructable from both tags in the same manner. Figure 5.4 now shows a comparison of the sensitivity of the transverse momentum of the D^* and the muon for bins covering roughly the same regions. Differential cross sections as functions of k_t (fig. 5.4a,b) and x_g (fig. 5.4a,b)

are presented.

In figure 5.4a the transverse momentum of the muon is restricted to $2 < p_{t,\mu} < 3$ GeV, while the transverse momentum of the D^* is restricted to $2.4 < p_{t,D^*} < 3.8$ GeV, which is referred to as *low transverse momenta* in the following. At low muon transverse momentum a harder spectrum is observed than at low transverse momentum of the D^*, the mean value of the k_t-distribution $\langle k_t \rangle = 3.5$ GeV in the p_{t,D^*}-bin is slightly below the mean value $\langle k_t \rangle = 4.3$ GeV in the $p_{t,\mu}$-bin.

The same is true for figure 5.4b, where $3 < p_{t,\mu} < 8$ GeV and $3.8 < p_{t,D^*} < 7.8$, referred to as *high tranverse momenta*. The k_t-spectrum in the $p_{t,\mu}$-bin is again harder than the spectrum in the p_{t,D^*}-bin. Also the mean value is different: $\langle k_t \rangle = 5.6$ GeV in the $p_{t,\mu}$-bin and $\langle k_t \rangle = 4.2$ GeV in the p_{t,D^*}-bin.

Comparing the x_g-distributions in bins of p_{t,D^*} and $p_{t,\mu}$ (fig. 5.4c and d) reveals that the differences there are much smaller. The mean values of $\log x_g$ for low transverse momenta of D^* and muon lie close together, $\langle \log x_g \rangle = -2.2$ in the p_{t,D^*}-bin and $\langle \log x_g \rangle = -2.2$ in the $p_{t,\mu}$-bin. For high transverse momenta the mean values are even identical, $\langle \log x_g \rangle = -1.9$ for both the p_{t,D^*}- and the $p_{t,\mu}$-bin. All in all this shows that D^* and muon tagging do not give the same k_t-distribution.

For both muon and D^* tagging the sensitivity of the transverse momentum to k_t is comparable to the sensitivity of p_{t,D^*} in DIS as presented above. The same can be said for the sensitivity of p_{t,D^*} and $p_{t,\mu}$ to the longitudinal momentum fraction of the hard interacting gluon, x_g, when considering that here only two bins of p_{t,D^*} and $p_{t,\mu}$ are analysed instead of three.

The Pseudo-rapidity of D^* and Muons in Double Charm Tagging

Figure 5.5 shows the comparison of the sensitivity of η_μ and η_{D^*} to k_t and x_g represented by differential cross sections in bins of these observables. Figure 5.5b agrees with the previous observation (fig. 5.3) that the pseudo-rapidity of D^* particles is not sensitive to k_t. In contrast to that muons in the central region (dashed line in fig. 5.5a) show a slightly harder k_t spectrum. Here again a difference between D^* and muon tagging becomes visible.
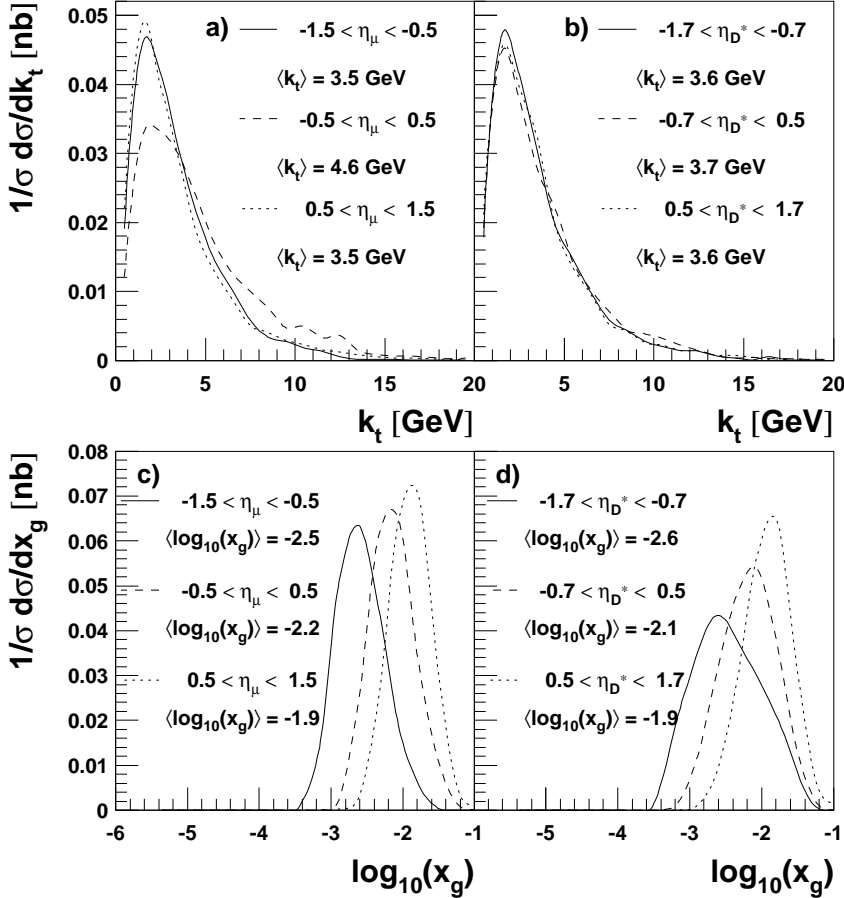
Figure 5.5: *DESY 05-040: Differential cross section as a function of k_t and x_g in bins of η_μ and η_{D^*}: the graphs in a (b) show the k_t-distribution in bins of η_μ (η_{D^*}), the graphs in c (d) show the x_g-distribution in bins of η_μ (η_{D^*}).*

Both η_{D^*} and η_μ show a sensitivity to x_g comparable to the sensitivity of η_{D^*} in DIS (DESY 01-100). The differences between D^* and muon tagging is only found in the k_t-distributions in bins of p_t.

The Transverse Momentum of the D^*-Muon System

The transverse momentum of the D^*-μ system $p_{t,D^*\mu}$ (eq. (4.1)) shows a clearer sensitivity to the gluon transverse momentum than p_{t,D^*} and $p_{t,\mu}$, which can be seen in figure 5.6. In figure 5.6b it is obvious that at $3.5 < p_{t,D^*\mu} < 6$ GeV the differential cross section as a function of k_t has a much
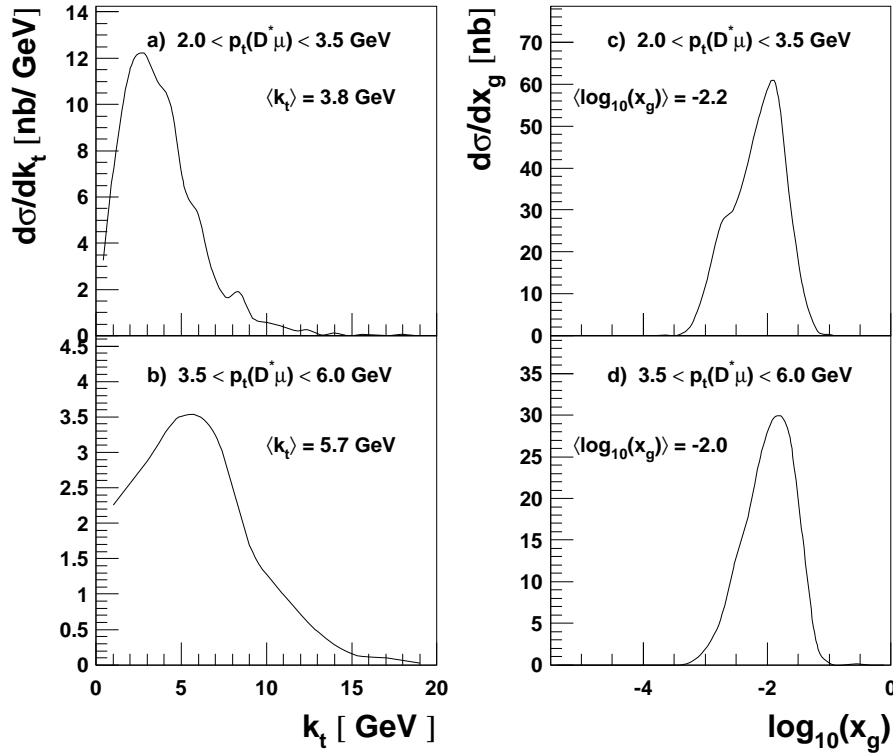
Figure 5.6: *DESY 05040: Cross section as functions of k_t (a-c) and x_g (d-f) are presented in three different bins of $p_{T,D^*\mu}$.*

broader shape than at $2 < p_{t,D^*\mu} < 3.5$ GeV (fig. 5.6a). Also compared to figures 5.4a and b and 5.2a the k_t spectrum at high $p_{t,D^*\mu}$ is significantly harder.

This leads to the conclusion that the transverse momentum of the quark box, which in the double charm tagging method is approximated by $p_{t,D^*\mu}$, gives a quantity that is highly sensitive to the transverse momentum of the hard interacting gluon. This was expected because, as argued in section 2.6, the gluon k_t has to be finite in order to create a quark-antiquark pair that does not cancel in transverse momentum.

In the figures 5.6c and d, on the other hand, $p_{t,D^*\mu}$ shows no sensitivity to the longitudinal gluon momentum fraction.
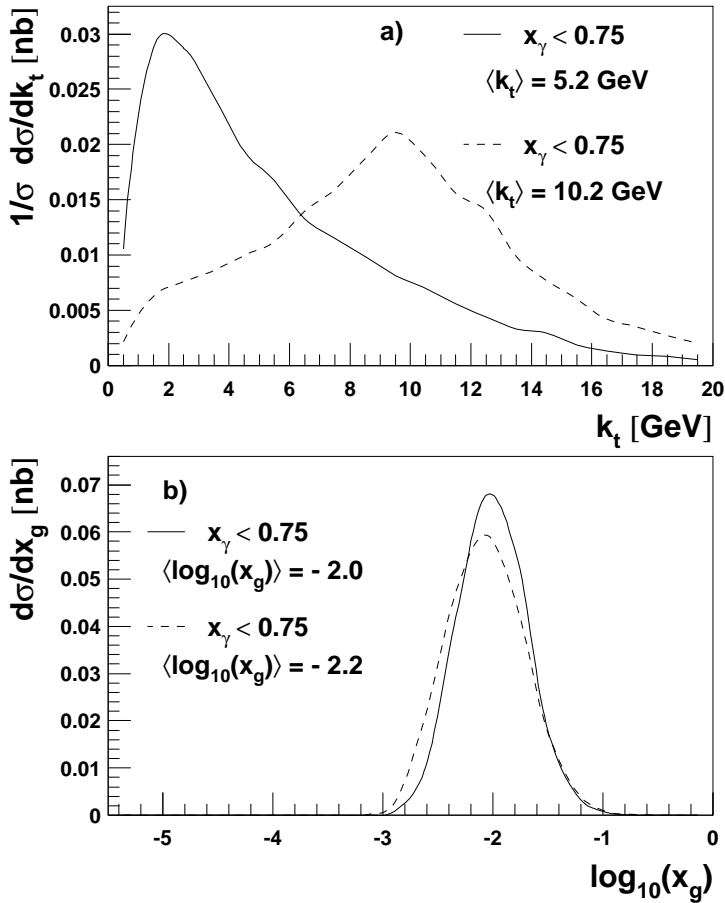
Figure 5.7: *DESY 98-085: Normalised inclusive $D^{*\pm}$ and associated dijet [18] cross section as a function of k_t and x_g in different regions of x_γ on generator level: in a) $x_\gamma < 0.75$, in b) $x_\gamma > 0.75$*

x_γ in Charm Photoproduction

If dijets are used in combination with charm production, the fraction x_γ of the photon momentum that enters the hard interaction can be used to become sensitive to different regions in k_t. In section 2.8.2 the motivation behind this was already explained. Figure 5.7a confirms the expectation that x_γ is sensitive to k_t: the solid line represents the differential cross section as a function of k_t for $x_\gamma < 0.75$, and the dashed line represents the same distribution for $x_\gamma > 0.75$. It can be seen that high x_γ are sensitive to low k_t
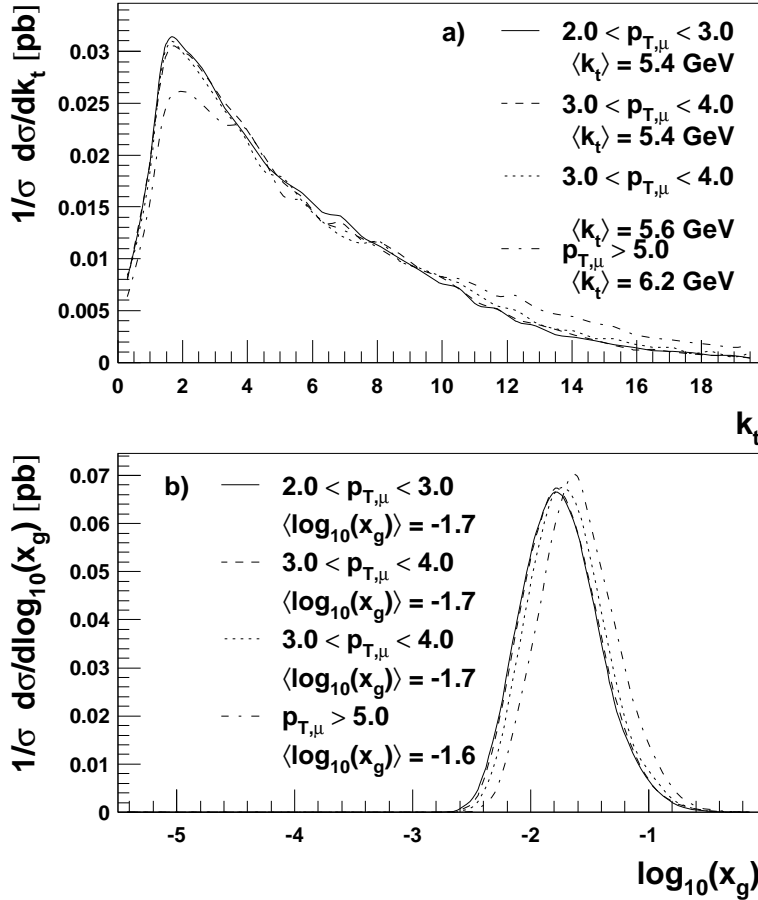
Figure 5.8: *DESY 99-126: Differential cross sections as functions of k_t (a) and x_g (b) in different bins of $p_{t,\mu}$, indicated by different line styles. The mean values are given for each distribution.*

($\langle k_t \rangle = 5.2$ GeV), and low x_γ are sensitive to high k_t ($\langle k_t \rangle = 10.2$ GeV), as expected from section 2.8.2.

Transverse Momentum of Muons in Beauty Production

Figure 5.8 shows differential cross sections as functions of k_t (a) and x_g (b) in different bins of the transverse momentum of muons from beauty decay as measured in DESY 99-126. The figure illustrates that $p_{t,\mu}$ is neither sensitive to k_t nor to x_g.

5.1.2 x_γ and E_T in Dijet Events

The momentum fraction x_γ of the diquark system may also be studied in inclusive diquark events that are not restricted to heavy quarks. At low x_γ different mean transverse energies of the jets can be used to become sensitive to different regions of high k_t.

Dijets at Low Q^2

For DIS at low Q^2 (< 80 GeV^2) this is shown in figures 5.9e to h, where the cross section as a function of k_t in two bins of x_γ is represented by the solid ($0.15 < x_\gamma < 0.6$) and the dashed ($0.6 < x_\gamma < 0.75$) line. For both x_γ-bins the mean k_t rises with increasing E_T. The k_t-region covered here ranges from about $\langle k_t \rangle = 4$ GeV (fig. 5.9e) to about $\langle k_t \rangle = 13$ GeV (fig. 5.9h). The transverse energy of jets therefore presents an opportunity to choose the k_t-region to study. It is also interesting to note that the difference between the distributions of the two bins becomes smaller at high transverse jet energies.

At $x_\gamma > 0.75$ the mean transverse momentum of the hard interacting gluon increases from about $\langle k_t \rangle = 3$ GeV at $30 < \bar{E}_T^2 < 45$ GeV^2 to about $\langle k_t \rangle = 5$ GeV at $45 < \bar{E}_T^2 < 65$ GeV^2. Thus the conclusion that the sensitivity to high k_t increases at high $\bar{E}_T$ remains true for $x_\gamma > 0.75$.

Figure 5.10 now shows differential cross sections as functions of x_g. As can be seen there the sensitivity of E_T^{jet} shown in figure 5.10 is not as pronounced, but still the mean value $\langle \log x_g \rangle$ increases from $\langle x_g \rangle = -2.2$ in the lowest bin to $\langle \log x_g \rangle = -1.6$ in the highest bin. If the width of distribution is taken into account, the measurement becomes sensitive to roughly one order of magnitude in x_g by changing the transverse energy of jets.

Dijets in Photoproduction

In figures 5.11 the same sensitivity of x_γ to k_t can be observed. Again, differential cross sections as functions of k_t are shown for $x_\gamma < 0.75$ in figures 5.11a to d, and for $x_\gamma > 0.75$ in figures 5.12e to h (the dashed lines only

serve for better illustration). Figures 5.11a to d show that large k_t become accessible with increasing transverse energy at low x_γ (up to $k_t \sim 20$ GeV for $10.0 < E_T < 20.0$ GeV).

Differential cross sections as a function of x_g are shown in figure 5.12. The graphs confirm that with increasing transverse jet energies higher longitudinal momentum fractions, here up to $\log x_g \approx -1$, become available, which was already shown for dijet events in DIS at low Q^2 (fig. 5.10).
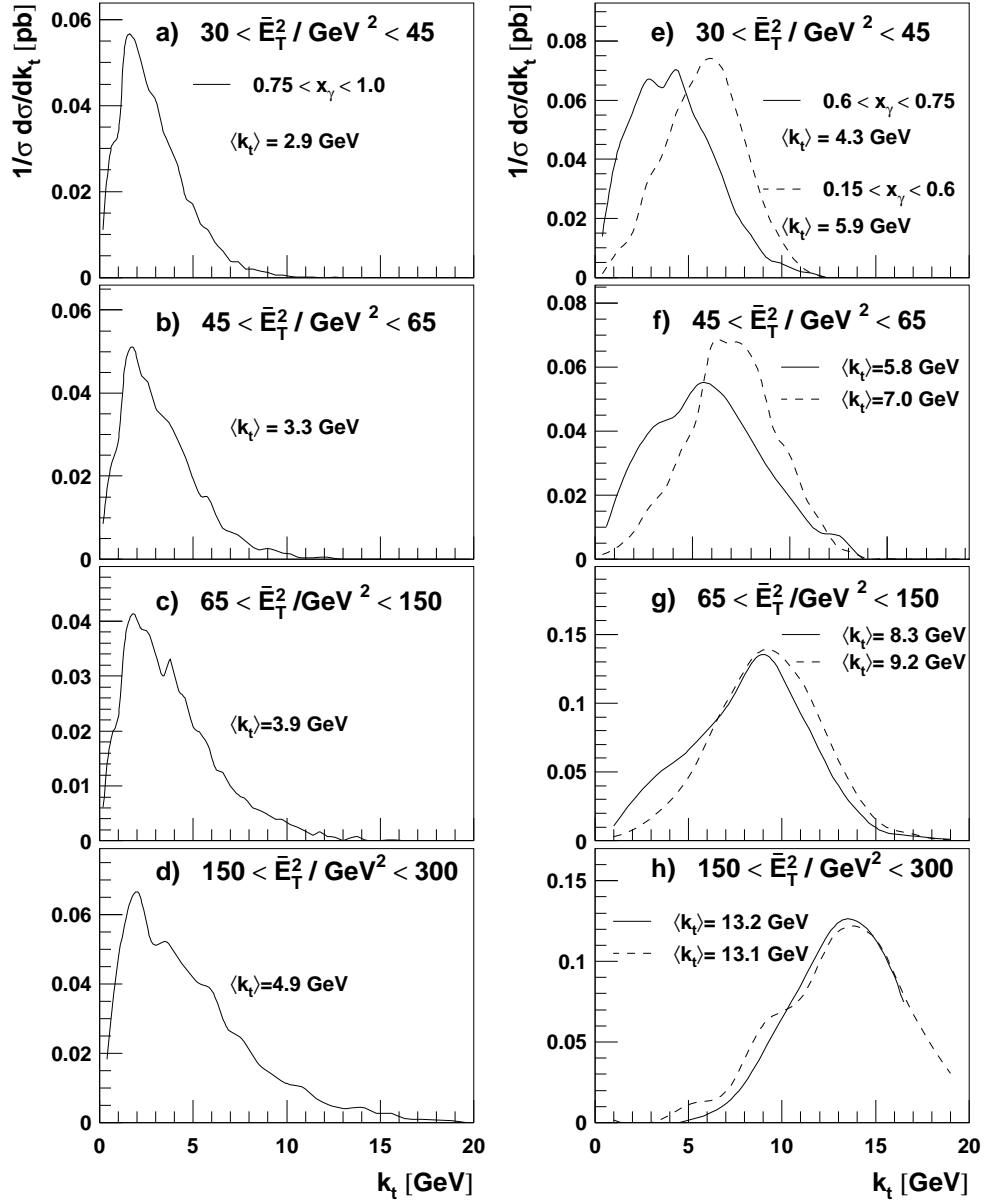
Figure 5.9: *DESY 98205: Normalised dijet cross section at low Q^2 as a function of k_t in bins of x_γ and the mean transverse energy of the jets, $\bar{E}_T$. Plots* a *to* d *are at high x_γ with $\bar{E}_T$ rising from* a *to* d*. Plots* e *to* f *are at low x_γ with $\bar{E}_T$ rising from* e *to* f*, where the solid line represents $0.15 < x_\gamma < 0.6$, and the dashed line $0.6 < x_\gamma < 0.75$*
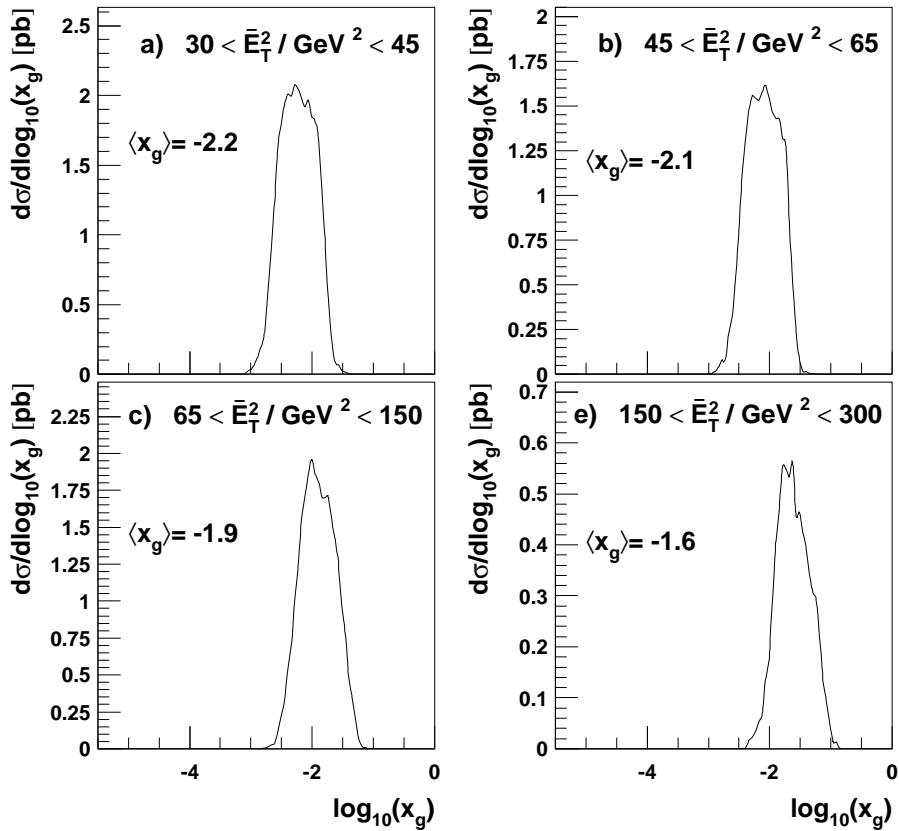
Figure 5.10: *DESY 98-205: Differential cross sections as functions of x_g in different bins of the transverse energy of jets. The mean values $\langle x_g \rangle$ of the distributions are also given.*
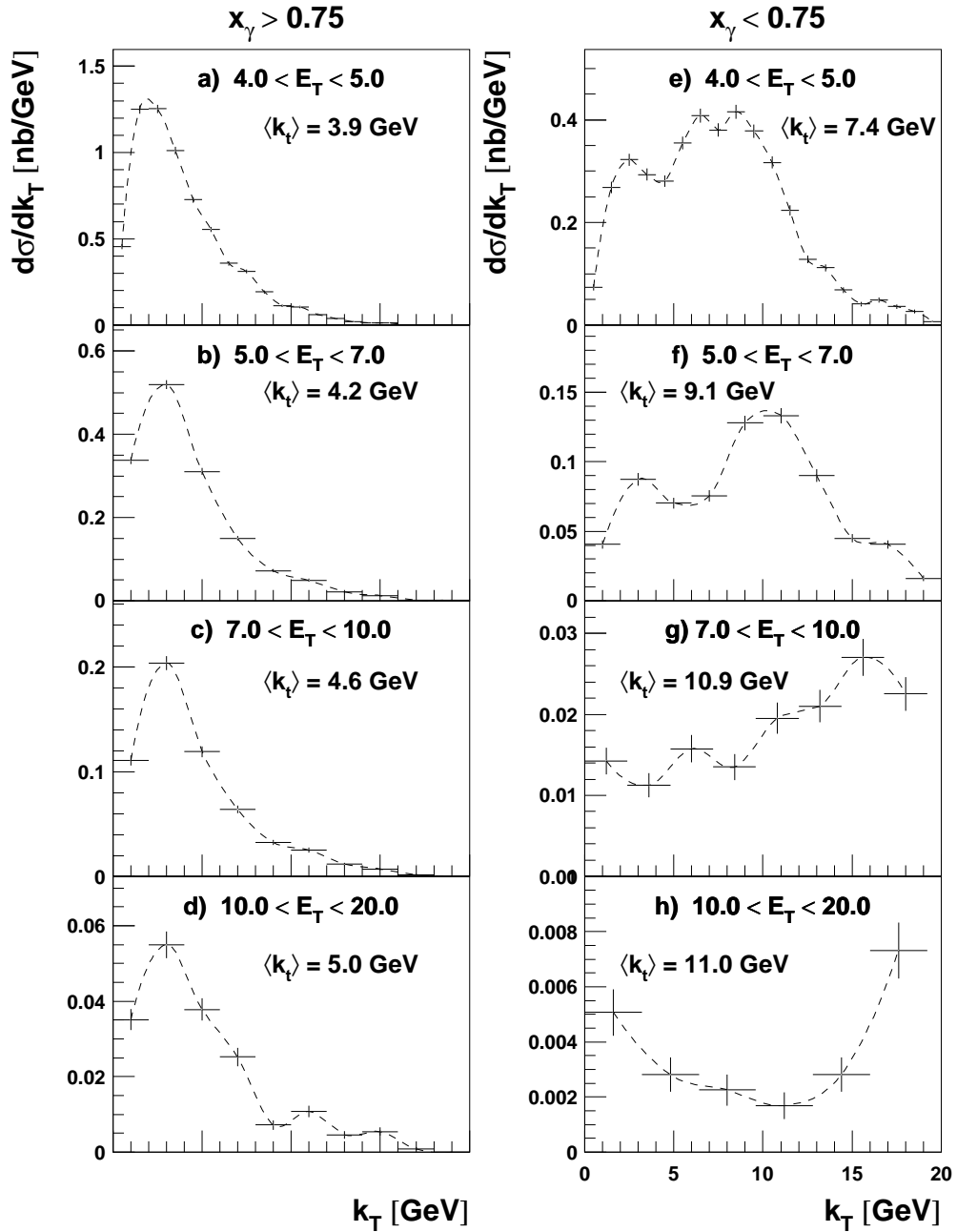
Figure 5.11: *DESY 97-196: Differential cross sections as functions of k_t in four different bins of E_T. The distributions are shown at $x_\gamma > 0.75$ (a-d) and at $x_\gamma > 0.75$ (e-h). The dashed lines serve for better illustration.*
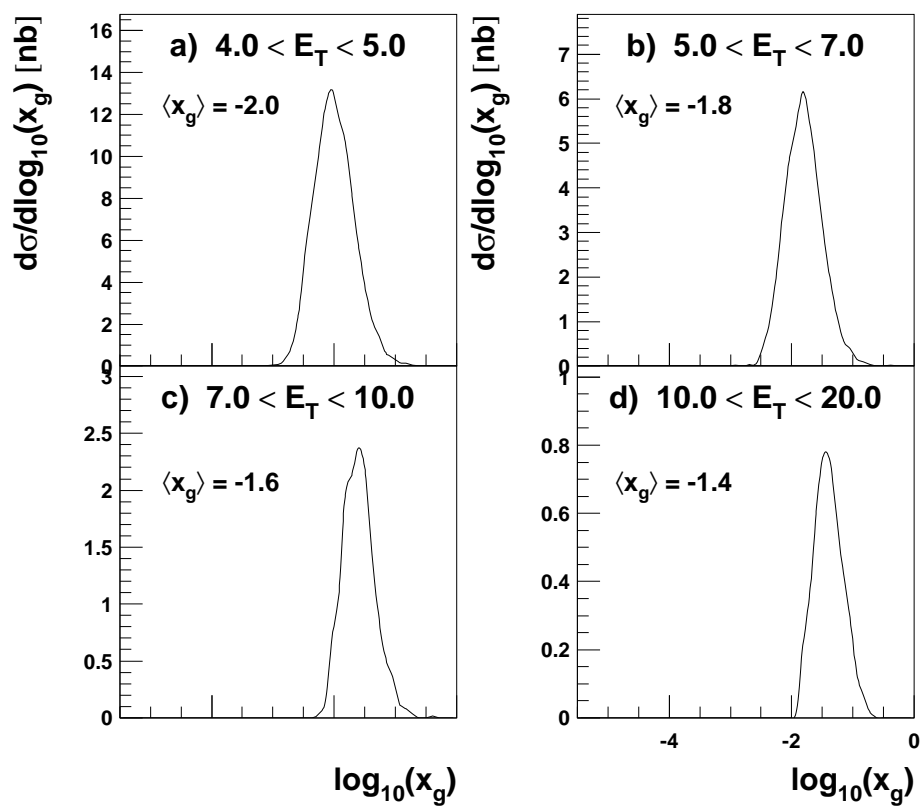
Figure 5.12: *DESY 97-196: Differential cross sections as functions of x_g in four different bins of E_T.*
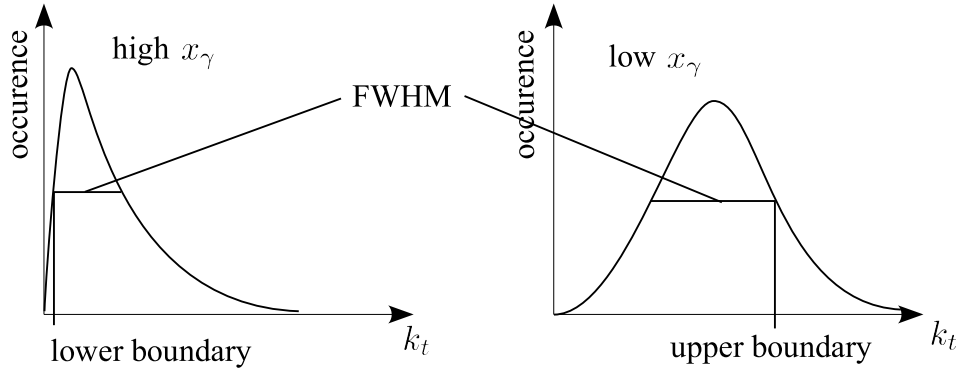
Figure 5.13: *Illustration of the method to obtain the accessible gluon phase space of the investigated measurements.*

5.2   Mapping of Gluon Phase Space

A 'map of the phase space' of hard interacting gluons is rendered to display the accessible gluon phase space of the measurements presented in chapter 4.

The accessible phase space of a measurement is indicated by the mean values $\langle k_t \rangle$ and $\langle \log x_g \rangle$ of the total distributions. The boundaries of the accessible phase space are obtained by varying the quantities investigated in the previous section (x_γ, p_{t,D^*}, etc.) and studying the k_t- and x_g-distributions.

Figure 5.13 illustrates this in an example where x_γ is used to study k_t. There the lower boundary of the accessible phase space is obtained from the high x_γ-bin, while the upper boundary is obtained from the low x_γ-bin. The mean value, on the other hand, is always the mean value of the total distribution, namely the sum of all distributions.

Figures 5.14 and 5.15 show the accessible k_t- and x_g- regions of the measurements presented in section 4.1. The curves show the three sets of gluon densities presented in section 2.4 as a function of k_t for $\log x_g = -2$ and serves merely as an illustration of the studied gluon densities. The dots represent the mean values $\langle k_t \rangle$ and $\langle x_g \rangle$ respectively, while the horizontal error bars indicate the accessible phase space.

It can be seen in figure 5.14 that the inclusion of jets enhances the avail-
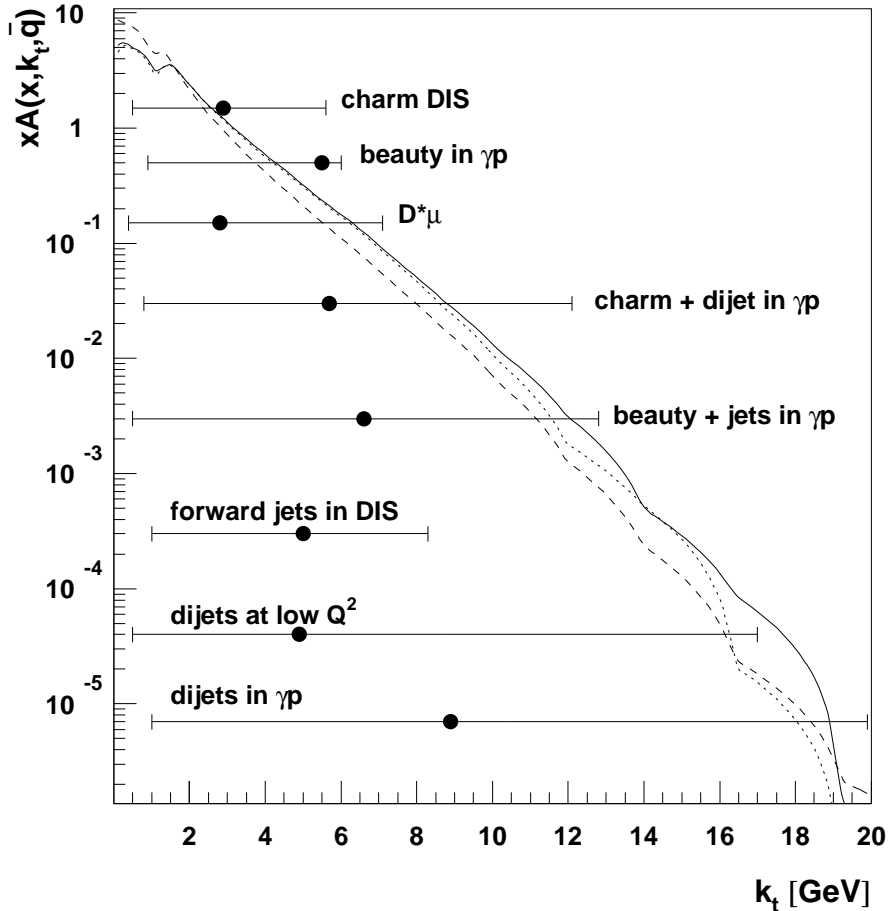
Figure 5.14: *Available regions of the gluon transverse momentum of previous HERA measurements. The three unintegrated gluon densities presented in section 2.4 are shown as a function of k_t. The dots mark the mean values $\langle k_t \rangle$ while the error bars mark the accessible k_t-region.*

able k_t-region in charm as well as in beauty production. Heavy quark measurements mostly cover the region of low k_t, while dijet measurements stretch over a wide range in k_t up to values of $k_t = 20$ GeV.

Figure 5.15 presents the regions of x_g accessible to the investigated measurements. There it can be seen that measurements in DIS can access lower x_g in comparison to measurements in photoproduction.
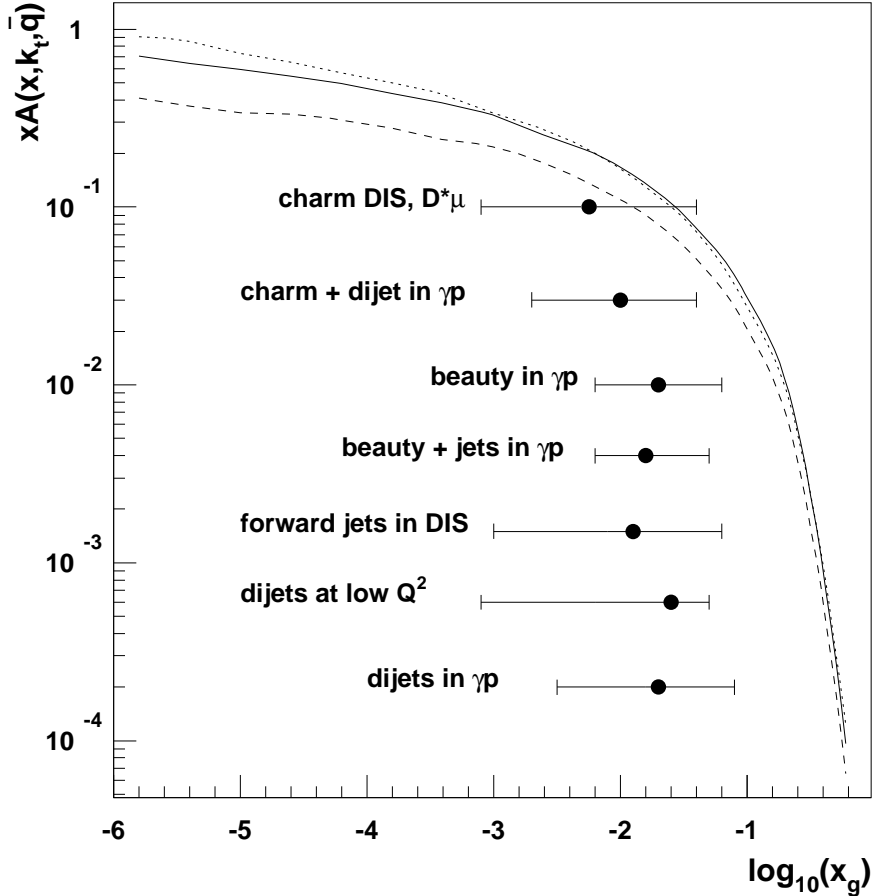
Figure 5.15: *Available regions of the longitudinal gluon momentum fraction of previous HERA measurements. The three unintegrated gluon densities presented in section 2.4 are shown as a function of $\log x_g$. The dots mark the mean values $\langle \log x_g \rangle$ while the error bars mark the accessible regions in x_g.*

It is also interesting to note that measurements of beauty quarks face a restriction to rather high x_g because the mass $2 \cdot m_b \approx 10$ GeV to be produced by the photon and the gluon puts a lower threshold 'on the longitudinal momentum fraction of the gluon. Charm measurements, on the other hand, cover a wider region in longitudinal momentum but are also restricted in the region of high transverse momentum. There dijet measurements provide an opportunity for more detailed analysis.
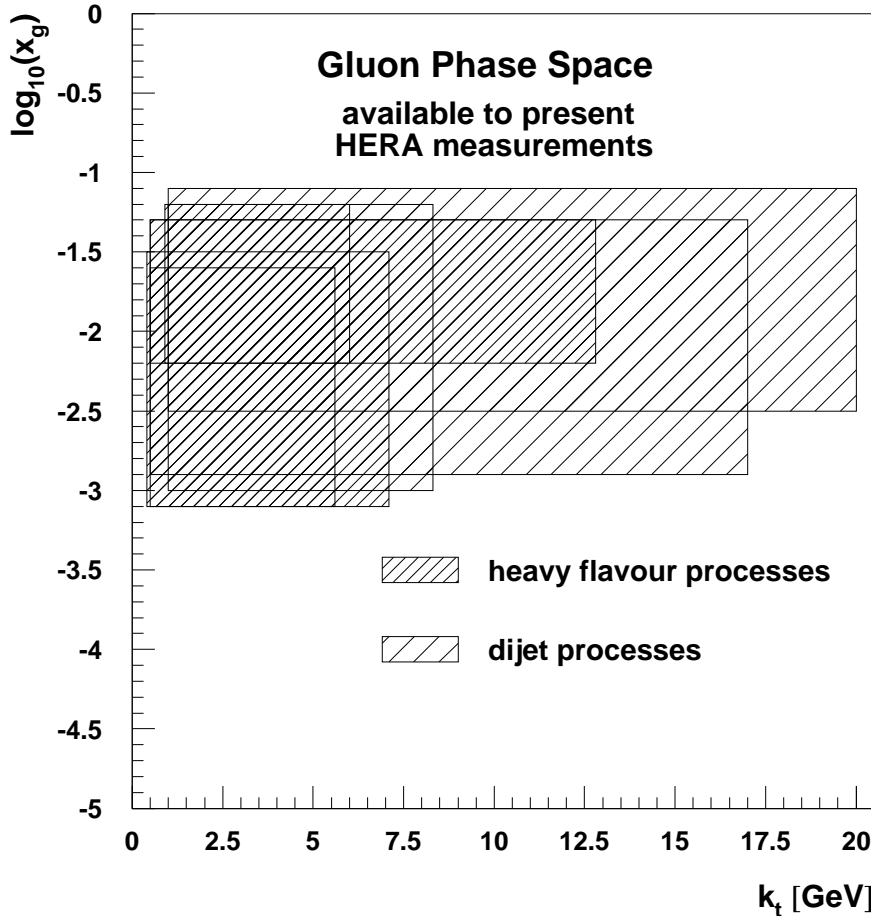
Figure 5.16: *Gluon phase space available to present heavy flavour and dijet measurements at HERA. The boxes indicate the individual measurements.*

In figure 5.16 the accessible x_g-regions are now plotted against the accessible k_t-regions to display the phase space accessible by present HERA measurements. The area with the lighter hatch represents the phase space of the gluon in dijet measurements while the darker hatch represents the gluon phase space in heavy flavour production.

5.3   Dedicated Measurement of Unintegrated Gluon Densities

In figure 5.16 it is interesting to note the regions of phase space which have not been made available yet. As can also be seen from figure 5.15 the region of $x_g < 10^{-3}$ is not even available to forward jets studied at HERA.

The region of $x_g > 0.1$ is especially interesting because none of the investigated measurements covers this. Dedicated heavy flavour measurements would provide an opportunity to study gluon densities in this region because the main production mechanism is boson gluon fusion even at high x_g. In combination with jets regions of high k_t at high x_g would also become available.

Since up to now gluon densities are the main focus in current research of k_t-factorisation, such a measurement would be a profitable and natural continuation of this thesis.

Chapter 6

Conclusions

In this thesis it has been emphasised that for a deeper understanding of un-integrated gluon densities further constraints from experiment are needed. A map of the gluon phase space accessible to HERA measurements has been presented, which also indicates the regions of phase space where new measurements are desirable. The measurements presented here can be used to constrain the uPDFs in their particular region of phase space. Furthermore it has been shown that the observables x_γ and E_T^{jet} are both sensitive to the transverse momentum of the gluon.

Measurements of Heavy quark production are suited to determine uninte-grated gluon densities at $x_g \gtrsim 0.1$ from experiment. In addition a combination of heavy flavours and dijets gives the opportunity to use x_γ and E_T to access a large region in transverse momentum.

Bibliography

[1] Halzen, F. and Martin, Alan D., *QUARKS AND LEPTONS: AN INTRODUCTORY COURSE IN MODERN PARTICLE PHYSICS*. New York, Usa: Wiley (1984) 396p.

[2] Ellis, R. K. and Stirling, W. James and Webber, B. R., *QCD and collider physics*, Vol. 8. 1996.

[3] Devenish, R. and Cooper-Sarkar, A., *Deep inelastic scattering*. Oxford, UK: Univ. Pr. (2004) 403 p.

[4] Catani, S. and Ciafaloni, M. and Hautmann, F., Nucl. Phys. **B366**, 135 (1991).

[5] Kuraev, E. A. and Lipatov, L. N. and Fadin, Victor S., Sov. Phys. JETP **44**, 443 (1976).

[6] Kuraev, E. A. and Lipatov, L. N. and Fadin, Victor S., Sov. Phys. JETP **45**, 199 (1977).

[7] Balitsky, I. I. and Lipatov, L. N., Sov. J. Nucl. Phys. **28**, 822 (1978).

[8] Fadin, Victor S. and Lipatov, L. N., Phys. Lett. **B429**, 127 (1998).

[9] Ciafaloni, Marcello and Camici, Gianni, Phys. Lett. **B430**, 349 (1998).

[10] Andersson, Bo and others, Eur. Phys. J. **C25**, 77 (2002).

[11] Jung, Hannes, Mod. Phys. Lett. **A19**, 1 (2004).

[12] Hansson, M. and Jung, H. (2003).

[13] Martí Magro, Lluís, Investigation of Heavy Quark and Multiple Interactions at HERA, Diplomarbeit (2005).

[14] Ellis, Stephen D. and Soper, Davison E., Phys. Rev. **D48**, 3160 (1993).

[15] Jung, Hannes, *The* Rapgap *Monte Carlo for Deep Inelastic Scattering, Version 3.1.* Available at http://www.desy.de/%7Ejung/rapgap/ rapgap31021.ps.gz, 2005.

[16] Collins, John and Jung, Hannes (2005).

[17] Corradi, M., *Benchmark Cross-seection Manual.* 2005.

[18] Breitweg, J. and others, Eur. Phys. J. **C6**, 67 (1999).

[19] Breitweg, J. and others, Eur. Phys. J. **C12**, 35 (2000).

[20] Adloff, C. and others, Phys. Lett. **B528**, 199 (2002).

[21] Adloff, C. and others, Phys. Lett. **B467**, 156 (1999).

[22] Breitweg, J. and others, Eur. Phys. J. **C18**, 625 (2001).

[23] Adloff, C. and others, Eur. Phys. J. **C1**, 97 (1998).

[24] Adloff, C. and others, Phys. Lett. **B415**, 418 (1997).

[25] Breitweg, J. and others, Eur. Phys. J. **C1**, 109 (1998).

[26] Breitweg, J. and others, Eur. Phys. J. **C4**, 591 (1998).

[27] Adloff, C. and others, Nucl. Phys. **B538**, 3 (1999).

[28] Breitweg, J. and others, Eur. Phys. J. **C6**, 239 (1999).

[29] Breitweg, J. and others, Phys. Lett. **B479**, 37 (2000).

[30] Adloff, C. and others, Phys. Lett. **B483**, 36 (2000).

[31] Chekanov, S. and others, Eur. Phys. J. **C23**, 615 (2002).

[32] Adloff, C. and others, Eur. Phys. J. **C25**, 13 (2002).

[33] Wagner, Jeannine, *Charm and beauty production at HERA with D* - muon events.*

[34] Aktas, A. and others, Phys. Lett. **B621**, 56 (2005).

[35] Collins, John C. (1997).

Appendix A

Description of HZ05040

The following short description of the HzTool subroutine HZ05040 will be published in the HzTool -manual. The current version of the manual is available at *http://hepforge.cedar.ac.uk/hztool/docs/hztool.pdf.*

HZ05040: Measurement of Charm and Beauty Photoproduction at HERA Using $D^*\mu$ Correlations

Purpose:
Produces the histograms for the $D^*\mu$ analysis of the measurement presented in the paper DESY 05-040.
Event selection:
$p_T(D^*) > 1.5$ GeV
$|\eta(D^*)| < 1.5$
$p(\mu) > 2$ GeV
$|\eta(\mu)| < 1.735$
$0.05 < y < 0.75$
$Q^2 < 1$ GeV^2
Structure:
HZ05040 is callable at any time.

HZ05040 calls the subroutine btype(id1,id2,type) to determine angle and charge correlations for beauty corrections.

Usage:

```
*
        INTEGER IFLAG
        ...
        call HZ05040(IFLAG )
```

Input arguments

IFLAG=1: Initialisation

IFLAG=2: Histogram Filling

IFLAG=3: Termination

Histograms

ID=101: $1/\sigma \, d\sigma/dp_T(\mu)$

ID=102: $1/\sigma \, d\sigma/dp_T(D^*)$

ID=103: $1/\sigma \, d\sigma/d\eta(\mu)$

ID=104: $1/\sigma \, d\sigma/d\eta(D^*)$

ID=105: $1/\sigma \, d\sigma/dp_T(D^*\mu)$

ID=106: $1/\sigma \, d\sigma/dp_T(D^*\mu)$, finer binning

ID=107: $1/\sigma \, d\sigma/d\Delta\phi(D^*\mu)$

ID=108: $1/\sigma \, d\sigma/d\Delta\phi(D^*\mu)$, finer binning

ID=109: $1/\sigma \, d\sigma/dM(D^*\mu)$

ID=110: $1/\sigma \, d\sigma/d\hat{y}(D^*\mu)$

ID=111: $1/\sigma \, d\sigma/d\log(x_g)$, b-corrected

ID=112: $1/\sigma \, d\sigma/dp_T(D^*\mu)$, b-corrected

ID=113: $1/\sigma \, d\sigma/d\hat{y}(D^*\mu)$, b-corrected

The histograms -101 to -113 contain the data of the distributions. The finer binning of histograms 106 and 108 has to be compared to the data in -105 and -107, respectively, because in the data no finer binning is available.

Histograms 111 to 113 contain the distributions after correcting for angle and charge correlations as presented in the paper.

Erklärung

Hiermit versichere ich, die vorliegende Arbeit selbstständig und nur unter Verwendung der angegebenen Hilfsmittel angefertigt zu haben.

Hamburg, den 29. September 2005.

Danksagung

Als erstes danke ich von Herzen meinen Eltern für ihre Geduld und ihre Unterstützung während meines gesamten Studiums, und meiner Schwester, die immer hinter mir stand, mich aber auch kritisierte, wenn ich falsch lag.

Natürlich gebührt auch höchster Dank Joachim Meyer, der mit seiner hervorragenden Vorlesung mein Interesse geweckt und mit sicherem Auge meine unsicheren Formulierungen aufgespürt hat, und Herrn Lechtenfeld, der mir die Arbeit hier erst ermöglicht hat.

To the people @ room 335: Dank an Lluis, der mir immer mit Rat, Tat und Doppelkeks beiseite stand, and peace to Tobias for throwin' in his buck o'five. And of course many thanks to Nina for all the help and advice about Linux, and for the Doves.

Am allermeisten jedoch danke ich Hannes für seine Geduld, seine Zeit, seine Inspiration, alles in allem für ein fantastisches Jahr!

Mein einigermaßen passables Englisch habe ich zum Teil Sandra zu verdanken, die mich tatsächlich dazu gebracht hat, eine Hausarbeit in einem Fach zu schreiben, das mit meinem Studium überhaupt nichts zu tun hat!

Dank auch an meine Freunde Armin, Basti, Frederik, Hotte, Marc, Nils und Tschab, dass es nach so vielen Jahren immer noch geht!

And last but not least danke ich meiner Freundin Rebecca, dass sie nicht ganz die Geduld mit mir verloren hat und immer ein offenes Ohr hatte für mein ewiges Geplapper über Quarks & Co.

Peace.